Assessing textural features of thoracic malignancies on pre-treatment ^{18}F-FDG PET/CT imaging

Chicklore, Sugama

Awarding institution:
King's College London

Assessing textural features of thoracic malignancies on pre-treatment ^{18}F-FDG PET/CT imaging

Dr. Sugama Chicklore MBBS, MRCS, MSc Nuclear Medicine

March 2020

Thesis submitted to King's College London for the degree of MD(Res)

Department of Cancer Imaging,
School of Biomedical Engineering and Imaging Sciences

ABSTRACT

Purpose

The purpose of my thesis was to assess the use of texture features derived from 2-[fluorine-18] fluoro-2-deoxy-d-glucose (^{18}F-FDG) images in thoracic cancers. To achieve this, two studies were undertaken**.**

1. The aim of the first study was to determine retrospectively if texture features derived from ^{18}F-FDG positron emission tomography/computed tomography (^{18}F-FDG PET/CT) images of malignant pleural mesothelioma (MPM) were associated with overall survival in a cohort of patients scanned in our institution.
2. The aim of the second study was to correlate prospectively texture parameters from ^{18}F-FDG PET/CT images of untreated non-small-cell lung cancer (NSCLC) with histological and immunohistochemical (IHC) parameters in order to obtain a better understanding of the biological factors that may be related to spatial heterogeneity of ^{18}F-FDG PET images.

Methods

1. Fifty-eight consecutive patients (mean age 64.4 years, 51 male) with MPM, investigated between January 2006 and December 2011, were included in the first study. Patients with previous pleurodesis were excluded as this can cause significant benign inflammatory ^{18}F-FDG uptake. ^{18}F-FDG PET/CT scans were processed and analysed using a standard protocol. Calculation of the texture features was performed using in-house software implemented with MATLAB (MathWorks, Natick, Mass, US). Texture features, standardised uptake values (SUVs), metabolic

tumour volume (MTV) and total lesion glycolysis (TLG) were derived from volume of interest (VOI) of the MPMs. Cox regression analysis was used to examine the effects of the PET parameters and other variables on survival outcomes.

2. Nineteen consecutive patients (mean age 70.5 years, 10 male) with histologically proven, ≥3cm NSCLC planned for surgery and undergoing ^{18}F-FDG PET/CT imaging were recruited prospectively. Calculation of the texture features was performed using in-house software implemented with MATLAB (MathWorks, Natick, Mass, US). The lobectomy specimens were marked such that its orientation within the body was known. Histology included markers of angiogenesis, hypoxia, glycolysis and proliferation. As data were not normally distributed on Shapiro-Wilk testing, Spearman rank correlation was used to assess correlations between eighteen ^{18}F-FDG PET derived texture parameters and 6 IHC stains.

Results

1. Univariable analysis indicated several variables including non-epithelioid histology (hazard ratio (HR) 2.13 (confidence interval (CI) 1.11-4.08)), log-TLG (HR 1.33 (CI 1.07-1.67)), first-order entropy (HR 1.61 (CI 1.02-2.56)) and first-order energy (HR 0.68 (CI 0.48-0.96)) were significantly associated with patient survival ($p<0.05$). Multivariable analysis showed that first-order entropy (HR 1.75 (CI 1.07-2.89)) was an independent predictor of patient survival.
2. All patients underwent imaging a median of 1 day before surgery (range: 1 day to 44 days). There were 10 adenocarcinomas (ADC), 8 squamous cell carcinomas (SCC) and 1 large cell neuroendocrine carcinoma (LCNC). Group 1 (all 19 patients): CD105 microvascular density (MVD), staining neovessel endothelial cells, correlated

negatively with TLG and first-order energy; and positively with neighbourhood grey tone difference matrices (NGTDM) coarseness (r = -0.51, -0.47, 0.53, respectively: all $p<0.05$). CD34 MVD, staining vascular and lymphatic endothelial cells, correlated negatively with MTV and TLG; and positively with NGTDM coarseness (r = -0.59, -0.50, 0.62, respectively: all $p<0.05$). $Ki67_{average}$ ($Ki67_{avg}$) and $Ki67_{maximum}$ ($Ki67_{max}$) values correlated negatively with grey level co-occurrence matrix (GLCM) energy and first-order skewness (r = -0.47 and r = -0.48, respectively: all $p<0.05$).

Group 2 (18 patients with ADC and SCC): CD105 MVD correlated negatively with TLG, first-order energy and first-order entropy; and positively with NGTDM coarseness (r = -0.53, -0.52, -0.47, 0.53, respectively: all $p<0.05$). CD34 MVD correlated negatively with MTV and TLG; and positively with NGTDM coarseness (r = -0.61, -0.52, 0.64, respectively: all $p<0.05$).

Group 3 (10 ADC patients): CD105 MVD and CD34 MVD correlated with both MTV (r = -0.71, -0.76, respectively: all $p<0.05$) and NGTDM coarseness (r= 0.75, 0.77, respectively: all $p<0.05$).

Group 4 (8 SCC patients): CD105 MVD and CD34 MVD correlated negatively with first-order energy (r = -0.79, -0.74, respectively: all $p<0.05$).

Hypoxia-inducible factor-1 (HIF-1)-alpha correlated strongly with MTV, second-order textural parameters (GLCM energy, GLCM homogeneity and GLCM entropy) and high-order textural parameters (NGTDM coarseness and NGTDM contrast) (r = 0.73, 0.71, 0.83, -0.81, -0.73, -0.73, respectively: all $p<0.05$).

Hexokinase-II (HEX-II) correlated strongly with MTV, second-order textural parameter (GLCM contrast) and high-order textural parameter (NGTDM coarseness) (r = -0.72, 0.73, 0.72, respectively: all $p<0.05$).

If the correction for multiple correlation testing was to be applied, the only statistically significant correlation was between CD34 MVD and high-order coarseness ($p = 0.004$), in Groups 1 and 2.

Conclusion

1. Textural features have prognostic ability in predicting survival in MPM patients. This is superior to the currently used standard PET parameters such as SUVs. In particular, first-order entropy is significantly associated with overall survival in MPM.
2. Several standard and textural parameters extracted from ^{18}F-FDG images of NSCLC correlate strongly with MVD, Ki67, HIF-1-alpha and HEX-II histological parameters suggesting relevant underlying biological mechanisms are associated with ^{18}F-FDG distribution in tumours. My study has also uncovered interesting differences in PET texture correlations with histological subtypes in NSCLC; with only limited data in current literature my study would add value to it.

PREFACE

My thesis includes two independent studies conducted at King's College London and Guy's and St. Thomas' Hospital NHS Foundation Trust. The common theme in both studies in my thesis is the use of texture features derived from ^{18}F-FDG images in different areas of oncology. I used the software Feature Analysis Software Tool (FAST) written in MATLAB by Dr Muhammad Musib Siddique, a previous employee of the KCL Cancer Imaging group to perform all texture analysis. I drew regions of interest (ROI) on each axial slice of the image around the tumours and the FAST program processes a volume of interest (VOI) and then applies mathematical operations to output texture parameters.

The first study investigated the role of texture features derived from ^{18}F-FDG images to predict overall survival in MPM patients (chapter 4). Mr Paul Bassett provided professional statistical input for this study.

The second study investigated the histological correlates of ^{18}F-FDG images PET images of NSCLC (chapter 5). I prospectively recruited 19 patients with NSCLC for this study. 6 IHC parameters derived from pathological surgical specimens were correlated with texture parameters derived from ^{18}F-FDG PET images. Dr. Emma Mclean and Dr. Daisuke Nonaka from St. Thomas' Hospital histopathology department cut the surgical specimens and scored the IHC stained slides for all 19 patients.

TABLE OF CONTENTS

LIST OF FIGURES

LIST OF TABLES

ACKNOWLEDGEMENTS

I would like to acknowledge the contribution of few people without whose help this thesis would have been an impossible task. I am grateful to my supervisors Prof Gary Cook and Prof Vicky Goh for their guidance and input. I would also like to thank my cardiothoracic surgery colleagues who helped with patient recruitment for my prospective study (chapter 5), in particular Miss Juliet King, Mrs Karen Harrison-Phipps and Mr. Andrea Bille. I would like to thank my histopathology colleagues Dr. Emma Mclean and Dr. Daisuke Nonaka who helped me with cutting and analyses of the histology specimens in chapter 5. I must thank Dr Muhammad Musib Siddique who wrote the software Feature Analysis Software Tool (FAST) in MATLAB and for his continuous support throughout my thesis. I must also thank Mr Paul Bassett for his professional statistical input in chapter 4. I must thank all my colleagues at Clinical PET Centre in King's College London/Guy's and St. Thomas NHS Foundation Trust for their support through my study period.

I would also like to thank my husband Sujith, my son Tanav, my daughter Tiya and my parents for their encouragement and moral support.

ABBREVIATIONS

^{18}F-FDG	2-[fluorine-18] fluoro-2-deoxy-d-glucose
ADC	Adenocarcinoma
ARSAC	Administration of Radioactive Substances Advisory Committee
ALK	Anaplastic lymphoma kinase
bFGF	Basic fibroblast growth factor
CD	Cluster of differentiation
CR	Complete responder
CT	Computed tomography
CI	Confidence interval
CNN	Convolutional neural network
EGFR	Epidermal growth factor receptor
FAST	Feature Analysis Software Tool
FLT	Fluorothymidine
FH	Freehand
FLAB	Fuzzy locally adaptive Bayesian
GLUT-1	Glucose transporter-1
GLCM	Grey level co-occurrence matrices
HR	Hazard ratios
HEX-II	Hexokinase-II
HIF-1-alpha	Hypoxia inducible factor–1-alpha
IHC	Immunohistochemical
$Ki67_{avg}$	$Ki67_{average}$
$Ki67_{max}$	$Ki67_{maximum}$
LCNC	Large cell neuroendocrine carcinoma
LASSO	Least absolute shrinkage and selection operator
Lu	Lutetium
LSO	Lutetium oxyorthosilicate
LYSO	Lutetium yttrium orthosilicate
ML	Machine learning
MRI	Magnetic resonance imaging
MPM	Malignant pleural mesothelioma
MTV	Metabolic tumour value
MVD	Microvascular density
NHS	National Health Service
NGTDM	Neighbourhood grey tone difference matrices
NR	Non-responder
NSCLC	Non-small cell lung cancer
NF-κB	Nuclear factor-κB
OSEM	Ordered subset expectation maximisation
OS	Overall survival
PR	Partial responder
PMT	Photomultiplier tubes

PDGF	Platelet derived growth factor
PET	Positron emission tomography
PD-1	Programmed cell death-1
PD-L1	Programmed cell death-1 ligand
ROI	Region of interest
SCC	Squamous cell carcinoma
SD	Standard deviation
SUV	Standardised uptake value
SVM	Support vector machine
TLG	Total lesion glycolysis
t	Time
TAM	Tumour-associated macrophage
TIL	Tumour-infiltrating lymphocyte
TKI	Tyrosine kinase inhibitor
UK	United Kingdom
VEGF	Vascular endothelial growth factor
VOI	Volume of interest
WSI	Whole-slide image

CHAPTER 1

INTRODUCTION

For the purposes of my thesis I will focus on 2-[fluorine-18] fluoro-2-deoxy-d-glucose (^{18}F-FDG) tracer alone as it is the most common tracer used and the sole tracer used in all my experiment chapters.

1.1 ^{18}F-FDG PET/CT imaging in clinical practice

Cancer is one of the leading causes of death in the world (1) including the United Kingdom (UK) (2). Lung cancer is the most commonly diagnosed cancer and the leading cause of cancer deaths worldwide (2). Imaging plays a crucial role in the management of cancer patients as patient management is guided by imaging, among other factors. Imaging has a central role in staging, follow up and restaging patients with cancer. Since its introduction into clinical practice, ^{18}F-FDG positron emission tomography (PET) has established its role in this field and its role is increasing in oncology. It is a functional imaging modality and ^{18}F-FDG is the most commonly used tracer for PET imaging. ^{18}F-FDG PET provides qualitative and quantitative metabolic information regarding the tumours. PET also can identify pathologies by abnormal tracer uptake more sensitively than on cross-sectional imaging by identifying disease often before morphological abnormalities are apparent. PET, when combined with computed tomography (CT), provides both metabolic and anatomical information, respectively in one setting. This combined modality helps localise the lesions better than on PET alone and hence increases confidence in interpreting the scans. The

evidence-based indications for the use of PET/CT in UK are published by the Royal College of Radiologists (3).

1.2 Understanding tumour biology

Rapid cell proliferation, local invasion and distant metastases are hallmarks of malignancy. Tumorigenesis is supported by polypeptide growth factors (e.g. platelet derived growth factor [PDGF] and insulin-like growth factor) and factors promoting tumour angiogenesis (e.g. vascular endothelial growth factor [VEGF] and basic fibroblast growth factor [bFGF]) (4). A large tumour which is rapidly proliferating and more than 1 mm to 2 mm in diameter outgrows its existing vasculature and hence becomes necrotic unless neoangiogenesis occurs (4).

Malignant cells have increased glucose utilisation due to upregulation of hexokinase activity leading to the phosphorylation and trapping of ^{18}F-FDG in the cell and increased expression of glucose transporters-1 (GLUT-1) (5). Glucose undergoes glycolysis with the formation of pyruvate under aerobic conditions. However, under hypoxic conditions, glucose is metabolised under anaerobic conditions with resultant increased tumour lactate levels (6). ^{18}F-FDG is a radiolabelled analogue of glucose which is taken up by metabolically active tumour cells through the same GLUT-1 transporters. The rate of uptake of ^{18}F-FDG by the tumour cells is proportional to their metabolic activity (6). Like glucose, it undergoes phosphorylation to form ^{18}F-FDG-6-phosphate; however, unlike glucose, it does not undergo further metabolism, thereby becoming trapped in metabolically active cells (Figure 1).

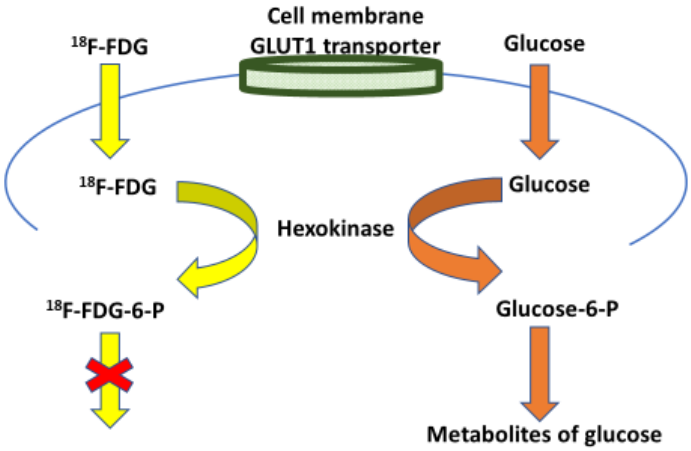

Figure 1. Metabolic pathways of Glucose and ^{18}F-FDG

1.3 General principles of PET/CT imaging

The principle of PET is that a radiopharmaceutical tracer is injected intravenously into a patient and emits photons that are registered by external detectors positioned in a ring. ^{18}F is a cyclotron-produced radioisotope of fluorine that emits positrons that annihilate with electrons to produce two nearly opposing photons (511 keV) and has a short half-life (110 minutes) (Figure 2). FDG is labelled with ^{18}F and can be usually imaged 60 to 90 minutes after injection. These opposing annihilation photons are detected by the PET scanner simultaneously. The PET scanner has scintillation crystals which are coupled to photomultiplier tubes (PMTs). The new generation PET detectors widely use Lutetium (Lu) based scintillators such as LSO (lutetium oxyorthosilicate) and LYSO (Lutetium yttrium orthosilicate) because of their higher stopping power and lower decay time which in turn reduces the scanning time. In our department we currently use PET/CT scanners from 2 vendors; GE Healthcare (GE Discovery 710) and Siemens Medical Solutions (Siemens Biograph mCT), although all studies in this thesis were performed on the GE scanners.

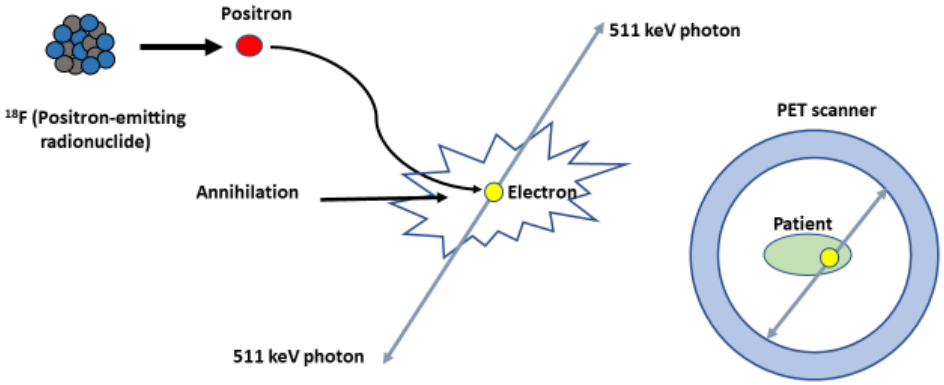

Figure 2. ^{18}F Positron emission and positron-electron annihilation

As discussed above, PET image acquisition is based on the simultaneous (coincidence) detection of two photons. However, not all coincidences contribute to image formation. There are different types of coincidences: true, random, scatter and multiple. Ideally, we would want only the true coincidences detected by the scanner as the others contribute to background noise which leads to artefacts. The scattered attenuated photons within the patient are not detected which leads to attenuation artefacts due to more attenuation from deeper tissues but this can be corrected for. The images are then reconstructed using iterative reconstruction algorithms.

1.4 Quantifying tumour heterogeneity in ^{18}F-FDG PET/CT imaging by texture analysis

In this section I will be introducing the concept of texture analysis in ^{18}F-FDG PET/CT scans for malignancies (7).

Medical imaging is used routinely in oncology for diagnosis, staging and assessment of treatment response, but is less reliable for predicting response or for inferring prognosis before therapy has been instigated, such that the ability to stratify patients to different treatments or to personalise therapy remains largely limited to TNM staging information. Personalised medicine is a goal in modern cancer therapy that aims for optimal treatment for an individual patient that is dependent on tumour characteristics in that individual. The ability to predict the behaviour of a tumour to treatment before therapy has been instigated would be invaluable in enabling stratification in clinical trials or personalising future cancer treatments in the clinic.

Whilst novel imaging sequences, contrast agents and tracers are being developed to explore new aspects of tumour biology, it is also recognised that standard medical images may contain more useful information than is being used in a routine clinical setting. The field of "radiomics", whereby additional features may be extracted from medical images, may not only allow more accurate measurement of treatment response but also non-invasive molecular and genetic profiling of tumours as a further step towards personalised Medicine (8).

^{18}F-FDG PET/CT is already well established for staging certain cancers due to better sensitivity and specificity compared to anatomical imaging such as CT (9). It also has the advantage of being able to measure therapy response relatively early in the course of treatment when anatomical changes have not occurred, such that serial ^{18}F-FDG PET/CT

scans are being used successfully in a number of cancers to detect early treatment effect, in clinical routine and increasingly, in clinical trials (10, 11). It is useful to have knowledge of the sensitivity of a tumour to a therapeutic regimen as early as possible as this will help tailor the treatment for individual patients, particularly if the patient is not responding to a drug. Nonresponding patients can have treatment intensified or can be switched to alternative therapies, increasing the probability of tumour control and avoiding toxicity from ineffective treatment.

As PET also lends itself to quantification, semiquantitative measurements of tracer uptake are frequently adopted in clinical trials and clinical routine, including standardised uptake values (SUVs; e.g. SUV_{mean}, SUV_{max}, SUV_{peak}) (12). SUV is a measurement of the tracer uptake in a tumour normalised on the basis of a distribution volume. It is the ratio of tissue radioactivity concentration at a given time (t) and the injected activity at the time of injection and usually divided by the body weight.

$$SUV(t) = \frac{\text{radioactive concentration at time t (MBq/kg)}}{\text{injected activity / body weight}}$$

SUV_{max} is the hottest voxel within a defined volume of interest (VOI) and this is the most widely used parameter due to its ease of use and being operator independent. SUV_{peak} is an average SUV computed within a fixed and most active $1cm^3$ VOI, often containing (and not necessarily centred on) the hottest pixel value.

However, it is recognised that ^{18}F-FDG uptake may not always accurately reflect tumour response due to confounding factors such as early reduction in activity in the presence of viable tumour (13) or increases in uptake secondary to inflammatory processes following chemotherapy and radiotherapy (14, 15). There is also variability in the reported accuracy of

^{18}F-FDG PET/CT in this context. For example, in non-small cell lung cancer (NSCLC), the ability of ^{18}F-FDG PET to predict histopathological response varies from 80 % to 97 % in terms of sensitivity and from 64 % to 100 % in terms of specificity (16).

There is only limited evidence that the level of uptake on pre-treatment scans, as measured by various SUV parameters, may be predictive (17-21), but results sometimes conflict as to whether high or low SUVs are predictive depending on treatment modality, e.g. radiotherapy vs. chemotherapy in NSCLC (20, 21). Also, in NSCLC there are data that show that the baseline SUV prior to therapy may be prognostic, with low values being associated with longer survival, but the optimal cut-off SUV varies widely in the literature (16). Baseline ^{18}F-FDG PET has also shown some predictive value in radioimmunotherapy in non-Hodgkin's lymphoma (22), high-grade gliomas (23), head and neck cancer (24, 25) and anal cancer (26), but not oesophageal carcinoma (27). In this context, introducing predictive and prognostic parameters from baseline ^{18}F-FDG PET scans that perform better than SUV parameters would be invaluable and would open the potential to stratify patients more appropriately for treatment.

It is recognised that malignant tumours exhibit intratumoural biological heterogeneity associated with cellular and molecular characteristics such as cellular proliferation, necrosis, fibrosis, differences in blood flow and angiogenesis, cellular metabolism, hypoxia and expression of specific receptors, some of which may be evident on histological analysis. Similarly, heterogeneity of ^{18}F-FDG uptake within tumours has been attributed to a number of factors including cellularity, proliferation, angiogenesis, necrosis and hypoxia, factors that independently have been associated with more aggressive behaviour, poorer response to treatment and worse prognosis. However, there is currently little evidence to confirm what biological and molecular features underlie differences in tumour texture in ^{18}F-FDG PET

images.

Texture analysis is emerging as a new tool for assessing intratumoural heterogeneity in medical imaging. Tumour heterogeneity in baseline ^{18}F-FDG PET imaging may allow better tissue characterisation, image segmentation and improved prediction of therapy response and survival (28-35).

Whilst the data have been rapidly accumulating for contrast enhanced CT and magnetic resonance imaging (MRI) in this field, the evidence for texture analysis in PET imaging is only just emerging.

1.5 Texture analysis

Texture analysis refers to a variety of mathematical methods that may be applied to describe the relationships between the grey level intensity of pixels or voxels and their position within an image. An advantage of measuring textural parameters is that it is a post-processing technique that can be applied to data acquired during standard clinical imaging protocols thereby maximizing the information that can be derived from standard clinical images.

A number of texture features can be derived that provide a measure of intralesional heterogeneity (33, 36). Textural parameters can be derived from statistics-based (37, 38), model-based (39-42), or transform-based (43, 44) methods. Statistics-based techniques have been most commonly applied and are based on the spatial distribution of pixel or voxel values, calculating local features at each pixel in the image and deriving parameters from the distributions of the local features. The statistical methods are categorised into

first-order (global, histogram), second-order (local, 2 pixels) and high-order (local, 3 or more pixels) statistics.

First-order parameters describe global textural features that relate to the grey level frequency distribution within the region of interest (ROI). They are based on histogram analysis and include mean, minimum and maximum intensity, first-order energy, first-order entropy, standard deviation (SD), skewness and kurtosis.

Second-order features describe local texture features and are calculated using grey level co-occurrence matrices (GLCM). These matrices determine how often a pixel of intensity *i* finds itself within a certain relationship to another pixel of intensity *j*. Second-order features based on a co-occurrence matrices include second-order entropy, second-order energy, contrast, homogeneity, dissimilarity and correlation.

High-order parameters can be calculated using neighbourhood grey tone (intensity) difference matrices (NGTDMs) to describe local features (33, 45). Local texture parameters derived from NGTDMs are based on differences between each voxel and the neighbouring voxels in adjacent image planes and are thought to closely resemble the human experience of the image (45).

For example, coarseness, one of the local textural parameters, has been likened to granularity within an image and is the most fundamental property of texture. Contrast relates to the dynamic range of intensity levels in an image and the level of local intensity variation and busyness relates to the rate of intensity change within an image (31, 45).

Regional features can also be calculated from voxel alignment (e.g. run length and run-length variability) and grey level size-zone matrices that reflect regional intensity variations or the distribution of homogeneous regions (e.g. zone emphasis and size-zone variability) (33) (Table 1).

Order of textural features	Description		Examples
First	Grey level frequency distribution from histogram analysis	Global	Minimum, mean and maximum intensity Standard deviation Skewness Kurtosis
Second	From spatial grey level dependence matrices	Local	Entropy Energy Contrast Homogeneity Dissimilarity Correlation
Higher	From neighbourhood grey-tone difference matrices	Local	Coarseness Contrast Busyness Complexity
	From voxel alignment matrices	Regional	Run-length and emphasis Run-length variability
	From grey level size zone matrices	Regional	Zone emphasis Size-zone variability

Table 1. Textural features

To illustrate the difference between different order statistics, Figure 3 shows four simulated cases with different intensity patterns. All four cases will give the same features based on first-order statistics (e.g. histogram, mean, first-order energy, first-order entropy etc.), as properties are calculated using individual pixel values ignoring the spatial relationships between pixels. Second-order statistics based on a co-occurrence matrix will give different features between Figure 3a and b as the properties of two-pixel values occurring at specific locations relative to each other are estimated. However, features will be the same for cases Figure 3b, c and d when the offset is one pixel in the x-direction. High-order statistics, e.g. NGTDM, estimate properties based on more pixels occurring at specific locations relative to each other and will give different results for all the cases shown in Figure 3.

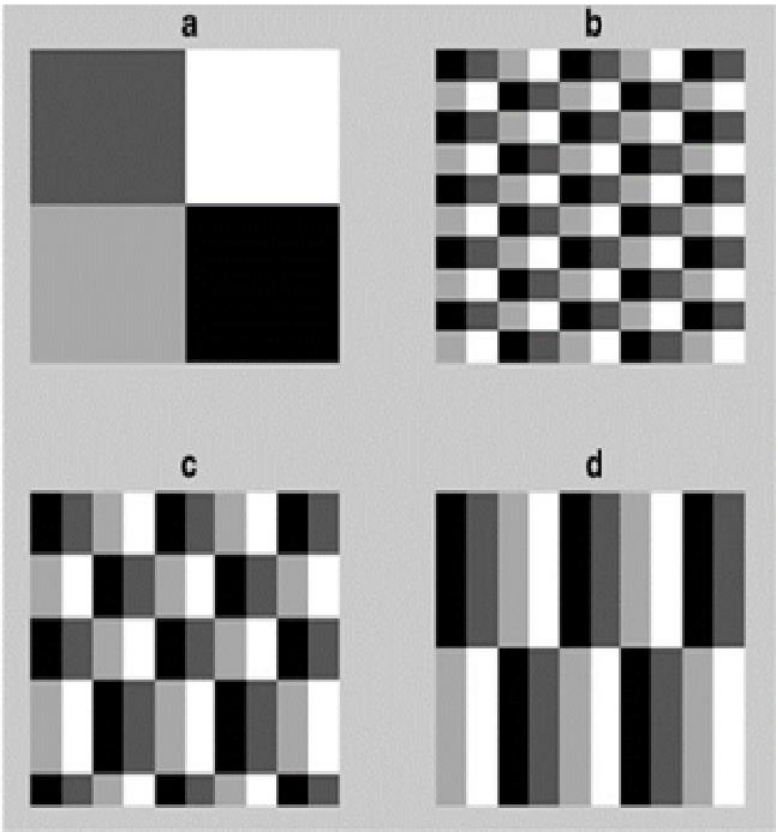

Figure 3. Four simulations of different intensity variations. First-order parameters are the same for all four cases. Although the second-order features (derived from the grey level co-occurrence matrix with offset [10]) will be different for a compared to b, c and d, the latter three will be the same. Third-order features (derived from neighbourhood grey tone difference matrices or grey level size-zone matrices) will be different for all four cases

1.6 Texture analysis in ^{18}F-FDG PET

Whilst the high spatial resolution of CT and MRI with subcentimeter pixel sizes allows texture analysis of relatively small tumours, the poorer spatial resolution of PET with pixel sizes of up to 5 mm, limits the size of small volume tumours that may be assessed, the requirement being for a reasonable number of adjacent pixels to be present to be able to measure some of the texture features. The accuracy and precision of texture analysis in clinical evaluation depends significantly on individual scanning protocols. Factors such as image acquisition, reconstruction and inherent image quality parameters such as noise, motion artefacts and slice thickness, may be important. It is to be expected that all texture

analysis methods are influenced to some extent by these factors and the sensitivity of various texture features may be based on different image models.

Veenland et al. (46) investigated the sensitivity of four different texture analysis methods for image noise and blur and found that the discriminative performance of all texture features was reduced by noise. The influence of noise on the discriminative performance was dependent on the image type used. The discrimination of more gradually different images, such as fractal images, is poor for relatively low noise levels but when the images are more different, only high noise levels decrease the discriminative performance. Galavis et al. (47) studied the variability of the texture features in PET images due to different acquisition modes and reconstruction parameters. Texture features such as first-order entropy, first-order energy, maximal correlation coefficient and low grey-level run emphasis exhibited small variations due to differences on acquisition mode and reconstruction parameters. Features such as contrast-NGTDM, coarseness, homogeneity, and busyness showed larger variations.

These are obviously important potential limitations of texture analysis and these aspects would require further evaluation if texture analysis of PET images were to be used in multicentre studies, for example.

Further factors that will require careful assessment are the methods used for ROI definition on PET images and related intra-observer and inter-observer variation. An initial study has shown that the reproducibility of a number of textural parameters is as good as or better than that for SUVs (48). A recent study from our centre showed that textural parameters vary with time after injection as do SUVs in ^{18}F-FDG PET imaging (49, 50).

Following radiological reports of the use of textural features, there has been more recent interest in the use of texture analysis in ^{18}F-FDG PET imaging in oncology. The literature describing the use of ^{18}F-FDG PET in analysing tumour heterogeneity is summarised in Table 2. Types of cancer that have been investigated with texture analysis include head and neck cancer, cervical cancer, soft tissue sarcomas, oesophageal cancer and NSCLC (28-35). There have been numerous studies published in the last few years describing the use of ^{18}F-FDG PET in analysing tumour heterogeneity and I have summarised a few, ranging over the years, in the table for the purposes of my thesis.

Table 2. Current literature describing texture analysis of ^{18}F-FDG PET

Cancer type	Study findings	Correlate
Head and neck SCC (animal model)	Heterogeneity of ^{18}F-FDG uptake within a tumour correlates with histopathological findings (p=0.028) (28)	Histopathology
Head and neck SCC	Low-intensity long-run emphasis is associated with higher local failure in patients treated with chemoradiotherapy (51)	
Sarcoma	Tumour spatial heterogeneity predicts patient outcome (p<0.001) (32)	SUV_{max}
Head and neck and cervix	Textural features explain tumour uptake and treatment resistance (cervical p=0.04; head and neck p=0.0012) (34)	SUV_{max}
Head and neck	NGTDM features such as PET coarseness, PET contrast, and CT coarseness provided good discrimination performance (30, 31)	
Oesophagus	Local (p<0.0006) and regional (p=0.0002) textural features predict response to chemoradiotherapy (33)	SUV_{max}, SUV_{peak} SUV_{mean}
NSCLC	Potential use of heterogeneity parameter using SUV-volume histograms described (29)	
NSCLC	Multimodality image feature modelling is a predictor of locoregional recurrence after radiotherapy (35)	SUV Hounsfield unit
NSCLC	Demonstrated significant associations between PET features, CT features, and histological type and potential use of PET texture features to differentiate between histological types (52)	Histopathology SUV CT texture features
Salivary gland carcinoma	Minimum intensity and long run emphasis were significant predictors of progression free survival (53)	

1.7 Tissue characterisation and segmentation

Texture analysis has been used for adaptive smoothing, segmentation and classification of medical images (54, 55). Whilst I am not aware that this approach has yet been used in PET, there is the potential for improving the reproducibility of conventional parameters such as SUV.

Parameters derived from NGTDMs, describing features such as coarseness, contrast and busyness (45), have shown the ability to differentiate primary and nodal tumour from normal tissue in head and neck cancer (30). It was shown that the primary tumour and metastatic nodes have lower coarseness and busyness but higher contrast than normal tissues.

The same group studied 20 patients with head and neck cancers and 20 patients with NSCLC and manually segmented normal and abnormal tissues on ^{18}F-FDG PET images (31). Texture features, including some derived from GLCMs and NGTDMs, were selected for characterisation of these segmented ROI. They concluded that NGTDM features, such as PET coarseness, PET contrast, and CT coarseness, extracted from the ^{18}F-FDG PET/CT images provided good discrimination, and this may lead to improvement in the accuracy of radiation targeting of head and neck cancers. Other potential heterogeneity parameters using SUV–volume histograms in patients with NSCLC have been described but this has not been clinically tested (29).

Another study employed deep learning (convolutional neural networks (CNN)) and machine learning (ML) (random forests, support vector machines (SVM), adaptive boosting and artificial neural network). The four ML methods separately used 13 standard diagnostic features (e.g. SUV, tumour size) and 82 textural features to classify mediastinal lymph nodes

on ^{18}F-FDG PET images in patients with NSCLC (56). The accuracy of CNN was 86% and was not significantly different from those of the best ML methods that used standard diagnostic features or the combination of diagnostic and textural features. They concluded that the performance of CNN is not significantly different from the best classical methods and radiologists for classifying mediastinal lymph node metastasis of NSCLC from PET/CT images. They also noted that as CNN does not need tumour segmentation or feature calculation, it is more convenient and more objective than the classical methods.

1.8 Prediction and prognosis

Some studies have shown that texture parameters are better than SUV parameters in predicting response to therapy and survival in a number of cancers. Eary et al. retrospectively analysed 234 patients with sarcoma for tumour heterogeneity on baseline ^{18}F-FDG scans before either neoadjuvant chemotherapy or surgical resection (32). The technique assessed a parameter derived from the variation from a three-dimensional ellipsoid model for homogeneous tissue. It was concluded that heterogeneity was a strong independent predictor of survival, and that SUV_{max} was somewhat less predictive of survival. El Naqa et al. used first- and second-order texture features to predict outcome in head and neck cancers (9 patients) and cervix cancer (14 patients) (34). It was concluded that texture features could significantly aid in summarising tumour uptake characteristics in its microenvironment and its relationship to treatment resistance in certain clinical scenarios. Tixier et al. retrospectively studied response to chemoradiotherapy in 41 patients with oesophageal cancer (33). CT RECIST criteria were used to categorise the patients as complete responders (CR), partial responders (PR) or non-responders (NR). A Bayesian

algorithm was used to automatically delineate tumour volume, and only primary tumours were considered. SUV parameters (max, peak and mean) and 38 textural parameters were extracted from the same tumour volumes. By receiver operating characteristic curve analysis it was found that texture analysis was able to differentiate CR, PR and NR with higher sensitivity than any SUV measurement, thus demonstrating that texture analysis of the intratumoural tracer heterogeneity on baseline ^{18}F-FDG PET scans can predict response to combined chemoradiation treatment in oesophageal cancer. Texture features derived from co-occurrence matrices strongly differentiated NRs from PRs, thus helping stratify patients appropriately. It was also suggested that regional and local characterisation of ^{18}F-FDG PET tracer heterogeneity in tumours is more powerful than global measurements currently used in clinical practice.

Vaidya et al. analysed pre-treatment ^{18}F-FDG PET/CT studies in 27 NSCLC patients for local and locoregional failures (35). They extracted 32 tumour region features based on SUV or Hounsfield units, intensity–volume histogram and textural characteristics. Intensity–volume histogram variables showed the highest univariate association with locoregional recurrence and it was concluded that multimodality image feature modelling with ^{18}F-FDG PET and CT is a predictor of locoregional recurrence in NSCLC after radiotherapy.

Carvalho et al., in their study demonstrated texture parameters derived from metastatic lymph nodes from ^{18}F-FDG PET images in patients with NSCLC using a least absolute shrinkage and selection operator (LASSO) method have been found to be more strongly associated with overall survival than when extracted from primary tumour data (57).

Jansen et al. established in their study that genetic mutations, including epidermal growth factor receptor (EGFR) mutations and anaplastic lymphoma kinase gene rearrangements, that are associated with improved response to certain tyrosine kinase inhibitors (TKIs), are

associated with image features derived from ^{18}F-FDG PET in NSCLC (58). However, the correlation between EGFR mutated tumours and level of ^{18}F-FDG uptake is conflicting in the published literature, with some studies predominantly showing high ^{18}F-FDG uptake in EGFR mutated tumours, reflecting increased glycolysis through AKT signalling (59), and others showing lower uptake (60). However more recent studies have demonstrated that along with standard PET parameters, such as SUV_{max}, texture parameters also show associations with EGFR mutation status (61, 62) and some studies have shown that textural features can predict treatment response and survival following treatment with TKIs (63, 64). Moon et al. in their study with small cell lung cancer cohort have shown some less specific association between ^{18}F-FDG PET textural features and genetic heterogeneity (65). Nair et al. published 2 papers in 2012 and 2014 demonstrating correlation between NSCLC genomics and ^{18}F-FDG textural features (66, 67). In their first paper they found that a prognostic metagene signature derived from 25 patients with NSCLC was associated with a multivariate ^{18}F-FDG uptake feature derived from principal components analysis, both of which were associated with survival in external and validation cohorts (66). The radiogenomic profile was associated with altered cell cycle, proliferation, death and self-recognition pathways, and recognised nuclear factor-κB (NF-κB) protein as a central node within the metagene. The later study showed that NF-κB protein expression is associated with high ^{18}F-FDG uptake with both being related to advanced tumour stage, grade and invasion (67). Two recent reviews, one of which was from our centre, described correlations between NSCLC ^{18}F-FDG PET radiomic features and treatment response and survival (68, 69). Ohri et al. in their study with 201 datasets and 43 textural features, used the LASSO method and identified a single textural feature (SumMean) as an independent predictor of overall survival in large tumours treated with chemoradiotherapy (70). In a more recent study of 358 datasets and 665

radiomic features, a similar LASSO methodology was used to derive predictive feature vectors that were tested on an independent validation set and predicted a 14-month survival difference (71).

1.9 Pathobiological basis of texture in ^{18}F-FDG PET imaging

Whilst several textural features in structural and functional imaging of cancer have been shown to differentiate tumour types and predict treatment response, and/or are associated with survival, it is largely unknown what the biological correlates of textural features are.

There are few pre-clinical studies demonstrating the correlation between texture features and molecular and biological features. Henriksson et al. investigated the pattern of ^{18}F-FDG uptake in relation to the intratumoural histopathological appearance in nude mice with xenografted tumours originating from an established head and neck squamous cell carcinoma (SCC) model (28). Regions containing more than 50% tumour cells showed significantly higher ^{18}F-FDG uptake than those with more stromal tissue and necrosis. It was concluded that heterogeneous ^{18}F-FDG uptake within a tumour is correlated with histopathological findings and that the variable appearance of tracer uptake on PET scan depends on the distribution of different tissue components in the tumour. In hepatoma and pancreatic murine tumour models, ^{18}F-FDG spatial heterogeneity has been reported to be associated with the distribution of glucose transporters and hexokinase (72, 73). In orthotopic breast cancer models, a correlation was found between various radiomic texture features describing the spatial distribution of ^{18}F-FDG activity in autoradiographic images and the spatial distribution or density of cells determined on histopathological staining (74).

It has also been postulated that increased image heterogeneity within tumours may be associated with differences in regional tumour cellularity, proliferation, hypoxia, angiogenesis and necrosis (33, 75), factors that independently have been associated with more aggressive behaviour, poorer response to treatment and worse prognosis. Other histopathological correlates such as antigen or receptor expression also likely are associated with tumour heterogeneity. It is unlikely that structural and functional imaging textural features are associated with the same biological causes of spatial intensity variations within an image, although in general, features that correspond to increased heterogeneity have been assumed to be related to a poorer prognosis and poor response to treatment. However, given the multitude of textural parameters that have been described, this is probably an oversimplification of the relationships between tumour biology and heterogeneity within an image. For example, CT features related to increased heterogeneity, including increased entropy or decreased energy, predict poor response and/or survival (76-78), whereas in ^{18}F-FDG PET imaging of oesophageal carcinoma, treatment responders showed greater local heterogeneity at baseline, but measures of regional tumour heterogeneity showed better response stratification (33). In head and neck cancer, tumour and nodes have been reported as having lower coarseness and busyness but higher contrast than normal tissues (31). The relationship between texture features and tissue characteristics is therefore complex and texture feature measurements can clearly not simply be regarded as lying on a spectrum between heterogeneity and homogeneity. Some recent studies have attempted to correlate histological and biological features of NSCLC with radiomic features from ^{18}F-FDG PET imaging. Bashir et al. (79) in their study of NSCLC observed correlations between histopathological mean cell density and lacunarity (large gaps between clusters of cells) and standard ^{18}F-FDG parameters, including SUV_{mean}

and total lesion glycolysis (TLG), first-order statistical features, including kurtosis and skewness, and ^{18}F-FDG lacunarity. Karacavus et al. (80) in their study have shown associations between several texture parameters and NSCLC clinical stage and Ki67 immunohistochemistry analysis of proliferation using k-nearest neighbours and SVM methods. Another recent study reported the possibility of differentiation of histopathological tumour subtypes (SCC and adenocarcinoma (ADC)) using texture and colour features derived from ^{18}F-FDG PET images using a SVM algorithm with an area under the receiver operating characteristic curve of 0.89 (81).

With the advent of immune checkpoint inhibitors that target programmed cell death-1 and its ligand (PD-1, PD-L1), the treatment of advanced and metastatic cancers, such as NSCLC and melanoma, has drastically changed and there is no longer a dismal prognosis. Currently immunohistochemical (IHC) measurement of PD-L1 expression in biopsy material is used to target these patients. It is recognised that some patients respond well despite negative PD-L1 expression measured on IHC, and that PD-L1 expression is heterogeneous, suggesting inaccuracies and sampling errors in measurement (82, 83). Imaging has the potential to reveal global, locoregional and metastatic characteristics associated with PD-L1 expression either directly or by texture analysis (84, 85).

Recent studies have also explored the relationships between regional ^{18}F-FDG PET and MRI textural features from combined PET/MRI showing correlations with microvascular density (MVD) and expression of vascular endothelial growth factor in renal cell carcinoma, with the highest correlations when combining PET and MRI radiomic features (86).

There is therefore a need to carefully investigate texture features from different imaging modalities and using different PET tracers to correlate with histopathological features that may influence image texture including angiogenesis, hypoxia, proliferation etc., either in a

preclinical model or in humans when tissue is available for complementary histological analysis. Although the current reference standard in clinical practice is histopathology and IHC, using extracted texture features from imaging may help us in the future to better understand tumour behaviour including local invasion, metastatic potential, the relationship and interaction of tumour cells with the microenvironment, and predict and monitor response or resistance to therapy (87).

1.10 Texture analysis in other imaging modalities

Texture analysis in other radiological imaging has been more extensively described than with PET. CT and MRI texture studies have shown improved tissue characterisation, response prediction and prognostication, and studies are emerging in which the link between texture features and tumour biology has been analysed.

There is evidence that texture analysis may aid tissue characterisation. Al-Kadi and Watson showed that CT features can be helpful in differentiating aggressive from nonaggressive NSCLC (37), while it has also been possible to show differences between histological subtypes using textural parameters on CT (88). MRI studies have shown that texture features may differ between benign and malignant lesions. Co-occurrence matrix features of dynamic contrast-enhanced MRI images and signal enhancement ratio maps have been used in breast cancer to distinguish between benign and malignant lesions (89, 90), whilst Holli et al. have demonstrated that co-occurrence matrix features are significantly different between invasive lobular carcinoma and invasive ductal carcinoma (91). Similarly, texture features have also been used in brain, liver and prostate studies to distinguish between types of tumours and between benign and malignant disease (92-94).

There is also evidence that tumour heterogeneity on contrast-enhanced CT imaging is an independent predictor of response to therapy and survival. Goh et al. studied patients with renal carcinoma treated with TKIs and found that changes in texture features related to heterogeneity of CT images are independent predictors of time to progression (76). Ganeshan et al. analysed textural features in unenhanced CT scans of oesophageal carcinoma and concluded that these features are related to SUV parameters in corresponding ^{18}F-FDG PET scans and to tumour stage and survival (77).

MRI texture features have also been shown to predict response to treatment. Texture features change during treatment in non-Hodgkin's lymphoma (95), coherence and fractal dimension predict response in limb sarcomas (96), and low fractal dimension is associated with better response in colorectal cancer (97). Recently studies have correlated texture parameters on CT with survival in NSCLC (78), glucose metabolism (98) and histological correlations, including angiogenic and hypoxia markers (75). Segal et al. showed that with a number of image characteristics in hepatocellular carcinoma, including a texture heterogeneity score and estimated percentage of necrosis on contrast enhanced CT images, it is possible to reconstruct the majority of the gene expression profiles, revealing cell proliferation, liver synthetic function and patient prognosis (99).

In conclusion, clinical images contain more information than is routinely used. Additional information can easily be extracted to describe and quantify the spatial distribution of voxel intensities (textural features) from conventional radiological images and from PET images obtained using ^{18}F-FDG and other tracers. Texture features of CT and MRI have shown the ability to characterise tissues as well as predict treatment response and survival in some tumour types. Recent interest in texture analysis of functional imaging, including ^{18}F-FDG PET, has shown similar properties, although the biological mechanisms are unproven.

Further work is required to understand the biological basis of image texture in ^{18}F-FDG PET and to further validate the methodology in different cancers. It remains to be seen whether texture analysis of other metabolic tracers, e.g. ^{11}C- or ^{18}F-choline, or tracers reflecting other aspects of tumour biology such as proliferation with ^{18}F-FLT (fluorothymidine), angiogenesis/ integrin expression with labelled R-G-D compounds or hypoxia-selective agents, may produce similar results.

Seeking more powerful imaging biomarkers through texture analysis is of high relevance to modern cancer treatment where the aim is to personalise treatment through non-invasive molecular and genomic profiling of tumours.

CHAPTER 2

AIMS AND HYPOTHESES

Texture analysis helps us quantify various aspects of the tumour microenvironment which is not obvious to naked eye. As I discussed in the previous chapter, texture parameters extracted from images have been shown to be associated with some features of tumour biology. Texture analysis also has been shown to help predict prognosis in patients with cancer and help stratify patients for individual treatment pathways. However, there are limited data in the literature regarding texture analysis in PET imaging compared to other imaging modalities and hence a need for further research studies. With numerous new treatment modalities available in treatment of thoracic malignancies such as NSCLC and malignant pleural mesothelioma (MPM), it is prudent to able to get as much information as possible to guide and choose appropriate treatment for individual patients.

2.1 Hypotheses

1. Measurement of heterogeneity parameters (textural features) may be more prognostic than the conventional metrics such as SUV parameters, TLG and metabolic tumour value (MTV) in MPM.
2. There is a relationship between ^{18}F-FDG heterogeneity and tumour biology as measured by histopathological and IHC parameters in NSCLC.

2.2 Aims

1. To determine if texture features derived from baseline ^{18}F-FDG PET images of MPM are associated with overall survival in patients
2. To determine if textural parameters of ^{18}F-FDG PET/CT images of untreated NSCLC correlate with histological and IHC parameters in order to obtain a better understanding of the biological factors that cause spatial heterogeneity of ^{18}F-FDG PET images.

Chapter 3, 4 and 5 describe Methods and Results from two experiments addressing the above two aims.

CHAPTER 3

GENERAL METHODS

3.1 ^{18}F-FDG imaging

In this section I will describe the imaging performed for both my experiment chapters.

3.1.1 Patient preparation

Patients fasted for approximately 4–6 hours prior to the ^{18}F-FDG PET-CT scan to enhance ^{18}F-FDG uptake by tumours. They were allowed to have water during this period. Before injection of ^{18}F-FDG, the blood glucose level was measured and the patients were only injected if the blood sugar level was less than 10mmol/L. Good control of blood glucose was essential because, as explained in the introduction chapter, ^{18}F-FDG and glucose use the common transport mechanism (GLUT) in both normal and tumour cells. Patients were also instructed to avoid any kind of strenuous activity prior to the examination.

3.1.2 ^{18}F-FDG dose and uptake period

We administered median 320 MBq, range: 303 MBq to 373 MBq of ^{18}F-FDG intravenously. Following injection of the radioisotope the patients are placed in a quiet area in a cubicle for 90 minutes for the MPM patients in chapter 4 and 60 minutes for NSCLC patients in chapter 5. Patients were asked to limit any movements including speech to avoid physiologic muscle uptake of ^{18}F-FDG.

3.1.3 Image acquisition

^{18}F-FDG PET/CT scans were acquired using our standard institutional clinical imaging protocol for oncology. All MPM patients in chapter 4 were scanned on one of the two scanners Discovery VCT or DST, GE Healthcare, Chicago, USA and all NSCLC patients in chapter 5 were scanned with Discovery 710, GE Healthcare, Chicago, USA. All ^{18}F-FDG PET/CT scans were performed at 90 minutes (mean 89.7±9.3 minutes) post-injection for the MPM patients in chapter 4 and after 60 minutes (mean 71.3±15.7 minutes) post-injection for the NSCLC patients in chapter 5.

The patients were positioned with the arms above the head as a standard protocol. If a patient is not able to maintain this position comfortably without moving for the entire study, arms by the side was used as an alternative. The CT scan took around a minute to complete and the PET study approximately 20 minutes for the half-body scan from base of skull to mid-thighs. The CT scan was used for localisation and for attenuation correction. Images were corrected for effects of attenuation for accurate image analysis.

Images were reconstructed using ordered subset expectation maximisation (OSEM, 2 iterations, 20 subsets) with a reconstructed slice thickness of 3.27 mm and pixel size 4.7mm. The CT component of PET/CT scans was acquired at 140 kVp and 65 mAs without administration of oral or intravenous contrast agent and CT data was used for attenuation correction.

3.2 Image analysis

In this section I will describe the software I used for texture analysis of PET images for both my experiment chapters.

3.2.1 Feature Analysis Software Tool (FAST)

FAST is a novel in-house built quantitative analysis software package, developed by the Cancer Imaging group at King's College London, for the texture analysis of PET scans among other imaging modalities. Based on a number of methods including GLCM, run-length matrix, fractal analysis, NGTDM, FAST extracts texture features that reflect the local, regional and global patterns of image heterogeneity.

The FAST can import both PET and CT images simultaneously in DICOM format and can align them. The FAST allows the images to be displayed in axial, coronal or sagittal views and can magnify the images and adjust the contrast.

Once the images were imported, I then was able to draw ROIs in 3D on the PET image to separate the object of interest from the background. The same region was automatically overlaid to the CT component of PET so that the properties from both modalities were computed for the same region. For the purposes of my thesis I only used the data extracted from PET images. The regions were refined using various image segmentation methods based on thresholding for the MPM patients in chapter 4 and fuzzy logic techniques for NSCLC patients in chapter 5. The fuzzy logic technique could not be used in MPM due to irregular and non-contiguous regions.

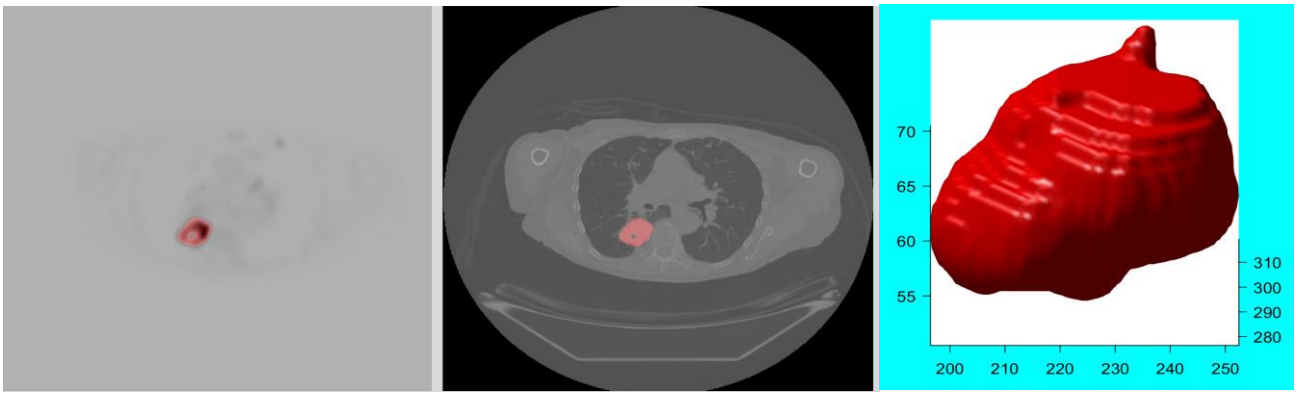

Figure 4. ROI drawn on FAST on axial images in a patient with right lower lobe NSCLC (left hand side and central images) and 3-D image of the tumour extracted from the ROI drawn

The FAST software then extracted a suite of first-order, second-order and high-order textural parameters based on intensity distribution and region geometry and results were automatically exported into an excel spread sheet. The software also calculated the SUV_{max}, SUV_{mean}, SUV_{peak}, TLG and MTV. Appendix 1 lists different textural parameters commonly used in the literature including the parameters used in the experiment chapters of my thesis.

CHAPTER 4

ASSOCIATION OF TEXTURE FEATURES DERIVED FROM ^{18}F-FDG PET IMAGES OF MALIGNANT PLEURAL MESOTHELIOMA WITH OVERALL PATIENT SURVIVAL

4.1 Introduction

MPM is a highly aggressive primary tumour of the pleura with very poor prognosis. MPM is causally linked to asbestos exposure in most cases. The median survival from diagnosis is less than 12 months and most patients die within 10–17 months of their first symptoms (100, 101).

The incidence of MPM has increased in industrialised nations because of past widespread exposure to asbestos (101). Asbestos is still in use in some countries especially the developing countries and hence the incidence of MPM is predicted to increase further in coming decades (102).

Multimodality treatment with surgery, chemotherapy and radiotherapy is most commonly offered to MPM patients. Although multimodality treatment regimens have improved survival, overall outcomes are still poor (100, 103).

There is a need for more targeted and more effective therapies, but this needs a better understanding of the tumour biology, particularly given that MPM is a heterogeneous tumour. A better understanding of tumour biology will help in future tailoring individual treatment plans.

^{18}F-FDG PET/CT is widely used for diagnosis and staging of MPM and also in differentiating it from benign pleural disease (104-106). There is growing interest in use of ^{18}F-FDG PET/CT for the prediction of survival at baseline and also in therapy response evaluation (107-109).

There have been studies from our institution and others which assessed the association of ^{18}F-FDG PET/CT standard parameters with survival in MPM (108, 110).

Recently there has been increasing interest in tumour heterogeneity measured using textural analysis of the distribution ^{18}F-FDG PET/CT in some cancers (32, 34, 35, 111, 112). Additional features, extracted by computational post processing techniques, which can have prognostic value and may reflect the tumour phenotype and genotype. It is hoped that textural features may allow better tissue characterisation and better stratification of MPM for treatment, thus improving the individualisation of targeted therapies.

4.2 Aims and hypotheses

The study hypothesis was that parameters derived from ^{18}F-FDG PET image heterogeneity at baseline have prognostic significance in MPM. The aim of this retrospective study was to determine if baseline standard and texture features derived from ^{18}F-FDG PET images of MPM were associated with overall survival in a retrospective cohort of patients scanned in our institution.

4.3 Material and methods

4.3.1 Subjects

This retrospective study received institutional review board approval and requirement for informed consent was waived. All pre-treatment staging ^{18}F-FDG PET/CT scans performed in patients with MPM at our institution between January 2006 and December 2011 were selected from the institutional PET database. For inclusion in this study, patients should

have undergone a whole-body (base of skull to upper thighs) ^{18}F-FDG PET/CT as a part of their routine staging procedure prior to therapy. Patients who had a pleurodesis prior to the PET scan were excluded to avoid false positives from the non-malignant uptake of ^{18}F-FDG that results from this procedure (113). Patients with tumour volumes <5cm^3 were also excluded (n=2; see section 4.3.2 for further information).

Fifty-eight consecutive patients (mean age 64.4 years, 51 male) comprised the final cohort. Demographic and clinicopathological data, including histological subtype, treatment details and overall survival (OS) were collected.

4.3.2 Image analysis

One observer (SC) experienced in ^{18}F-FDG PET in MPM and ROI definition, analysed all 58 scans. ROIs were drawn on each slice of the scan and the VOI of the primary tumour on ^{18}F-FDG PET images was generated using a predefined threshold of 40% of the maximum pixel intensity with adjustments by the operator if non-tumoural areas of activity were incorrectly included within the VOI (111, 114). This procedure was repeated to include all metabolically active tumour even if it was not on contiguous slices. For non-contiguous tumours we limited our image analysis to the largest 3 VOIs for texture analysis. All the VOIs used for texture analysis also included SUV_{max} and SUV_{peak} regions. All VOIs were summed to calculate a MTV. TLG was calculated as the product of MTV and SUV_{mean}. Only the primary tumour was included in the image analysis, excluding any adjacent nodal disease, if present. Images were analysed for texture parameters previously found to have predictive and/or prognostic ability including first-order features (SD, skewness, kurtosis, entropy and energy

(115, 116)) and high-order features (coarseness, contrast, busyness and complexity (33, 45, 48, 115)).

Calculation of the texture features was performed using in-house software implemented with MATLAB (MathWorks, Natick, Mass, US). Voxel values within the tumour VOI were resampled to yield 32 discrete bins.

Since the inclusion of small tumour volumes can bias tracer uptake heterogeneity-based studies, we empirically chose $5cm^3$ as the minimum threshold volume based on other similar studies (33, 117). Brooks et al. (118) described a method to evaluate minimum volume to give 95% certainty that the global intensity distribution has been sampled adequately. We determined that by this method our minimum volume threshold was less than $5cm^3$ in our study.

4.3.3 Statistical Analysis

TLG required log transformation. The outcome of interest was patient survival. Subgroup analyses of individual histological types could not be undertaken because of the small number of patients in each non-epithelioid group.

Cox regression analysis was used to examine the effects of the PET parameters and other variables upon the survival outcomes and was performed in two stages. Initially, a univariable model was used to test the individual association of each variable with survival times. Results were expressed as hazard ratios (HR) and their confidence intervals (CI). For categorical variables, the HR represent the relative change in the risk of death when the factor was present compared to when it was absent. For continuous variables, the HR represent the relative change in the risk of death for a one-unit increase in that variable,

unless one-unit is a small or larger amount, in which case effects are reported for different sized increases.

Entering variables identified as significantly associated with survival from the univariable model; a multivariable model was then created to examine the joint effect of the variables. To reduce the number of parameters in this stage of the analysis, a backward selection procedure was used, i.e. only those showing some evidence of an association with survival from the univariable analyses were included and we chose an arbitrary cut-off of $p<0.1$. Before the multivariable analysis was performed, the collinearity between predictor variables was examined. Where there was found to be collinearity between variables (variance inflation factor > 10), one or more variables was excluded from the multivariable analysis, e.g. SUV_{peak}, SUV_{mean} and MTV. MTV was excluded in favour of TLG.

The time in months between the PET scan and the date of death was defined as overall survival. The time between PET scans and last censor was recorded in surviving patients. Kaplan-Meier curves were generated for factors found to be significant predictors on multivariable analysis. For the purposes of the graphs the parameters were divided into two approximately equal groups. A p value of less than 0.05 was considered statistically significant.

4.4 Results

The mean/median and SD/range for each standard and texture parameter is presented in Table 3.

Table 3. Mean/median and standard deviation/range for each standard and texture parameter

Standard/Texture feature	Mean(Median)	SD(Range)
SUV_{max} (*)	12 .06 (11.28)	5.82 (2.16 – 28.44)
Log-TLG	6.34 (6.48)	1.46 (2.02 – 9.59)
SD	3.45 (2.95)	2.08 (0.62 – 8.45)
Skewness	1.19 (1.14)	0.53 (0.34 – 2.89)
Kurtosis	4.89 (4.19)	2.67 (2.08 – 18.85)
First-order entropy	2.28 (2.24)	0.61 (1.06 – 3.41)
First-order energy (*)	0.15 (0.13)	0.09 (0.04 – 0.39)
Coarseness (**)	0.00130 (0.00046)	0.00188 (0.00010 – 0.01063)
Contrast	3.11 (1.88)	3.08 (0.12 – 13.00)
Busyness (*)	11.02 (9.00)	9.19 (0.63 – 40.88)
Complexity (***)	273.96 (274.50)	78.50 (140.49 – 500.55)

The HR calculated using the univariable model are presented in Table 4, indicating the change in the risk of death at any time for each variable. The univariable analysis suggested that several of the variables examined were significantly ($p<0.05$) associated with patient survival.

Table 4. Hazard ratios calculated using the univariable model

Variable	Hazard Ratio (95% CI)	P-value
Male gender	1.71 (0.61, 4.77)	0.31
Non-Epithelioid histology	2.13 (1.11, 4.08)	**0.02**
Age (**)	1.01 (0.67, 1.52)	0.97
SUVmax (*)	1.20 (0.96, 1.51)	0.11
Log-TLG	1.33 (1.07, 1.67)	**0.01**
SD	1.13 (0.99, 1.29)	0.08
Skewness	1.04 (0.61, 1.77)	0.89
Kurtosis	1.01 (0.92, 1.11)	0.85
First-order entropy	1.61 (1.02, 2.56)	**0.04**
First-order energy (†)	0.68 (0.48, 0.96)	**0.03**
Coarseness (††)	0.84 (0.69, 1.03)	0.09
Contrast	1.10 (1.00, 1.21)	0.06
Busyness (*)	1.09 (0.95, 1.25)	0.20
Complexity (***)	0.80 (0.67, 0.97)	**0.02**

(†) HR reported for a 0.1-unit increase in predictor variable
(††) HR reported for a 0.001-unit increase in predictor variable
(*) HR reported for a 5-unit increase in predictor variable
(**) HR reported for a 10-unit increase in predictor variable
(***) HR reported for a 50-unit increase in predictor variable

Histological subgroups included epithelioid (n=30), sarcomatoid (n=5), mixed (n= 13), desmoplastic (n=2) and unknown (n=8). Histology was significantly associated with survival when patients were split in to epithelioid and non-epithelioid groups. Patients with a non-epithelioid histology had a higher risk of death, and thus shorter survival times. The risk of death at any time was more than twice as high compared to patients with epithelioid histology.

There was some evidence that some standard parameters were associated with survival, with higher SUV_{max} and log-TLG values associated with an increased risk of death. However, the result was not statistically significant for SUV_{max}.

Of the texture parameters first-order entropy, first-order energy and complexity were all significantly associated with survival. Higher values of first-order entropy were associated with an increased risk of death and thus shorter survival time. For example, one-unit increase in first-order entropy was associated with a 61% increase in the risk of death at any time. Higher values of first-order energy and complexity were associated with a lower risk of death. For example, a 0.1-unit increase in first-order energy was associated with a reduction in the risk of death at any time of around a third.

Before the multivariable analysis was performed, collinearity between predictor variables was examined. For example, first-order entropy and first-order energy were found to be highly collinear and therefore only first-order entropy was retained for the analyses.

Histology, TLG, first-order entropy, complexity, coarseness, contrast and SD were used for multivariable analysis. The data was dichotomised around the median value for analyses. The results of the multivariable analyses (Table 5) indicated that first-order entropy was independently associated with patient survival (p= 0.03), whilst non-epithelioid histology and coarseness were of borderline significance (p = 0.05 and 0.06, respectively) but these variables were retained in the final model.

Table 5. Results of the multivariable analyses

Variable	Hazard Ratio (95% CI)	P-value
Non-Epithelioid histology	1.92 (1.00, 3.70)	0.05
First-order entropy	1.75 (1.07, 2.89)	**0.03**
Coarseness (††)	0.80 (0.63, 1.01)	0.06

(††) Hazard ratio reported for a 0.001-unit increase in predictor variable

A graphical illustration of the results for first-order entropy (figure 5) and coarseness (figure 6) is shown in a Kaplan-Meier graph.

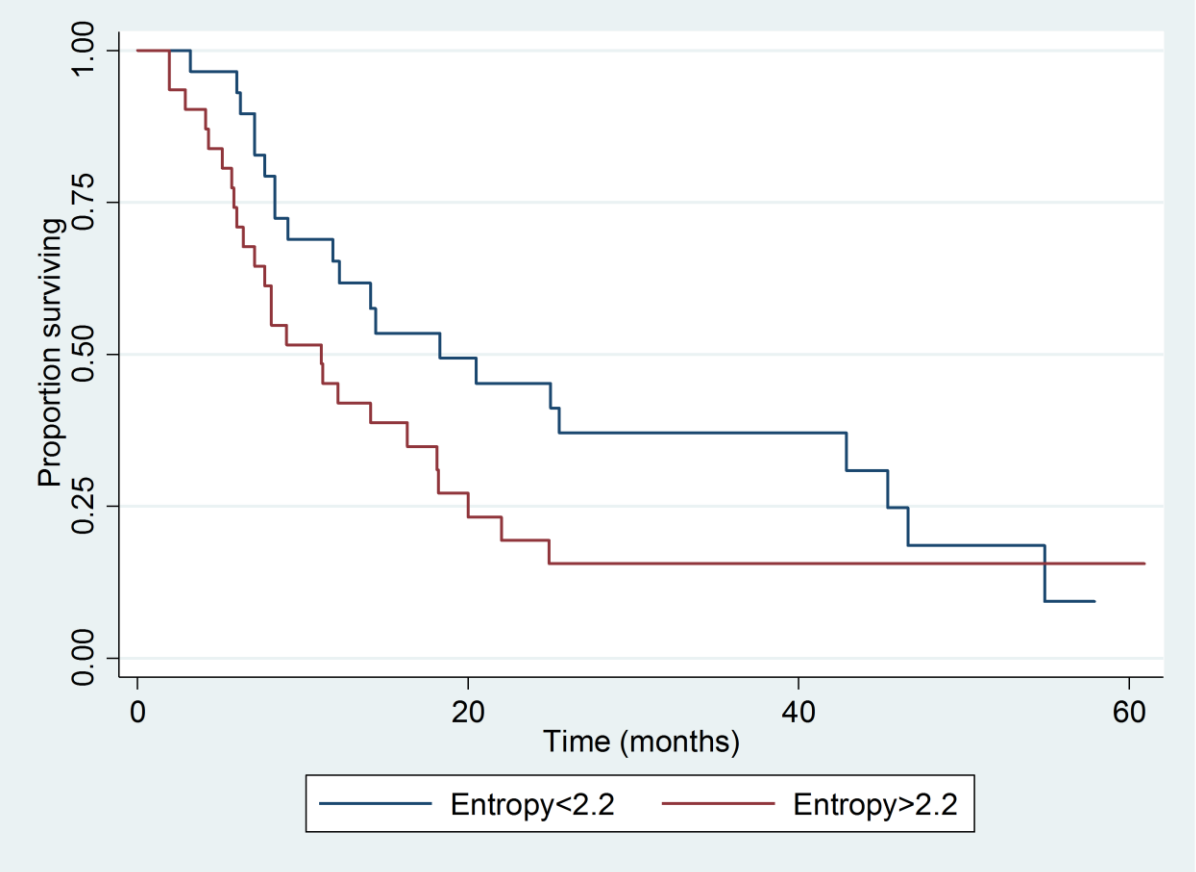

Figure 5. Results for first-order entropy in a Kaplan-Meier graph

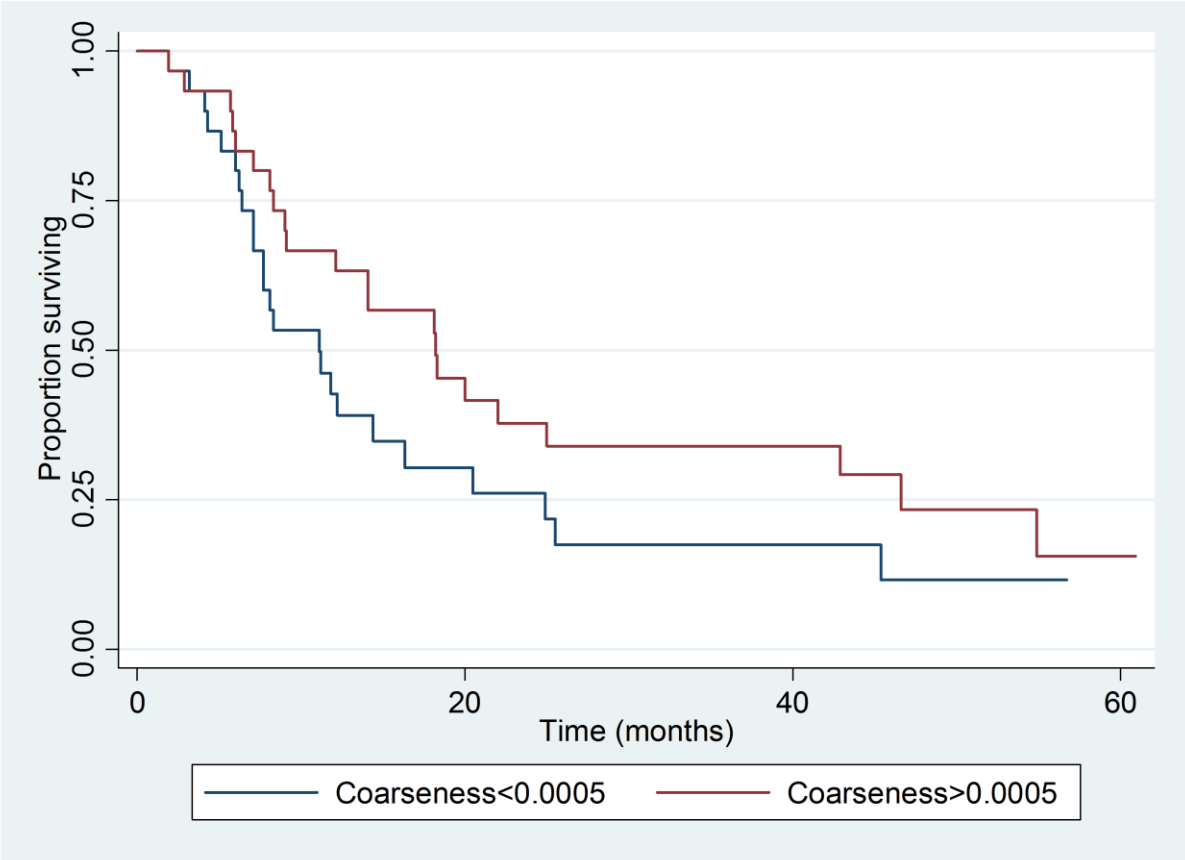

Figure 6. Results for coarseness in a Kaplan-Meier graph

Correlations between first-order entropy and both SUV_{max} and MTV were tested. First-order entropy did not show a significant correlation with MTV ($r^2 = 0.01$, $p>0.05$). A correlation was found between first-order entropy and SUV_{max} ($r^2 = 0.63$, $p=0.005$).

4.5 Discussion

In this study we investigated the prognostic significance of parameters derived from baseline, pre-treatment ^{18}F-FDG PET image heterogeneity in MPM. The results of our retrospective analysis of 58 ^{18}F-FDG PET scans have shown that non-epithelioid histology, standard PET parameters (SUV_{max}, TLG) as well as heterogeneity parameters (first-order entropy, first-order energy, coarseness, contrast, SD and complexity) are associated with

prognosis on univariable analysis. On multivariable analysis first-order entropy remained a significant independent predictor of survival. A one-unit increase in first-order entropy was associated with a 75% increase in the risk of death at any time.

We believe this is the first study to describe a relationship between heterogeneity in ^{18}F-FDG PET images and survival in MPM patients. We and others have previously described the prognostic ability of standard PET parameters that take into account functional volume (MTV, TLG) (110, 119-121). In the current study, whilst TLG showed an association in univariable analysis, only first-order entropy was an independent predictor on multivariable analysis, suggesting that a measure of heterogeneity may be a superior predictor over standard parameters that do not take heterogeneity of activity into account.

Biologic and genomic tumoural heterogeneity is known as an adverse feature in cancer and probably underlies treatment failure as resistant clones survive (122). Similarly, imaging heterogeneity has been associated with adverse features in thoracic malignancy including poor treatment response and survival (63, 69, 71, 77, 78, 111, 112).

There have been several recently published studies evaluating textural PET parameters and their role in predicting patient survival and treatment response. A study of 41 patients with newly diagnosed oesophageal cancer noted that tumour texture features extracted from baseline ^{18}F-FDG PET images allow for the best stratification of patients in the context of therapy-response prediction (33). Wu et al. (123) concluded in their study on 101 patients with early-stage NSCLC that intratumoural heterogeneity of ^{18}F-FDG PET could predict distant metastases, a feature that could potentially help to stratify patients to appropriate treatment pathways early on at the time of diagnosis.

Specifically, first-order entropy is a feature that is not only reproducible and robust (48, 124-126) but has been shown to be predictive and prognostic in a number of cancers (63, 127,

128). In a recent study by Hatt et al. (129) of 101 NSCLC patients with ^{18}F-FDG PET scans first-order entropy was found to be one of the significant prognostic factors for overall survival prediction; similar to our study findings. First-order entropy is also independently associated with overall survival and treatment response to a TKI in a study of 47 patients with NSCLC (63).

Whilst heterogeneity parameters may be subject to bias at small volumes and may act as surrogates of size (118), we found no significant correlation between first-order entropy and MTV in our data. In contrast, we have noted a correlation with SUV_{max} even though SUV and first-order entropy measure different characteristics. The likely cause is that greater first-order entropy of voxel intensities is more likely in tumours with high SUV_{max} (and associated larger spread of voxel intensities) than in tumours with low SUV_{max}. Our dataset contained a wide range of intensities (SUV_{max} ranging from 2.16 to 28.44 and correlations between SUV parameters and first-order heterogeneity parameters are therefore not unexpected. A dataset with a smaller range of SUV parameters between subjects would be expected to show weaker or absent correlations.

My study has some limitations. I excluded patients who had a previous pleurodesis. This was necessary to avoid non-tumoural ^{18}F-FDG activity that occurs as a consequence of the inflammatory reaction in the pleura that follows pleurodesis (113). My results therefore cannot be extrapolated to patients following pleurodesis.

With regards to analysing the influence of histology, I could not fully determine the influence of all histological subtypes separately on the prognosis, as the non-epithelioid (sarcomatoid, mixed and desmoplastic) histology subtypes were grouped together in my

analysis. Apart from the epithelioid group, the number of patients in each non-epithelioid subgroup was too small for reliable analysis.

4.6 Conclusion

First-order entropy has prognostic ability by predicting overall survival in MPM patients. This is superior to the currently used standard PET SUV parameters.

CHAPTER 5

TEXTURAL FEATURES OF NON-SMALL-CELL LUNG CANCER ON PRE-TREATMENT ^{18}F-FDG PET/CT AND CORRELATION WITH HISTOLOGICAL PARAMETERS

5.1 Introduction

NSCLC remains the leading cause of cancer related death, worldwide (130). It represents approximately 85–90% of all lung cancers and its incidence is rising. The two main subtypes are ADC and SCC. ADC accounts for 50% of all lung cancer and its incidence has increased greatly in recent years (131). The prognosis of patients with NSCLC is poor despite many treatment options available and hence there is a need for reliable markers to guide treatment decisions, especially in this era of precision medicine. Tailoring the best individual management pathway that identifies the best therapeutic strategy for each patient, based on clinical and biological characteristics of the disease in an individual patient is crucial. Several prognostic factors have been identified, such as gender, performance status, histology, biomolecular features and stage, in order to identify subgroups of patients with different prognoses and thus candidates for different therapeutic options (132-134). Within the two main histological subtypes (ADC and SCC), different growth patterns are present and are associated with different grading and prognosis (135). In particular, ADC includes various invasive patterns belonging to three prognostic groups, including lepidic pattern, grade 1, acinar and papillary pattern, grade 2, micropapillary and solid pattern, grade 3. SCC provides three variants: keratinising, non-keratinising and basaloid form (133). The micropapillary and solid pattern subtypes of ADC are associated with a higher risk of

metastases and poorer prognosis compared to lepidic ADCs which are usually associated with lower risk and better prognosis (136). Acinar and papillary ADC are generally in an intermediate group, with a less predictable impact on patients' outcome (137). The keratinisation in SCC is associated with a poor prognosis and might be associated with smoking (138).

Lung cancer is often a heterogeneous tumour with different subtypes and growth patterns within the same tumour. However, it is not always possible to identify these differences on histopathology specimens. Other factors such as immune cell tumour infiltration and angiogenesis also influence tumour prognosis and treatment response, especially immunotherapy (139). One of the main problems related to the subtype classification system and to the detection of tumour morphological characteristics is that it is subject to considerable inter- and intra-observer variation and a subjective interpretation of highly complex pathological images by a pathologist (133).

It is known that malignant tumours including NSCLC exhibit intra-tumoural biologic heterogeneity and this heterogeneity is postulated to correlate with histological features such as cellular proliferation, necrosis, fibrous tissue, differences in blood flow, cellular metabolism, oxygenation, and expression of specific receptors. Hypoxia, which exists in varying degree in tumours, is one of the driving forces (140). Through selection pressures, hypoxia alters local expressions of p53, E-cadherin, hypoxia inducible factor–1 (HIF-1) alpha, GLUT-1 (increased glycolysis), and cluster of differentiation 34 (CD34; angiogenesis) and allows emergence of new cancer clones that are well adapted to the local environment (141-143). CD34 is a surface antigen expressed in the vascular endothelial cells with life-long expression; and does not distinguish between normal and tumour vessels (144). CD105 in

contrast is expressed only in tumour blood vessels and not present in normal endothelial cells (145).

The current gold standard for tumour analysis in oncology practice is histopathology and IHC but these are subject to biopsy sampling error. Imaging augments histopathological and IHC measures in this scenario as the whole tumour and its microenvironment can be noninvasively interrogated and hence capture the heterogeneity of not only the primary malignancy but also the underlying molecular and cellular processes between different tumours in the same patient (87).

^{18}F-FDG PET/CT is routinely used in oncologic imaging for diagnosis and staging and increasingly to determine early response to treatment, often employing semi-quantitative measures of lesion activity such as the SUV (19-21, 146, 147). However, the ability to predict the behaviour of a tumour in terms of future therapy response or prognosis using SUVs from a baseline scan prior to treatment is limited. ^{18}F-FDG uptake has been associated with various factors such as perfusion, cell proliferation, tumour viability, aggressiveness, and hypoxia (148).

In NSCLC, the ability of ^{18}F-FDG PET to predict histopathological response to chemoradiotherapy has been described (149, 150). There is only limited evidence that the level of uptake on pre-treatment scans, as measured by various SUV parameters, may be predictive but results sometimes conflict as to whether high or low SUVs are predictive depending on treatment modality, e.g. radiotherapy vs chemotherapy in NSCLC (18-21). Also, in NSCLC there are data that show that the baseline SUV prior to therapy may be prognostic with low values being associated with longer survival but the optimal cut off SUV varies widely in the literature (151-155).

In recent years, evidence has slowly accumulated showing that parameters obtained by texture analysis of radiological images, reflecting the underlying spatial variation and heterogeneity of voxel intensities within a tumour, may yield additional predictive and prognostic information (33, 45). It is hoped that measurement of these textural features may allow better tissue characterisation as well as better stratification of treatment in clinical trials, or individualisation of future cancer treatment in the clinic, than is possible with current imaging biomarkers. Whilst the data have been rapidly accumulating for contrast enhanced CT and MRI in this field, the evidence for texture analysis within PET imaging is only just emerging.

Cook et al. in their recent review discussed the role of PET and texture features in NSCLC (87). They discussed that PET provides macroscopic information on aberrant molecular pathways and altered cellular biology in cancer which allows most of the hallmarks of cancer to be imaged and quantified (156). Measurement of these cellular processes that have histopathological correlates is crucial to the understanding of individual tumour phenotypes, helping us understand how a tumour will behave with regard to local invasion or metastatic potential, understand the relationship and interaction of tumour cells with the microenvironment, and predict and monitor response or resistance to therapy (87).

As I discussed in the introduction chapter of the thesis, the study of radiomics is of academic interest since it has been recognised that genetic heterogeneity exists within tumours and between metastatic tumours in the same patient. Heterogeneity of the tumour microenvironment with respect to cellular density, proliferation, angiogenesis, hypoxia, receptor expression, necrosis, fibrosis, and inflammation might be reflected in medical images and that these factors can contribute to poor treatment responses and a more aggressive phenotype (157).

A variety of textural features that describe the spatial variation of voxel intensities in ^{18}F-FDG PET/CT images of untreated NSCLC have been shown to predict treatment response and survival. Tumour heterogeneity in baseline imaging may predict survival and therapy response (28-35). However, the correlation of tumour biology to textural features is largely not understood.

PET has relatively large voxels compared with MRI and CT, and the ability to accurately measure heterogeneity features without bias or dependence on volume is therefore more challenging. Using probability theory, Brooks et al. calculated that a volume of 45 cm^3 is required to adequately sample the tumour for measurement of second-order entropy without significant bias on ^{18}F-FDG PET images of cervical cancer (118). Hatt et al. in their study reported that several texture features are highly correlated with tumour volume, that the correlation varies among different features, and the level of correlation significantly decreases with larger volume tumours (129). For example, second-order entropy showed high correlation in volumes of <10 cm^3 but much less at volumes >10 cm^3, suggesting a much lower minimum volume than 45 cm^3 might be applicable. This demonstrated that texture features ae not just a surrogate for volume but in a subgroup of patients with NSCLC heterogeneity and volume were independent prognostic factors and therefore complementary, especially in tumours >10 cm^3 (129).

Based on this evidence I only included patients with >3cm maximum diameter (i.e. >> 10cm^3) NSCLC to avoid potential bias or volume factors.

5.2 Aims and hypotheses

The aim of my study was to correlate textural parameters of ^{18}F-FDG PET/CT images of untreated NSCLC with histological and IHC parameters in order to obtain a better understanding of the biological factors that potentially cause or are related to spatial heterogeneity of ^{18}F-FDG distribution in PET images.

The hypothesis was that the textural features of NSCLC derived from ^{18}F-FDG PET/CT are associated with specific histological features (such as angiogenesis, hypoxia, glycolysis and proliferation).

5.3 Material and methods

This was a prospective single centre non-randomised exploratory observational and pilot study. This study received approval from the Research Ethics Service committee (Chelsea, London), Health Research Authority and from Guy's and St. Thomas' NHS Foundation Trust Research and Development Directorate. A research ARSAC (Administration of Radioactive Substances Advisory Committee) certificate was also granted.

5.3.1 Subjects

I recruited patients with untreated NSCLC with the following inclusion and exclusion criteria.

Inclusion criteria:

i) Patients > 18 years old with a histological diagnosis of NSCLC.

ii) Patients planned for surgical resection without neoadjuvant treatment.

iii) Patients with clinical ^{18}F-FDG PET/CT imaging.

iv) Ability to provide informed written consent

v) Willingness and ability to comply with scheduled study visits and tests.

Exclusion criteria:

i) Concomitant uncontrolled medical conditions

ii) Patients planned for neoadjuvant chemotherapy or radiotherapy treatment prior to surgery.

iii) Primary tumour < 3cm diameter.

Demographic and clinicopathological data, including histological subtype were collected. Nineteen patients with a mean age of 70.5 years were included. Ten were male and nine were female. 10 patients had ADC, 8 had SCC and 1 had large cell neuroendocrine carcinoma (LCNC). All 19 patients had surgical resection of the tumour. All patients underwent ^{18}F-FDG PET/CT imaging a median 1 day before surgery (range: 1 day to 44 days).

5.3.2 Image analysis

Analysis was performed using in-house software implemented in MATLAB (FAST, KCL) that can measure several textural image features on PET/CT, CT and MRI and has been validated as part of the International Biomarker Standardisation Initiative (158).

Voxel values within the tumour VOI were resampled to yield 64 discrete bins, based on previously published data which demonstrated that a 64-bin quantisation scheme strikes the best compromise between minimising noise and preserving signal variation (48, 159).

Texture parameters previously found to have predictive and/or prognostic ability including first-order, second-order and high-order features were assessed (38, 51-53, 63, 64, 69, 111,

128, 129, 159-163). SUV parameters (SUV_{mean}, SUV_{max}, SUV_{peak}), MTV and TLG parameters were also derived from the same VOIs.

The reconstructed ^{18}F-FDG PET DICOM volumes from the reporting workstation (HERMES) were imported into FAST. I drew freehand (FH) ROIs around the metabolically active primary lung tumours on each axial slice on the ^{18}F-FDG PET scan to generate a VOI taking care not to include any non-tumoural regions; however, a < 5mm rim of background was included. The FH VOI served as the template for automatic segmentation using a 'fuzzy locally adaptive Bayesian' algorithm (FLAB), previously reported to be more accurate for tumour segmentation (164). Using the FLAB algorithm, the VOI voxels were categorised into three classes representing tumour core, region of partial volume averaging around tumour core and background (165). The voxels assigned to the tumour core and region of partial volume averaging were kept as the final FLAB VOI and the voxels assigned to background class was discarded.

I tested SUV_{max}, SUV_{mean}, SUV_{peak}, two tumour size related parameters (MTV and TLG) and eleven textural parameters: five first-order parameters (SD, energy, skewness, kurtosis, entropy), four second-order parameters (GLCM contrast, energy, homogeneity and entropy) and two high-order parameters (NGTDM coarseness and contrast).

5.3.3 IHC staining and post processing

The lobectomy specimens were obtained by the surgical team with the ex-vivo specimen marked such that its orientation within the body is known. The specimens were fixed in 10% buffered formalin for 24 hours prior to further processing. Two experienced consultant histopathologists (EM and DN) at Guy's and St. Thomas Hospital NHS Foundation Trust cut the surgical specimens with me present in the lab to identify the best section to be used. 3 micrometre thick tissue sections were then embedded in paraffin for IHC staining. The Biobank technicians at Guy's and St. Thomas Hospital NHS Foundation Trust based at Guy's Cancer Centre performed the IHC staining for angiogenesis (CD34 and CD105 MVD), hypoxia (HIF-1-alpha expression), glycolysis (GLUT-1 expression, HEX-II) and proliferation (Ki67).
IHC staining was performed on a Ventana Benchmark Ultra automated autostainer (Ventana Medical Systems, Inc.) using a multimer detection kit (UltraView universal DAB (diaminobenzidine tetrahydrochloride) Detection kit [760-500]). Haematoxylin II (790-2208) and bluing reagent (760-2037) were used to counterstain all IHC slides. Cell conditioning 1 was used for antigen retrieval. As the aim of my study was to correlate the micro-environment structure of the tumour to metabolic imaging, primary antibodies were used to target specific tumour micro-environment components.
The pathologists, EM and DN, scored all the slides for the 19 patients. As we had more than 1 slide for each patient, we used the average of the scores for GLUT-1%, MVD, HIF-1-alpha and Hexokinase-II (HEX-II) but for Ki67 we used both the average and maximum score. This was because maximum Ki67 score is known to correlate with clinical outcome (166).
Staining procedures and antibody descriptions are summarised in the following Table 6.

Table 6. Staining procedures summarising antigen retrieval agents and primary antibodies used in IHC staining

IHC stain	Purpose	Antigen retrieval		Primary Antibody			
		Time (minutes)	Temperature	Product name	Dilution	Time (minutes)	Temperature
CD 105	Vascular endothelial protein associated with angiogenesis (167)	64	95^{0}C	Abcam Anti-CD105 (EPR10145-10) (ab104836)	1:100	32	25^{0}C
CD 34	Vascular endothelial protein associated with angiogenesis; also highlights lymphatics (167)	64	95^{0}C	Abcam Anti-CD34 (ab185732)	1:100	32	25^{0}C
HIF-1-alpha	Protein expressed in hypoxic tumour regions (168)	36	95^{0}C	Abcam HIF-1-alpha(1A3) (ab113642)	1:200	32	25^{0}C
GLUT-1	Cell-membrane associated glucose transporter (169)	8	95^{0}C	Ventana GLUT-1 760-4526	Pre-diluted	16	37^{0}C
HEX-II	Intracellular enzyme involved in glycolysis (169)	64	95^{0}C	Abcam Anti-HEX-II (3D3) (ab104836)	1:50	32	25^{0}C
Ki67	Marker of tumour proliferation (170)	36	95^{0}C	Ventana CONFIRM anti-Ki-67 (30-9) 790-4286	Pre-diluted	16	36^{0}C

5.3.4 Statistical Analysis

The Shapiro-Wilk test for normality on SPSS (IBM SPSS Statistics, version 26) was used to check the data distribution. Based on this test, non-parametric Spearman rank correlation test was used as the data were not normally distributed. Spearman rank correlation was used to measure correlations between sixteen ^{18}F-FDG PET derived parameters and 6 IHC stains. A p-value of <0.05 was set as a cut-off to determine statistical significance for both tests. The cut-off threshold for correlation coefficient (r value) was based on the p-value thresholds and hence is different in each dataset below. A correction for multiple correlation testing was also determined. As I had 8 groups of data (SUV, first, second and high-order PET parameters; angiogenesis, hypoxia, glucose and proliferation histological parameters) the corrected p value was p= 0.05/8 = 0.006 for significance.

5.4 Results

The correlation coefficients (r value) for each standard and texture parameter versus histological parameters are presented in Table 7 for all 19 patients. Table 8 demonstrates p-values of the correlation test for the same dataset.

CD105 and CD34 MVD correlated strongly (p-value <0.05) with 3 parameters (standard and textural). CD105 MVD had a statistically significant correlation with TLG, first-order energy and NGTDM coarseness. CD34 MVD correlated strongly with MTV, TLG and NGTDM coarseness; the correlation with MTV and high-order coarseness were the strongest in the whole dataset (r> 0.6, p value < 0.01). $Ki67_{avg}$ and $Ki67_{max}$ values correlated strongly (p-value < 0.05) with GLCM energy and first-order skewness, respectively.

Although not statistically significant (p-value < 0.10 but > 0.05) there was also some correlation between the following parameters:

- Glut-1 correlated with SUV_{mean} and SUV_{peak}; first-order SD, energy and entropy; and second-order GLCM energy.
- CD105 MVD correlated with SUV_{max}, SUV_{peak} and MTV; first-order SD and entropy.
- $Ki67_{avg}$ correlated with first-order skewness.
- $Ki67_{max}$ correlated with first-order kurtosis and second-order GLCM energy.

HIF-1-alpha and HEX-II demonstrated no significant correlation with any textural features.

Figure 7 demonstrates a correlation graph matrix of statistically significant ($p < 0.05$) standard and texture parameter versus histological parameters for all 19 patients in this dataset.

If the correction for multiple correlation testing was to be applied, the only statistically significant correlation was between CD34 MVD and high-order coarseness ($p = 0.004$).

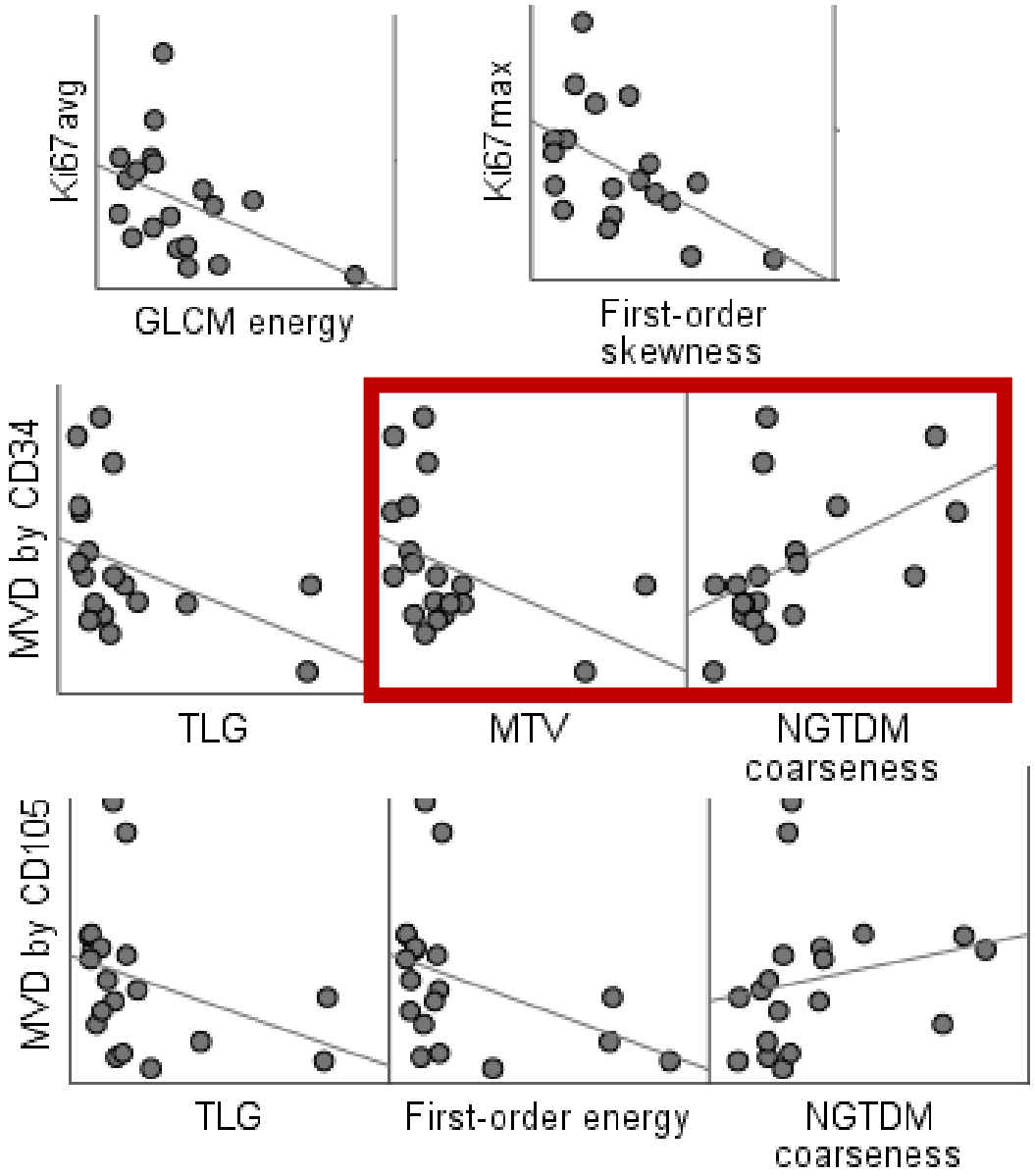

Figure 7. Correlation graph matrix of statistically significant ($p < 0.05$) standard and texture parameter versus histological parameters for all 19 patients. Graphs in red border box demonstrate strongest correlation in the dataset ($r > 0.6$, p value < 0.01)

Table 7. Correlation coefficients for each standard and texture parameter versus histological parameters for all 19 patients

Correlation Coefficient (r value)	GLUT-1 (%)	CD105 MVD	CD34 MVD	HIF-1-alpha	HEX-II	$Ki67_{avg}$	$Ki67_{max}$
SUV_{max}	0.384	-0.393	-0.172	-0.108	0.238	0.199	0.222
SUV_{mean}	0.397	-0.379	-0.162	-0.106	0.258	0.199	0.215
SUV_{peak}	0.413	-0.425	-0.191	-0.101	0.209	0.183	0.210
MTV	0.107	-0.453	-0.594	0.342	-0.233	-0.076	-0.017
TLG	0.345	-0.509	-0.496	0.239	-0.091	0.090	0.132
First-order SD	0.411	-0.419	-0.209	-0.284	0.209	0.133	0.147
First-order energy	0.397	-0.467	-0.379	0.136	0.056	0.135	0.154
First-order skewness	-0.248	0.332	0.265	-0.119	0.083	-0.441	-0.476
First-order kurtosis	-0.204	0.225	0.189	0.007	0.058	-0.385	-0.390
First-order entropy	0.391	-0.444	-0.231	-0.190	0.166	0.133	0.153
GLCM contrast	0.155	-0.093	0.096	-0.372	0.206	0.191	0.119
GLCM energy	-0.427	0.253	0.193	0.078	-0.149	-0.470	-0.417
GLCM homogeneity	-0.104	-0.060	-0.246	0.254	-0.220	-0.264	-0.226
GLCM entropy	0.210	-0.075	0.102	-0.381	0.242	0.297	0.220
NGTDM coarseness	-0.205	0.525	0.623	-0.316	0.227	0.002	-0.039
NGTDM contrast	0.116	0.014	0.217	-0.350	0.194	0.233	0.178

Legend for r value

r value	Colour code
> 0.46	
0.46 – 0.39	
< 0.39	

Table 8. Demonstrates p-values of the correlation test for all 19 patients

p-value (significance 2-tailed)	GLUT-1 (%)	CD105 MVD	CD34 MVD	HIF-1-alpha	HEX-II	$Ki67_{avg}$	$Ki67_{max}$
SUV_{max}	0.105	0.096	0.481	0.659	0.326	0.414	0.361
SUV_{mean}	0.092	0.110	0.508	0.664	0.286	0.414	0.377
SUV_{peak}	0.079	0.070	0.434	0.680	0.390	0.452	0.389
MTV	0.663	0.052	0.007	0.151	0.338	0.756	0.946
TLG	0.147	0.026	0.031	0.324	0.710	0.713	0.591
First-order SD	0.081	0.074	0.390	0.238	0.390	0.589	0.549
First-order energy	0.092	0.044	0.110	0.580	0.819	0.581	0.528
First-order skewness	0.306	0.166	0.272	0.628	0.734	0.058	0.040
First-order kurtosis	0.403	0.355	0.439	0.977	0.814	0.103	0.099
First-order entropy	0.098	0.057	0.341	0.436	0.497	0.589	0.533
GLCM contrast	0.525	0.705	0.696	0.117	0.397	0.433	0.626
GLCM energy	0.068	0.297	0.428	0.750	0.542	0.042	0.076
GLCM homogeneity	0.673	0.808	0.310	0.293	0.364	0.274	0.353
GLCM entropy	0.389	0.759	0.678	0.108	0.319	0.218	0.365
NGTDM coarseness	0.399	0.021	0.004	0.188	0.351	0.994	0.872
NGTDM contrast	0.636	0.955	0.372	0.142	0.426	0.336	0.466

Legend for p-value

p-value	Colour code
< 0.050	
0.05 – 0.1	
> 0.1	

Table 9 summarises the correlation coefficients (r value) for each standard and texture parameter versus histological parameters for patients with ADC and SCC only (n=18 patients); Table 10 demonstrates the p-values of the correlation test.

CD105 MVD had a similar correlation with TLG, first-order energy and NGTDM coarseness; first-order entropy was also statistically significant. CD34 MVD again correlated strongly with MTV, TLG and NGTDM coarseness.

Although not statistically significant (p-value < 0.10 but > 0.05) there were also some correlation between the following parameters:

- $Ki67_{avg}$ correlated with first-order skewness
- Glut-1 correlated with SUV_{max}, SUV_{mean} and SUV_{peak}; first-order SD, energy and entropy; and second-order GLCM energy.
- CD105 MVD correlated with SUV_{max}, SUV_{peak} and MTV; and first-order SD and entropy.

HIF-1-alpha and HEX-II demonstrated no significant correlation with any textural features, as seen with the previous data.

Figure 8 demonstrates a correlation graph matrix of statistically significant ($p < 0.05$) standard and texture parameter versus histological parameters for the 18 patients with ADC and SCC.

If the correction for multiple correlation testing was to be applied, the only statistically significant correlation was between CD34 MVD and high-order coarseness ($p = 0.004$), as seen with the previous data.

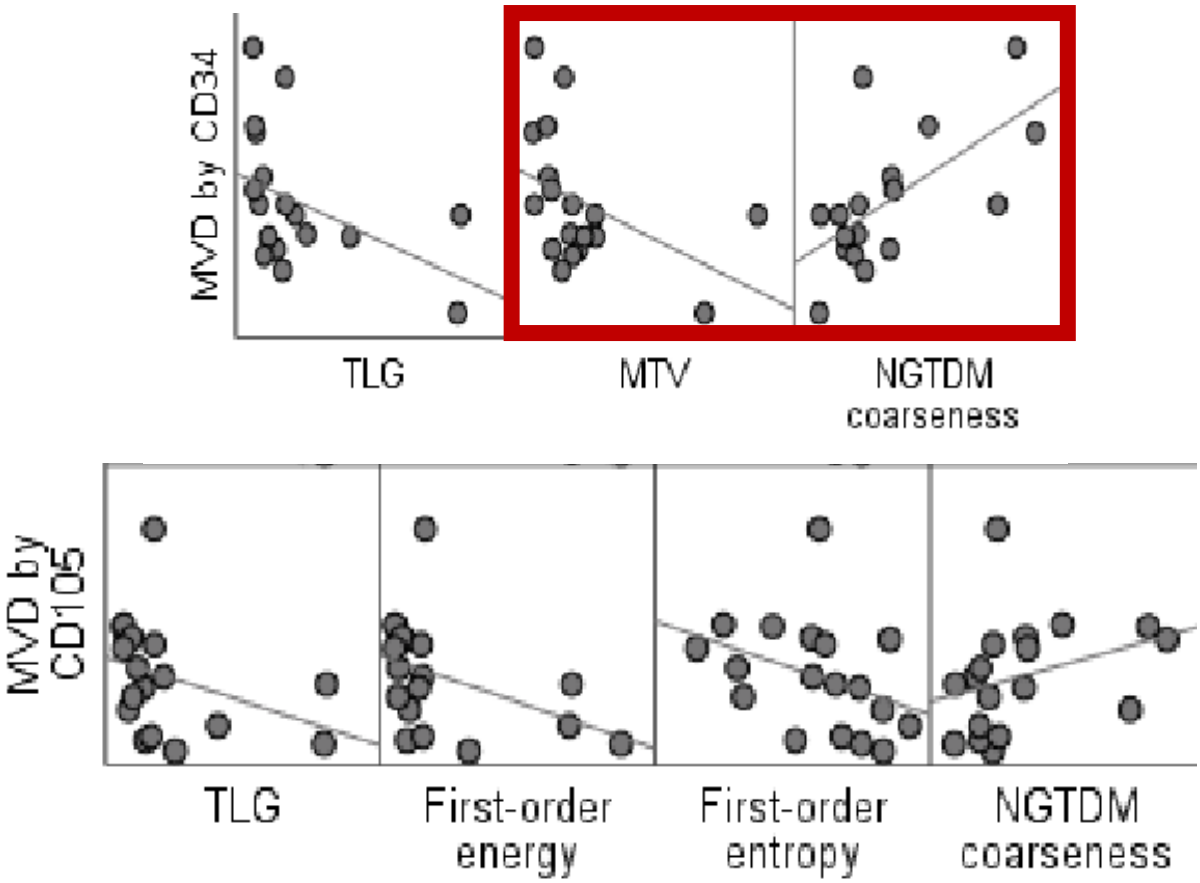

Figure 8. Correlation graph matrix of statistically significant ($p < 0.05$) standard and texture parameter versus histological parameters for 18 patients with ADC and SCC. Graphs in red border box demonstrate strongest correlation in the dataset ($r > 0.6$, p value < 0.01)

Table 9. Correlation coefficients for each standard and texture parameter versus histological parameters for 18 patients with ADC and SCC

Correlation Coefficient (r value)	GLUT-1 (%)	CD105 MVD	CD34 MVD	HIF-1-alpha	HEX-II	$Ki67_{avg}$	$Ki67_{max}$
SUV_{max}	0.405	-0.412	-0.165	-0.142	0.253	0.217	0.234
SUV_{mean}	0.418	-0.395	-0.153	-0.140	0.276	0.219	0.226
SUV_{peak}	0.437	-0.449	-0.187	-0.134	0.221	0.200	0.218
MTV	0.110	-0.449	-0.607	0.325	-0.221	-0.099	-0.026
TLG	0.352	-0.534	-0.521	0.232	-0.084	0.072	0.120
First-order SD	0.425	-0.457	-0.229	-0.276	0.222	0.163	0.178
First-order energy	0.403	-0.517	-0.413	0.130	0.066	0.131	0.153
First-order skewness	-0.230	0.255	0.185	-0.035	0.049	-0.427	-0.449
First-order kurtosis	-0.186	0.181	0.149	0.032	0.036	-0.327	-0.379
First-order entropy	0.409	-0.474	-0.239	-0.204	0.186	0.153	0.167
GLCM contrast	0.192	-0.170	0.037	-0.339	0.198	0.240	0.167
GLCM energy	-0.406	0.245	0.182	0.096	-0.164	-0.451	-0.390
GLCM homogeneity	-0.103	-0.086	-0.289	0.289	-0.237	-0.285	-0.223
GLCM entropy	0.248	-0.150	0.044	-0.346	0.233	0.353	0.278
NGTDM coarseness	-0.219	0.534	0.641	-0.295	0.212	0.015	-0.036
NGTDM contrast	0.147	-0.044	0.180	-0.312	0.184	0.287	0.232

Legend for r value

r value	Colour code
> 0.47	
0.47 – 0.40	
< 0.40	

Table 10. Demonstrates p-values of the correlation test for 18 patients with ADC and SCC

p-value (significance 2-tailed)	GLUT-1 (%)	CD105 MVD	CD34 MVD	HIF-1-alpha	HEX-II	$Ki67_{avg}$	$Ki67_{max}$
SUV_{max}	0.096	0.090	0.512	0.575	0.311	0.387	0.349
SUV_{mean}	0.084	0.104	0.544	0.580	0.268	0.383	0.367
SUV_{peak}	0.070	0.062	0.457	0.597	0.378	0.425	0.385
MTV	0.665	0.062	0.008	0.188	0.378	0.696	0.919
TLG	0.152	0.023	0.027	0.355	0.741	0.776	0.636
First-order SD	0.079	0.056	0.362	0.267	0.376	0.518	0.481
First-order energy	0.097	0.028	0.089	0.606	0.794	0.604	0.545
First-order skewness	0.359	0.307	0.462	0.890	0.848	0.077	0.062
First-order kurtosis	0.459	0.473	0.555	0.899	0.887	0.129	0.121
First-order entropy	0.092	0.047	0.340	0.417	0.460	0.545	0.507
GLCM contrast	0.446	0.499	0.883	0.169	0.430	0.338	0.507
GLCM energy	0.095	0.328	0.470	0.704	0.515	0.060	0.109
GLCM homogeneity	0.684	0.735	0.246	0.245	0.345	0.252	0.374
GLCM entropy	0.322	0.553	0.861	0.160	0.351	0.151	0.264
NGTDM coarseness	0.382	0.023	0.004	0.235	0.399	0.951	0.887
NGTDM contrast	0.559	0.861	0.475	0.208	0.465	0.248	0.354

Legend for p-value

p-value	Colour code
< 0.050	
0.05 – 0.1	
> 0.1	

Table 11 demonstrates correlation coefficients (r value) for each standard and texture parameter versus histological parameters for the 10 ADC patients only; Table 12 demonstrates the p-values of the correlation test.

CD105 and CD34 MVD correlated strongly with both MTV and NGTDM coarseness. The correlation with NGTDM coarseness was the strongest in the whole dataset for ADC ($r = 0.77$, $p < 0.01$). None of the other standard or textural parameters demonstrated any significant correlation with any of the histological parameters.

Figure 9 demonstrates a correlation graph matrix of statistically significant ($p < 0.05$) standard and texture parameter versus histological parameters for 10 patients with ADC.

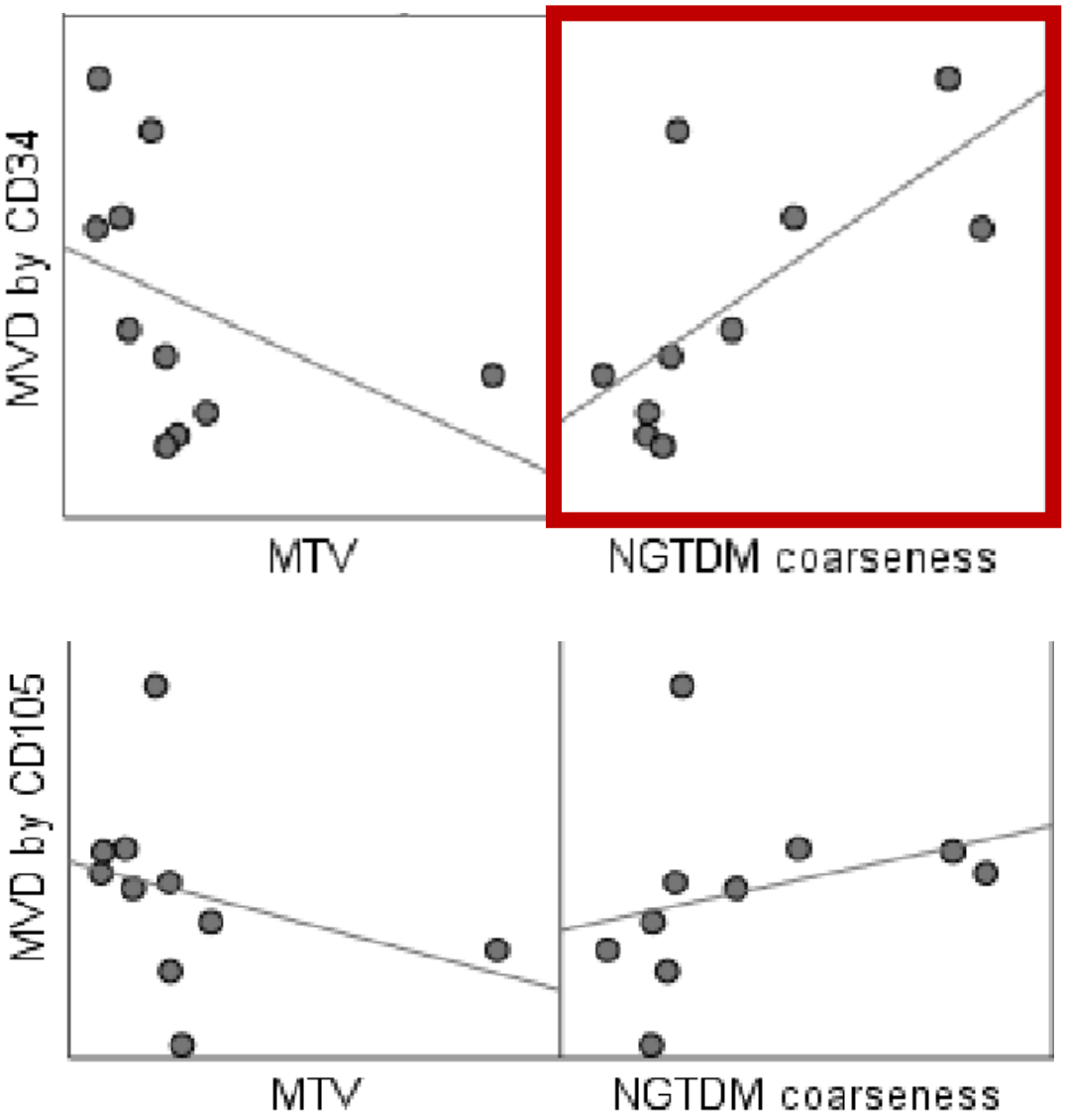

Figure 9. Correlation graph matrix of statistically significant ($p < 0.05$) standard and texture parameter versus histological parameters for 10 patients with ADC. Graphs in red border box demonstrate strongest correlation in the dataset ($r = 0.77$, p value < 0.01)

Table 11. Correlation coefficients for each standard and texture parameter versus histological parameters for 10 patients with ADC

Correlation Coefficient (r value)	GLUT-1 (%)	CD105 MVD	CD34 MVD	HIF-1-alpha	HEX-II	$Ki67_{avg}$	$Ki67_{max}$
SUV_{max}	-0.281	0.152	0.152	0.049	0.158	-0.030	-0.042
SUV_{mean}	-0.330	0.236	0.248	0.079	0.146	-0.042	-0.055
SUV_{peak}	-0.281	0.152	0.152	0.049	0.158	-0.030	-0.042
MTV	-0.012	-0.709	-0.758	0.000	-0.182	-0.176	0.055
TLG	0.024	-0.297	-0.418	0.219	0.097	0.103	0.248
First-order SD	-0.385	0.018	0.042	-0.012	0.006	-0.091	-0.055
First-order energy	-0.122	-0.127	-0.176	0.201	0.128	0.055	0.164
First-order skewness	-0.128	0.188	0.152	-0.164	-0.006	-0.394	-0.515
First-order kurtosis	-0.128	0.188	0.152	-0.164	-0.006	-0.394	-0.515
First-order entropy	-0.385	0.018	0.042	-0.012	0.006	-0.091	-0.055
GLCM contrast	-0.324	0.067	0.236	-0.097	-0.195	-0.103	-0.273
GLCM energy	-0.202	0.018	-0.055	-0.225	-0.116	-0.491	-0.515
GLCM homogeneity	-0.055	-0.345	-0.491	-0.097	-0.170	-0.321	-0.176
GLCM entropy	-0.037	0.018	0.212	-0.024	-0.055	0.212	0.152
NGTDM coarseness	0.049	0.745	0.770	0.000	0.231	0.188	-0.030
NGTDM contrast	-0.135	0.248	0.442	-0.006	-0.036	0.188	0.091

Legend for r value

r value	Colour code
> 0.7	
0.7 – 0.4	
< 0.4	

Table 12. Demonstrates p-values of the correlation test for 10 patients with ADC

p-value (significance 2-tailed)	GLUT-1 (%)	CD105 MVD	CD34 MVD	HIF-1-alpha	HEX-II	$Ki67_{avg}$	$Ki67_{max}$
SUV_{max}	0.431	0.676	0.676	0.894	0.663	0.934	0.907
SUV_{mean}	0.351	0.511	0.489	0.828	0.688	0.907	0.881
SUV_{peak}	0.431	0.676	0.676	0.894	0.663	0.934	0.907
MTV	0.973	0.022	0.011	1.000	0.614	0.627	0.881
TLG	0.947	0.405	0.229	0.544	0.789	0.777	0.489
First-order SD	0.271	0.960	0.907	0.973	0.987	0.803	0.881
First-order energy	0.736	0.726	0.627	0.578	0.725	0.881	0.651
First-order skewness	0.724	0.603	0.676	0.650	0.987	0.260	0.128
First-order kurtosis	0.724	0.603	0.676	0.650	0.987	0.260	0.128
First-order entropy	0.217	0.960	0.907	0.973	0.987	0.803	0.881
GLCM contrast	0.361	0.855	0.511	0.789	0.590	0.777	0.446
GLCM energy	0.576	0.960	0.881	0.532	0.751	0.150	0.128
GLCM homogeneity	0.880	0.328	0.150	0.789	0.638	0.365	0.627
GLCM entropy	0.920	0.960	0.556	0.947	0.881	0.556	0.676
NGTDM coarseness	0.893	0.013	0.009	1.000	0.521	0.603	0.934
NGTDM contrast	0.711	0.489	0.200	0.987	0.920	0.603	0.803

Legend for p-value

p-value	Colour code
< 0.050	
0.05 – 0.1	
> 0.1	

Table 13 demonstrates correlation coefficients (r value) for each standard and texture parameter versus histological parameters for the 8 SCC patients and table 14 demonstrates the p-values of the correlation test.

This data set demonstrated the maximum number of statistically significant correlations between standard and textural parameters versus histological parameters.
CD105 and CD34 MVD correlated strongly with first-order energy.
This dataset of 8 SCC patients is the only one in my study where the PET standard and textural parameters correlated strongly (p-value <0.05) with histological parameters HIF-1-alpha and HEX-II.
HIF-1-alpha correlated strongly with MTV, second-order GLCM energy, GLCM homogeneity and GLCM entropy and high-order NGTDM coarseness and NGTDM contrast.
HEX-II correlated strongly with MTV, second-order GLCM contrast and high-order NGTDM coarseness.

Although not statistically significant (p-value < 0.10 but > 0.05), there was some correlation between the following histological and textural parameters:

- Glut-1 correlated with second-order GLCM contrast and GLCM homogeneity; and high-order NGTDM contrast
- CD105 MVD correlated with SUV_{peak} and first-order entropy
- HEX-II correlated with TLG, first-order energy, second-order GLCM entropy and GLCM homogeneity; and high-order textural parameter (NGTDM contrast)
- $Ki67_{avg}$ correlated with first-order energy

The histological parameter $Ki67_{max}$ demonstrated no significant correlation with any standard or textural features.

Figure 10 demonstrates a correlation graph matrix of statistically significant ($p < 0.05$) standard and texture parameter versus histological parameters for 8 patients with SCC.

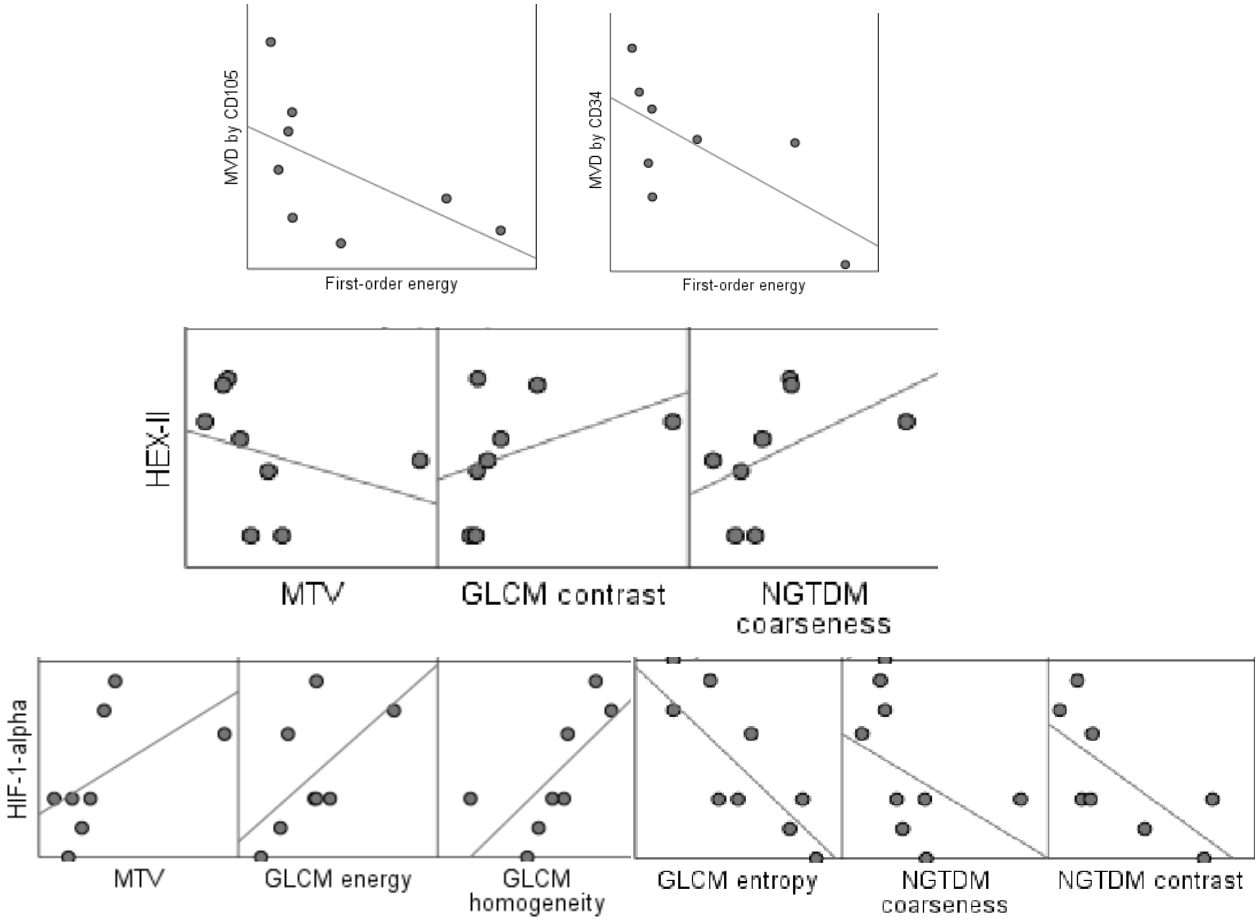

Figure 10. Correlation graph matrix of statistically significant ($p < 0.05$) standard and texture parameter versus histological parameters for 8 patients with SCC

Table 13. Correlation coefficients for each standard and texture parameter versus histological parameters for 8 patients with SCC

Correlation Coefficient (r value)	GLUT-1 (%)	CD105 MVD	CD34 MVD	HIF-1-alpha	HEX-II	$Ki67_{avg}$	$Ki67_{max}$
SUV_{max}	-0.126	-0.571	-0.190	0.366	-0.240	-0.167	-0.095
SUV_{mean}	-0.126	-0.571	-0.190	0.366	-0.240	-0.167	-0.095
SUV_{peak}	0.000	-0.667	-0.238	0.366	-0.347	-0.310	-0.238
MTV	0.504	-0.405	-0.548	0.732	-0.719	-0.333	-0.310
TLG	0.504	-0.619	-0.619	0.610	-0.683	-0.548	-0.524
First-order SD	0.000	-0.548	-0.143	0.146	-0.120	-0.310	-0.238
First-order energy	0.252	-0.786	-0.738	0.537	-0.623	-0.643	-0.595
First-order skewness	0.000	-0.190	-0.143	0.098	-0.036	-0.405	-0.286
First-order kurtosis	0.000	-0.286	-0.190	0.268	-0.084	-0.286	-0.143
First-order entropy	0.000	-0.667	-0.238	0.366	-0.347	-0.310	-0.238
GLCM contrast	-0.630	0.310	0.190	-0.586	0.731	0.357	0.286
GLCM energy	0.000	0.024	0.119	0.708	-0.287	0.310	0.405
GLCM homogeneity	0.630	-0.238	-0.381	0.830	-0.695	-0.286	-0.238
GLCM entropy	-0.504	0.238	0.262	-0.805	0.683	0.262	0.167
NGTDM coarseness	-0.504	0.405	0.548	-0.732	0.719	0.333	0.310
NGTDM contrast	-0.630	0.167	0.238	-0.732	0.659	0.310	0.238

Legend for r value

r value	Colour code
> 0.70	
0.70 – 0.62	
< 0.62	

Table 14. Demonstrates p-values of the correlation test for 8 patients with SCC

p-value (significance 2-tailed)	GLUT-1 (%)	CD105 MVD	CD34 MVD	HIF-1-alpha	HEX-II	$Ki67_{avg}$	$Ki67_{max}$
SUV_{max}	0.766	0.139	0.651	0.373	0.568	0.693	0.823
SUV_{mean}	0.766	0.139	0.651	0.373	0.568	0.693	0.823
SUV_{peak}	1.000	0.071	0.570	0.373	0.399	0.456	0.570
MTV	0.203	0.320	0.160	0.039	0.045	0.420	0.456
TLG	0.203	0.102	0.102	0.108	0.062	0.160	0.183
First-order SD	1.000	0.160	0.736	0.729	0.778	0.456	0.570
First-order energy	0.547	0.021	0.037	0.170	0.099	0.086	0.120
First-order skewness	1.000	0.651	0.736	0.818	0.933	0.320	0.493
First-order kurtosis	1.000	0.493	0.651	0.520	0.844	0.493	0.736
First-order entropy	1.000	0.071	0.570	0.373	0.399	0.456	0.570
GLCM contrast	0.094	0.456	0.651	0.127	0.040	0.385	0.493
GLCM energy	1.000	0.955	0.779	0.050	0.490	0.456	0.320
GLCM homogeneity	0.094	0.570	0.352	0.011	0.056	0.493	0.570
GLCM entropy	0.203	0.570	0.531	0.016	0.062	0.531	0.693
NGTDM coarseness	0.203	0.320	0.160	0.039	0.045	0.420	0.456
NGTDM contrast	0.094	0.693	0.570	0.039	0.076	0.456	0.570

Legend for p-value

p-value	Colour code
< 0.050	
0.05 – 0.1	
> 0.1	

In summary, we analysed the patients in 4 groups with key results as follows:

Group 1 (all 19 patients): CD105 MVD, staining neovessel endothelial cells, correlated negatively with TLG and first-order energy; and positively with NGTDM coarseness (r = -0.51, -0.47, 0.53, respectively: all $p<0.05$). CD34 MVD, staining vascular and lymphatic endothelial cells, correlated negatively with MTV and TLG; and positively with NGTDM coarseness (r = -0.59, -0.50, 0.62, respectively: all $p<0.05$). $Ki67_{avg}$ and $Ki67_{max}$ values correlated negatively with GLCM energy and first-order skewness, respectively (r = -0.47 and r = -0.48, respectively: all $p<0.05$).

Group 2 (18 patients with ADC and SCC): CD105 MVD correlated negatively with TLG, first-order energy and first-order entropy; and positively with NGTDM coarseness (r = -0.53, -0.52, -0.47, 0.53, respectively: all $p<0.05$). CD34 MVD correlated negatively with MTV and TLG; and positively with NGTDM coarseness (r = -0.61, -0.52, 0.64, respectively: all $p<0.05$).

Group 3 (10 ADC patients): CD105 MVD and CD34 MVD correlated with both MTV (r = -0.71, -0.76, respectively: all $p<0.05$) and NGTDM coarseness (r= 0.75, 0.77, respectively: all $p<0.05$).

Group 4 (8 SCC patients): CD105 MVD and CD34 MVD correlated negatively with first-order energy (r = -0.79, -0.74, respectively: all $p<0.05$).

HIF-1-alpha correlated strongly with MTV, second-order textural parameters (GLCM energy, GLCM homogeneity and GLCM entropy) and high-order textural parameters (NGTDM coarseness and NGTDM contrast) (r = 0.73, 0.71, 0.83, -0.81, -0.73, -0.73, respectively: all $p<0.05$).

HEX-II correlated strongly with MTV, second-order textural parameter (GLCM contrast) and high-order textural parameter (NGTDM coarseness) (r = -0.72, 0.73, 0.72, respectively: all $p<0.05$).

If the correction for multiple correlation testing was to be applied, the only statistically significant correlation was between CD34 MVD and high-order coarseness (p = 0.004), in Groups 1 and 2.

5.5 Discussion

In this study I investigated whether there were relationships between textural parameters of ^{18}F-FDG PET images and histological and IHC parameters of untreated NSCLC. This was to better understand the biological factors that may cause spatial heterogeneity of ^{18}F-FDG PET images and the possibility of us being able to predict the biological factors pre-operatively to influence management decisions.

Our prospective exploratory analysis, taking a p-value <0.05 as a significant result, has shown that TLG (inverse correlation) and NGTDM coarseness (positive correlation) correlate strongly with CD105 and CD34 MVD. CD105 MVD also strongly correlated with first-order energy (inverse correlation). $Ki67_{avg}$ strongly correlated with GLCM energy (inverse correlation), CD34 MVD with MTV (inverse correlation) and $Ki67_{max}$ with first-order skewness (inverse correlation).

The results (group 2) when the LCNC patient was excluded (n=1) showed similar strong correlation with CD105 MVD and CD34 MVD, except CD105 MVD also demonstrated strong correlation with first-order entropy (inverse correlation). Excluding the LCNC patient resulted in no significant correlation between PET and Ki67 IHC parameters.

The results from ADC subgroup of patients (n=10) have shown that MTV (inverse correlation) and NGTDM coarseness (positive correlation) correlate strongly with CD105 and CD34 MVD.

The SCC subgroup showed the maximum number of strong correlations: CD105 and CD34 MVD with first-order energy (inverse correlation); HEX-II with MTV (inverse correlation), GLCM contrast (positive correlation) and NGTDM coarseness (positive correlation); HIF-1-alpha demonstrated positive correlation with MTV, GLCM energy and GLCM homogeneity and inverse correlation with GLCM entropy, NGTDM coarseness and NGTDM contrast. Although histopathological and IHC parameters are the current gold standard for diagnosis and establishing tumour biology it is subject to sampling error at biopsy. Imaging, however, analyses the whole tumour and hence can potentially augment and complement histopathological and IHC measures.

There have been numerous studies that have shown the importance of understanding tumour biology and how they help in treatment decisions in NSCLC (171-174). For example, patients with advanced and metastatic NSCLC, who previously had barely any treatment options with poor prognosis, now have a better prognosis with immunotherapy targeting PD-1 and PD-L1 which are based on IHC measurements of PD-L1 expression (171).

Sasaki et al. in their study of 95 patients with surgically treated NSCLC found that survival was significantly longer for those with tumours expressing EGFR mutations than for those with wild-type gene expression (174). Low ERCC1 expression (key enzyme in nucleotide excision repair) correlates with increased sensitivity to platinum-based therapy and high ERCC1 expression correlates with better overall prognosis in NSCLC (175). The prognostic value of molecular markers such as EGFR mutation and ALK (anaplastic lymphoma kinase) rearrangement and benefit of TKIs in both early and advanced NSCLC, particularly ADC, have been published (176-179).

There are very limited data available in the literature correlating texture parameters with histological features in NSCLC. Recent studies have tried to demonstrate correlations

between histopathological and IHC features in NSCLC with textural features from ^{18}F-FDG PET imaging.

Bashir et al. in their recent study assessed correlations between ^{18}F-FDG PET-derived texture variables and whole-slide image (WSI)-derived metrics of tumour cellularity and spatial heterogeneity in twenty-two patients with NSCLC prospectively (79). They concluded that histopathological mean cell density and lacunarity (large gaps between cluster of cells) correlated with standard ^{18}F-FDG parameters, including SUV_{mean} and TLG, first-order statistical features, including kurtosis and skewness, and ^{18}F-FDG lacunarity, and thus may explain the biological basis of ^{18}F-FDG PET-uptake heterogeneity in NSCLC. In my study, similarly I found first-order skewness to have strong inverse correlation with $Ki67_{max}$ ($r = -0.47$, $p < 0.05$) and TLG to have strong inverse correlation with C105 and CD34 MVD ($r = -0.53$ and -0.52, respectively, $p < 0.05$).

Karacavus et al. in their study with a sub-group of 40 NSCLC patients (out of 83 total patients in the study) have shown correlations between a number of texture parameters (for example skewness, first-order entropy and first-order energy) and Ki67 IHC analysis of proliferation using k-nearest neighbours and SVM methods (80). TLG was the only standard metabolic parameter that correlated with Ki67 in their study. In my study Ki67 demonstrated an inverse correlation with GLCM energy and first-order skewness ($r = -0.47$ and $r = -0.48$, respectively: all $p<0.05$).

Castello et al. retrospectively analysed 44 patients with NSCLC before surgery (180). The tumour specimens were assessed for HIF-1-alpha, CD68-TAMs (tumour-associated macrophages), CD8-TILs (tumour-infiltrating lymphocytes), PD-1-TILs, and PD-L1 expressions and ^{18}F-FDG PET parameters, including SUV_{max}, SUV_{peak}, SUV_{mean}, MTV, and TLG and texture features including tumour sphericity, skewness, kurtosis, first-entropy, and first-energy.

They found that a significantly higher level of mean CD8-TILs was observed in tumours with higher entropy (P=0.041). In my study I found that in the SCC subgroup HIF-1-alpha demonstrated positive correlation with MTV, GLCM energy and GLCM homogeneity (r = 0.73, 0.71, 0.83, respectively: $p<0.05$) and inverse correlation with GLCM entropy, NGTDM coarseness and NGTDM contrast (-0.81, -0.73, -0.73, respectively: $p<0.05$).

Although this was not a textural analysis study, Vessele et al. concluded that standard SUV parameters from ^{18}F-FDG PET images correlated strongly with Ki-67 expression ($p < 0.0001$) (148).

Several ex-vivo studies have correlated ^{18}F-FDG uptake with cellularity, fibrosis, and hypoxia (28, 73, 181). Zhao et al. in their rat hepatoma model showed autoradiography of ex vivo tumour samples demonstrated ^{18}F-FDG uptake in the central regions of the tumours and that those regions were also the only regions that stained positively for HIF-1-alpha (73).

Van Baardwijk et al. studied five patients with NSCLC and found differences in zonal distribution of fibrosis and cellularity on histologic sampling of each region: Fibrosis predominated in low-activity tumour regions, whereas regions with high ^{18}F-FDG uptake showed greater cellularity (181).

The findings in my study add to the evidence in the literature. In my study SUV_{max}, $SUV_{mean,}$ and SUV_{peak}, although showed some correlation with CD105 MVD and GLUT-1 (%), these were not statistically significant.

Tumour heterogeneity is closely linked to blood supply and hypoxia (182, 183). A heterogenous tumour's blood supply is associated with hypoxic areas which in turn leads to genetic instability (182). HIF-1-alpha controls angiogenesis and glycolysis; tumour growth is also correlated with HIF-1-alpha expression. The hypoxic changes in tissues leads to resistance to treatment due to increased tumour aggression (183). I measured tumour

vascularity and hypoxia with MVD and HIF-1-alpha. This possibly explains why there was a positive correlation between HIF-1-alpha and MTV and inverse correlation between MVD and MTV across my data set, i.e. larger the metabolic tumour the less vasculature and increased areas of hypoxia.

The textural features that commonly have been found to correlate to histological parameters, survival, prognosis and staging in various studies in the literature were also found to have statistically significant correlations in my study. Although when corrected for multiple correlations the p-value for my data set is <0.006, I would like to argue that these are exploratory findings. The correlation data with p-values between 0.05 – 0.006 would give relevant information on potentially useful markers going forwards in larger confirmatory studies.

I have been cautious in interpreting my results for the ADC and SCC subset of patients in groups 3 and 4. I am aware that given the small number of patients in this data set (n = 10 and n = 8, respectively) the probability of false positive correlations with multiple testing is high. However, my analyses have demonstrated differences between ADC and SCC in line with similar studies in the literature; there are very limited data in the literature correlating PET texture parameters to IHC in different histological subtypes of NSCLC.

Ha et al. (184) in their study found that the 14 out of 15 FDG PET texture parameters that had significantly different values between ADC (n = 17) and SCC (n = 13) were co-occurrence matrix-based texture parameters. Similar results were found in my study with HIF-1-alpha correlating strongly with second-order textural parameters (GLCM energy, GLCM homogeneity and GLCM entropy) in SCC but not ADC.

Bianconi et al. (52), in their recent study concluded that SCC had stronger PET variability and lower uniformity in contrast to ADC which exhibited lower variability and higher uniformity.

Karetsi e al. (185) in their study, concluded that HIF-1-alpha differs significantly between subtypes of lung cancer, with the frequency of HIF-1-alpha nuclear expression 88.2% in SCC and 62.5% in ADC. This is similar to my study findings where HIF-1-alpha correlated strongly with MTV, second-order textural parameters (GLCM energy, GLCM homogeneity and GLCM in SCC patients but no significant correlation was found in ADC.

The limitations of my study are the number of patients recruited is small (n = 19) which may lead to lower statistical power. This is an exploratory study and the consistent relationship with the 2 different MVD measurements and the PET standard and texture parameters in all 4 groups of analysis suggests this is a real association. The other limitation of my study is that I have not corrected for multiple testing upfront. As this was an exploratory study, I wanted to analyse correlations between all textural and IHC parameters. Although the p-value after correction for multiple correlation testing is 0.006 for significance, I retained all significant results with p-value > 0.05 as my sample size is small and applying correction for multiple correlation may falsely lead to a type 2 error. I did not want to reject potentially true correlations between texture features and IHC as these features are of potential interest and need to be confirmed in larger series when corrections for multiple testing could be applied upfront.

5.6 Conclusion

Several standard and textural parameters extracted from ^{18}F-FDG images correlate with MVD, Ki67, HIF-1-apha and HEX-II histological parameters. This needs to be confirmed in larger series, but standard and texture parameters extracted from ^{18}F-FDG images potentially provide additional useful data that could report on the tumour phenotype more accurately. My study has also uncovered interesting differences in PET texture correlations with histological subtypes in NSCLC; with only limited data in the current literature, my study would add value to it.

CHAPTER 6

6.1 Discussion

The aim of my thesis was to determine if texture features derived from ^{18}F-FDG PET/CT were associated with survival and IHC parameters. In the following paragraph I will summarise my experiment chapters and future direction of my research.

The aim of my first experiment (chapter 4) was to retrospectively determine if texture features derived from ^{18}F-FDG PET/CT images of MPM were associated with overall survival. I did establish in my study that texture feature first-order entropy was an independent indicator in predicting survival in MPM patients and this parameter reflecting heterogeneity of ^{18}F-FDG distribution has been shown to be a predictive and prognostic marker in other tumours. There are no similar studies in the literature with MPM patients as per my knowledge. When compared to other published literature correlating standard PET parameters such as SUVs, I found that first-order entropy was a better indicator of overall survival in MPM. However, my study was a retrospective study, and this should be validated with a prospective design in the future, with more patients recruited, ideally from more than one institution. I was not able to analyse my data between each different histological subtype and this would be an interesting area to study further given the heterogeneity of MPM tumours.

The aim of my second experiment (chapter 5) was to prospectively measure texture parameters of ^{18}F-FDG PET/CT images of untreated NSCLC and to correlate these finding with IHC parameters in order to obtain a better understanding of the biological factors that may be related to spatial heterogeneity of ^{18}F-FDG PET images. I did establish correlations

between various standard, first-order, second-order and high-order ^{18}F-FDG texture features and histological (MVD, Ki67, HIF-1-alpha and HEX-II) parameters, in line with other similar studies in the literature. Of interest, these seem to differ in the main mechanisms associated with ^{18}F-FDG distribution. There are limited data in the literature comparing texture features to histology in NSCLC. I believe my study adds to the currently available data, although exploratory. Correction for multiple testing, reduces the number of statistically significant correlations.

6.2 Conclusion

I have established that texture features derived from tumours can predict overall survival in MPM and also correlate with immunohistochemical features in NSCLC. It thus suggests that FDG PET imaging has the potential to offer more information than what is currently used in clinical practice.

Reference List

(1) Ferlay, J., Soerjomataram, I., Dikshit, R., Eser, S., Mathers, C., Rebelo, M., Parkin, D.M., Forman, D., and Bray, F. (2015). Cancer incidence and mortality worldwide: Sources, methods and major patterns in GLOBOCAN 2012. *International Journal of Cancer* **136**(5), E359-E386.

(2) Bray, F., Ferlay, J., Soerjomataram, I., Siegel, R.L., Torre, L.A., and Jemal, A. (2018). Global cancer statistics 2018: GLOBOCAN estimates of incidence and mortality worldwide for 36 cancers in 185 countries. *CA Cancer. J. Clin.* **68**(6), 394-424.

(3) The Royal College Of Radiologists, Royal College Of Physicians Of London, Royal College Of Physicians And Surgeons Of Glasgow, Royal College Of Physicians Of Edinburgh, British Nuclear Medicine Society, and Administration Of Radioactive Substances Advisory Committee. (2016). Evidence-based indications for the use of PET-CT in the United Kingdom 2016. *Clin. Radiol.* **71**(7), 171.

(4) Cotran, R.S., Kumar, V., and Robbins, S.L. (2005). *Robbins and Cotran pathologic basis of disease ,* 7. ed. edn (Philadelphia, Pa. [u.a.]: Elsevier Saunders).

(5) Smith, T.A. (1998). FDG uptake, tumour characteristics and response to therapy: a review. *Nucl. Med. Commun.* **19**(2), 97-105.

(6) Kapoor, V., McCook, B.M., and Torok, F.S. (2004). An introduction to PET-CT imaging. *Radiographics* **24**(2), 523-543.

(7) Chicklore, S., Goh, V., Siddique, M., Roy, A., Marsden, P.K., and Cook, G.J. (2013). Quantifying tumour heterogeneity in 18F-FDG PET/CT imaging by texture analysis. *Eur. J. Nucl. Med. Mol. Imaging* **40**(1), 133-140.

(8) Lambin, P., Rios-Velazquez, E., Leijenaar, R., Carvalho, S., van Stiphout, Ruud G. P. M., Granton, P., Zegers, C.M.L., Gillies, R., Boellard, R., Dekker, A., and Aerts, Hugo J. W. L. (2012). Radiomics: Extracting more information from medical images using advanced feature analysis. *Eur. J. Cancer* **48**(4), 441-446.

(9) Hillner, B.E., Siegel, B.A., Liu, D., Shields, A.F., Gareen, I.F., Hanna, L., Stine, S.H., and Coleman, R.E. (2008). Impact of Positron Emission Tomography/Computed Tomography and Positron Emission Tomography (PET) Alone on Expected Management of Patients With Cancer: Initial Results From the National Oncologic PET Registry. *Journal of Clinical Oncology* **26**(13), 2155-2161.

(10) Juweid, M.E., and Cheson, B.D. (2006). Positron-Emission Tomography and Assessment of Cancer Therapy. *N. Engl. J. Med.* **354**(5), 496-507.

(11) Ben-Haim, S., and Ell, P. (2008). 18F-FDG PET and PET/CT in the Evaluation of Cancer Treatment Response. *Journal of Nuclear Medicine* **50**(1), 88-99.

(12) Wahl, R.L., Jacene, H., Kasamon, Y., and Lodge, M.A. (2009). From RECIST to PERCIST: Evolving Considerations for PET Response Criteria in Solid Tumors. *Journal of Nuclear Medicine* **50**122S-150S.

(13) Cremerius, U., Effert, P.J., Adam, G., Sabri, O., Zimmy, M., Wagenknecht, G., Jakse, G., and Buell, U. (1998). FDG PET for detection and therapy control of metastatic germ cell tumor. *J. Nucl. Med.* **39**(5), 815-822.

(14) Dehdashti, F., Mortimer, J.E., Trinkaus, K., Naughton, M.J., Ellis, M., Katzenellenbogen, J.A., Welch, M.J., and Siegel, B.A. (2008). PET-based estradiol challenge as a predictive biomarker of response to endocrine therapy in women with estrogen-receptor-positive breast cancer. *Breast Cancer Res. Treat.* **113**(3), 509-517.

(15) Mac Manus, M.P., Ding, Z., Hogg, A., Herschtal, A., Binns, D., Ball, D.L., and Hicks, R.J. (2011). Association Between Pulmonary Uptake of Fluorodeoxyglucose Detected by Positron Emission Tomography Scanning After Radiation Therapy for Non–Small-Cell Lung Cancer and Radiation Pneumonitis. *International Journal of Radiation Oncology*Biology*Physics* **80**(5), 1365-1371.

(16) de Geus-Oei, L.-., van, d.H., Visser, E.P., Hermsen, R., van Hoorn, B.A., Timmer-Bonte, J., Willemsen, A.T., Pruim, J., Corstens, F.H.M., Krabbe, P.F.M., and Oyen, W.J.G. (2007). Chemotherapy Response Evaluation with 18F-FDG PET in Patients with Non-Small Cell Lung Cancer. *Journal of Nuclear Medicine* **48**(10), 1592-1598.

(17) Rizk, N.P., Tang, L., Adusumilli, P.S., Bains, M.S., Akhurst, T.J., Ilson, D., Goodman, K., and Rusch, V.W. (2009). Predictive Value of Initial PET-SUVmax in Patients with Locally Advanced Esophageal and Gastroesophageal Junction Adenocarcinoma. *Journal of Thoracic Oncology* **4**(7), 875-879.

(18) Ohno, Y., Koyama, H., Yoshikawa, T., Matsumoto, K., Aoyama, N., Onishi, Y., and Sugimura, K. (2012). Diffusion-Weighted MRI Versus 18F-FDG PET/CT: Performance as Predictors of Tumor Treatment Response and Patient Survival in Patients With Non–Small Cell Lung Cancer Receiving Chemoradiotherapy. *Am. J. Roentgenol.* **198**(1), 75-82.

(19) Zhang, H., Yu, J., Meng, X., Yue, J., Feng, R., and Ma, L. (2011). Prognostic value of serial 18F]fluorodeoxyglucose PET-CT uptake in stage III patients with non-small cell lung cancer treated by concurrent chemoradiotherapy. *Eur. J. Radiol.* **77**(1), 92-96.

(20) Borst, G.R., Belderbos, J.S.A., Boellaard, R., Comans, E.F.I., Jaeger, K.D., Lammertsma, A.A., and Lebesque, J.V. (2005). Standardised FDG uptake: A prognostic factor for inoperable non-small cell lung cancer. *Eur. J. Cancer* **41**(11), 1533-1541.

(21) Lee, K.-. (2006). High Fluorodeoxyglucose Uptake on Positron Emission Tomography in Patients with Advanced Non-Small Cell Lung Cancer on Platinum-Based Combination Chemotherapy. *Clinical Cancer Research* **12**(14), 4232-4236.

(22) Cazaentre, T., Morschhauser, F., Vermandel, M., Betrouni, N., Prangère, T., Steinling, M., and Huglo, D. (2009). Pre-therapy 18F-FDG PET quantitative parameters help in

predicting the response to radioimmunotherapy in non-Hodgkin lymphoma. *European Journal of Nuclear Medicine and Molecular Imaging* **37**(3), 494-504.

(23) Colavolpe, C., Metellus, P., Mancini, J., Barrie, M., Béquet-Boucard, C., Figarella-Branger, D., Mundler, O., Chinot, O., and Guedj, E. (2011). Independent prognostic value of pre-treatment 18-FDG-PET in high-grade gliomas. *J. Neurooncol.* **107**(3), 527-535.

(24) Xie, P., Li, M., Zhao, H., Sun, X., Fu, Z., and Yu, J. (2011). 18F-FDG PET or PET-CT to evaluate prognosis for head and neck cancer: a meta-analysis. *J. Cancer Res. Clin. Oncol.* **137**(7), 1085-1093.

(25) Kitagawa, Y., Sano, K., Nishizawa, S., Nakamura, M., Ogasawara, T., Sadato, N., and Yonekura, Y. (2003). FDG-PET for prediction of tumour aggressiveness and response to intra-arterial chemotherapy and radiotherapy in head and neck cancer. *European Journal of Nuclear Medicine and Molecular Imaging* **30**(1), 63-71.

(26) Kidd, E.A., Dehdashti, F., Siegel, B.A., and Grigsby, P.W. (2010). Anal cancer maximum F-18 fluorodeoxyglucose uptake on positron emission tomography is correlated with prognosis. *Radiotherapy and Oncology* **95**(3), 288-291.

(27) Zhu, W., Xing, L., Yue, J., Sun, X., Sun, X., Zhao, H., and Yu, J. (2012). Prognostic significance of SUV on PET/CT in patients with localised oesophagogastric junction cancer receiving neoadjuvant chemotherapy/chemoradiation: a systematic review and meta-analysis. *Br. J. Radiol.* **85**(1017), e694-e701.

(28) Henriksson, E., Kjellen, E., Wahlberg, P., Ohlsson, T., Wennerberg, J., and Brun, E. (2007). 2-Deoxy-2-[18F] fluoro-D-glucose uptake and correlation to intratumoral heterogeneity. *Anticancer Res.* **27**(4B), 2155-2159.

(29) van Velden, Floris H. P., Cheebsumon, P., Yaqub, M., Smit, E.F., Hoekstra, O.S., Lammertsma, A.A., and Boellaard, R. (2011). Evaluation of a cumulative SUV-volume histogram method for parameterizing heterogeneous intratumoural FDG uptake in non-small cell lung cancer PET studies. *European Journal of Nuclear Medicine and Molecular Imaging* **38**(9), 1636-1647.

(30) Yu, H., Caldwell, C., Mah, K., Poon, I., Balogh, J., MacKenzie, R., Khaouam, N., and Tirona, R. (2009). Automated Radiation Targeting in Head-and-Neck Cancer Using Region-Based Texture Analysis of PET and CT Images. *International Journal of Radiation Oncology*Biology*Physics* **75**(2), 618-625.

(31) Yu, H., Caldwell, C., Mah, K., and Mozeg, D. (2009). Coregistered FDG PET/CT-Based Textural Characterization of Head and Neck Cancer for Radiation Treatment Planning. *IEEE Trans. Med. Imaging* **28**(3), 374-383.

(32) Eary, J.F., O'Sullivan, F., O'Sullivan, J., and Conrad, E.U. (2008). Spatial Heterogeneity in Sarcoma 18F-FDG Uptake as a Predictor of Patient Outcome. *Journal of Nuclear Medicine* **49**(12), 1973-1979.

(33) Tixier, F., Le Rest, C.C., Hatt, M., Albarghach, N., Pradier, O., Metges, J.-., Corcos, L., and Visvikis, D. (2011). Intratumor Heterogeneity Characterized by Textural Features on Baseline 18F-FDG PET Images Predicts Response to Concomitant Radiochemotherapy in Esophageal Cancer. *Journal of Nuclear Medicine* **52**(3), 369-378.

(34) El Naqa, I., Grigsby, P.W., Apte, A., Kidd, E., Donnelly, E., Khullar, D., Chaudhari, S., Yang, D., Schmitt, M., Laforest, R.*, et al.* (2009). Exploring feature-based approaches in PET images for predicting cancer treatment outcomes. *Pattern Recognit* **42**(6), 1162-1171.

(35) Vaidya, M., Creach, K.M., Frye, J., Dehdashti, F., Bradley, J.D., and El Naqa, I. (2012). Combined PET/CT image characteristics for radiotherapy tumor response in lung cancer. *Radiotherapy and Oncology* **102**(2), 239-245.

(36) Castellano, G., Bonilha, L., Li, L.M., and Cendes, F. (2004). Texture analysis of medical images. *Clin. Radiol.* **59**(12), 1061-1069.

(37) Al-Kadi, O., and Watson, D. (2008). Texture Analysis of Aggressive and Nonaggressive Lung Tumor CE CT Images. *IEEE Transactions on Biomedical Engineering* **55**(7), 1822-1830.

(38) Ganeshan, B., Miles, K.A., Young, R.C.D., and Chatwin, C.R. (2007). Hepatic entropy and uniformity: additional parameters that can potentially increase the effectiveness of contrast enhancement during abdominal CT. *Clin. Radiol.* **62**(8), 761-768.

(39) Brown, R.A., and Frayne, R. (2008). A comparison of texture quantification techniques based on the Fourier and S transforms. *Med. Phys.* **35**(11), 4998-5008.

(40) Goh, V., Sanghera, B., Wellsted, D.M., Sundin, J., and Halligan, S. (2009). Assessment of the spatial pattern of colorectal tumour perfusion estimated at perfusion CT using two-dimensional fractal analysis. *Eur. Radiol.* **19**(6), 1358-1365.

(41) Sanghera, B., Banerjee, D., Khan, A., Simcock, I., Stirling, J.J., Glynne-Jones, R., and Goh, V. (2012). Reproducibility of 2D and 3D Fractal Analysis Techniques for the Assessment of Spatial Heterogeneity of Regional Blood Flow in Rectal Cancer. *Radiology* **263**(3), 865-873.

(42) Craciunescu, O.I., Das, S.K., and Clegg, S.T. (1999). Dynamic Contrast-Enhanced MRI and Fractal Characteristics of Percolation Clusters in Two-Dimensional Tumor Blood Perfusion. *J. Biomech. Eng.* **121**(5), 480.

(43) Dettori, L., and Semler, L. (2007). A comparison of wavelet, ridgelet, and curvelet-based texture classification algorithms in computed tomography. *Comput. Biol. Med.* **37**(4), 486-498.

(44) Al-Kadi, O. (2010). Assessment of texture measures susceptibility to noise in conventional and contrast enhanced computed tomography lung tumour images. *Comput. Med. Imaging Graphics* **34**(6), 494-503.

(45) Amadasun, M., and King, R. (1989). Textural features corresponding to textural properties. *IEEE Trans. Syst. Man Cybern.* **19**(5), 1264-1274.

(46) Veenland, J.F., Grashuis, J.L., and Gelsema, E.S. (1998). Texture analysis in radiographs: The influence of modulation transfer function and noise on the discriminative ability of texture features. *Med. Phys.* **25**(6), 922-936.

(47) Galavis, P.E., Hollensen, C., Jallow, N., Paliwal, B., and Jeraj, R. (2010). Variability of textural features in FDG PET images due to different acquisition modes and reconstruction parameters. *Acta Oncol.* **49**(7), 1012-1016.

(48) Tixier, F., Hatt, M., Le Rest, C.C., Le Pogam, A., Corcos, L., and Visvikis, D. (2012). Reproducibility of Tumor Uptake Heterogeneity Characterization Through Textural Feature Analysis in 18F-FDG PET. *Journal of Nuclear Medicine* **53**(5), 693-700.

(49) Lodge, M.A., Lucas, J.D., Marsden, P.K., Cronin, B.F., O'Doherty, M.J., and Smith, M.A. (1999). A PET study of 18 FDG uptake in soft tissue masses. *European Journal of Nuclear Medicine and Molecular Imaging* **26**(1), 22-30.

(50) Lovat, E., Siddique, M., Goh, V., Ferner, R.E., Cook, G.J.R., and Warbey, V.S. (2017). The effect of post-injection 18F-FDG PET scanning time on texture analysis of peripheral nerve sheath tumours in neurofibromatosis-1. *EJNMMI Research* **7**(1), 35.

(51) Feliciani, G., Fioroni, F., Grassi, E., Bertolini, M., Rosca, A., Timon, G., Galaverni, M., Iotti, C., Versari, A., Iori, M., and Ciammella, P. (2018). Radiomic Profiling of Head and Neck Cancer: ^{18}F-FDG PET Texture Analysis as Predictor of Patient Survival. *Contrast Media & Molecular Imaging* **2018**3574310.

(52) Bianconi, F., Palumbo, I., Fravolini, M.L., Chiari, R., Minestrini, M., Brunese, L., and Palumbo, B. (2019). Texture Analysis on [(18)F]FDG PET/CT in Non-Small-Cell Lung Cancer: Correlations Between PET Features, CT Features, and Histological Types. *Molecular Imaging and Biology* **21**(6), 1200-1209.

(53) Wu, W., Li, Z., Dong, S., Liu, S., Zheng, L., Huang, M., and Zhang, J. (2019). Texture analysis of pretreatment [18F]FDG PET/CT for the prognostic prediction of locally advanced salivary gland carcinoma treated with interstitial brachytherapy. *EJNMMI Research* **9**(1), 89.

(54) Wang, Z., Guerriero, A., and De Sario, M. (1996). Comparison of several approaches for the segmentation of texture images. *Pattern Recog. Lett.* **17**(5), 509-521.

(55) Sharma, N., Ray, A., Sharma, S., Shukla, K.K., Pradhan, S., and Aggarwal, L. (2008). Segmentation and classification of medical images using texture-primitive features: Application of BAM-type artificial neural network. *Journal of Medical Physics* **33**(3), 119.

(56) Wang, H., Zhou, Z., Li, Y., Chen, Z., Lu, P., Wang, W., Liu, W., and Yu, L. (2017). Comparison of machine learning methods for classifying mediastinal lymph node metastasis of non-small cell lung cancer from (18)F-FDG PET/CT images. *EJNMMI Research* **7**(1), 11.

(57) Carvalho, S., Leijenaar, R.T.H., Troost, E.G.C., van Timmeren, J.,E., Oberije, C., van Elmpt, W., de Geus-Oei, L., Bussink, J., and Lambin, P. (2018). 18F-fluorodeoxyglucose positron-emission tomography (FDG-PET)-Radiomics of metastatic lymph nodes and primary tumor in

non-small cell lung cancer (NSCLC) - A prospective externally validated study. *PloS One* **13**(3), e0192859.

(58) Jansen, R.W., van Amstel, P., Martens, R.M., Kooi, I.E., Wesseling, P., de Langen, A.,J., Menke-Van der Houven van Oordt, Catharina,W., Jansen, B.H.E., Moll, A.C., Dorsman, J.C.*, et al.* (2018). Non-invasive tumor genotyping using radiogenomic biomarkers, a systematic review and oncology-wide pathway analysis. *Oncotarget* **9**(28), 20134-20155.

(59) Elstrom, R.L., Bauer, D.E., Buzzai, M., Karnauskas, R., Harris, M.H., Plas, D.R., Zhuang, H., Cinalli, R.M., Alavi, A., Rudin, C.M., and Thompson, C.B. (2004). Akt stimulates aerobic glycolysis in cancer cells. *Cancer Res.* **64**(11), 3892-3899.

(60) Lv, Z., Fan, J., Xu, J., Wu, F., Huang, Q., Guo, M., Liao, T., Liu, S., Lan, X., Liao, S.*, et al.* (2018). Value of (18)F-FDG PET/CT for predicting EGFR mutations and positive ALK expression in patients with non-small cell lung cancer: a retrospective analysis of 849 Chinese patients. *European Journal of Nuclear Medicine and Molecular Imaging* **45**(5), 735-750.

(61) Minamimoto, R., Jamali, M., Gevaert, O., Echegaray, S., Khuong, A., Hoang, C.D., Shrager, J.B., Plevritis, S.K., Rubin, D.L., Leung, A.N.*, et al.* (2017). Prediction of EGFR and KRAS mutation in non-small cell lung cancer using quantitative (18)F FDG-PET/CT metrics. *Oncotarget* **8**(32), 52792-52801.

(62) Yip, S.S.F., Kim, J., Coroller, T.P., Parmar, C., Velazquez, E.R., Huynh, E., Mak, R.H., and Aerts, Hugo J. W. L. (2017). Associations Between Somatic Mutations and Metabolic Imaging Phenotypes in Non-Small Cell Lung Cancer. *Journal of Nuclear Medicine : Official Publication, Society of Nuclear Medicine* **58**(4), 569-576.

(63) Cook, G.J.R., O'Brien, M.,E., Siddique, M., Chicklore, S., Loi, H.Y., Sharma, B., Punwani, R., Bassett, P., Goh, V., and Chua, S. (2015). Non-Small Cell Lung Cancer Treated with Erlotinib: Heterogeneity of (18)F-FDG Uptake at PET-Association with Treatment Response and Prognosis. *Radiology* **276**(3), 883-893.

(64) Park, S., Ha, S., Lee, S., Paeng, J.C., Keam, B., Kim, T.M., Kim, D., and Heo, D.S. (2018). Intratumoral heterogeneity characterized by pretreatment PET in non-small cell lung cancer patients predicts progression-free survival on EGFR tyrosine kinase inhibitor. *PloS One* **13**(1), e0189766.

(65) Moon, S.H., Kim, J., Joung, J., Cha, H., Park, W., Ahn, J.S., Ahn, M., Park, K., Choi, J.Y., Lee, K.*, et al.* (2019). Correlations between metabolic texture features, genetic heterogeneity, and mutation burden in patients with lung cancer. *European Journal of Nuclear Medicine and Molecular Imaging* **46**(2), 446-454.

(66) Nair, V.S., Gevaert, O., Davidzon, G., Napel, S., Graves, E.E., Hoang, C.D., Shrager, J.B., Quon, A., Rubin, D.L., and Plevritis, S.K. (2012). Prognostic PET 18F-FDG uptake imaging features are associated with major oncogenomic alterations in patients with resected non-small cell lung cancer. *Cancer Res.* **72**(15), 3725-3734.

(67) Nair, V.S., Gevaert, O., Davidzon, G., Plevritis, S.K., and West, R. (2014). NF-κB protein expression associates with (18)F-FDG PET tumor uptake in non-small cell lung cancer: a radiogenomics validation study to understand tumor metabolism. *Lung Cancer* **83**(2), 189-196.

(68) Sollini, M., Cozzi, L., Antunovic, L., Chiti, A., and Kirienko, M. (2017). PET Radiomics in NSCLC: state of the art and a proposal for harmonization of methodology. *Scientific Reports* **7**(1), 358.

(69) Bashir, U., Siddique, M.M., Mclean, E., Goh, V., and Cook, G.J. (2016). Imaging Heterogeneity in Lung Cancer: Techniques, Applications, and Challenges. *AJR.American Journal of Roentgenology* **207**(3), 534-543.

(70) Ohri, N., Duan, F., Snyder, B.S., Wei, B., Machtay, M., Alavi, A., Siegel, B.A., Johnson, D.W., Bradley, J.D., DeNittis, A.*, et al.* (2016). Pretreatment 18F-FDG PET Textural Features in Locally Advanced Non-Small Cell Lung Cancer: Secondary Analysis of ACRIN 6668/RTOG 0235. *Journal of Nuclear Medicine : Official Publication, Society of Nuclear Medicine* **57**(6), 842-848.

(71) Arshad, M.A., Thornton, A., Lu, H., Tam, H., Wallitt, K., Rodgers, N., Scarsbrook, A., McDermott, G., Cook, G.J., Landau, D.*, et al.* (2019). Discovery of pre-therapy 2-deoxy-2-(18)F-fluoro-D-glucose positron emission tomography-based radiomics classifiers of survival outcome in non-small-cell lung cancer patients. *European Journal of Nuclear Medicine and Molecular Imaging* **46**(2), 455-466.

(72) von Forstner, C., Egberts, J., Ammerpohl, O., Niedzielska, D., Buchert, R., Mikecz, P., Schumacher, U., Peldschus, K., Adam, G., Pilarsky, C.*, et al.* (2008). Gene expression patterns and tumor uptake of 18F-FDG, 18F-FLT, and 18F-FEC in PET/MRI of an orthotopic mouse xenotransplantation model of pancreatic cancer. *Journal of Nuclear Medicine : Official Publication, Society of Nuclear Medicine* **49**(8), 1362-1370.

(73) Zhao, S., Kuge, Y., Mochizuki, T., Takahashi, T., Nakada, K., Sato, M., Takei, T., and Tamaki, N. (2005). Biologic correlates of intratumoral heterogeneity in 18F-FDG distribution with regional expression of glucose transporters and hexokinase-II in experimental tumor. *Journal of Nuclear Medicine : Official Publication, Society of Nuclear Medicine* **46**(4), 675-682.

(74) Orlhac, F., Thézé, B., Soussan, M., Boisgard, R., and Buvat, I. (2016). Multiscale Texture Analysis: From 18F-FDG PET Images to Histologic Images. *Journal of Nuclear Medicine : Official Publication, Society of Nuclear Medicine* **57**(11), 1823-1828.

(75) Ganeshan, B., Goh, V., Mandeville, H.C., Ng, Q.S., Hoskin, P.J., and Miles, K.A. (2013). Non–Small Cell Lung Cancer: Histopathologic Correlates for Texture Parameters at CT. *Radiology* **266**(1), 326-336.

(76) Goh, V., Ganeshan, B., Nathan, P., Juttla, J.K., Vinayan, A., and Miles, K.A. (2011). Assessment of Response to Tyrosine Kinase Inhibitors in Metastatic Renal Cell Cancer: CT Texture as a Predictive Biomarker. *Radiology* **261**(1), 165-171.

(77) Ganeshan, B., Skogen, K., Pressney, I., Coutroubis, D., and Miles, K. (2012). Tumour heterogeneity in oesophageal cancer assessed by CT texture analysis: Preliminary evidence of an association with tumour metabolism, stage, and survival. *Clin. Radiol.* **67**(2), 157-164.

(78) Ganeshan, B., Panayiotou, E., Burnand, K., Dizdarevic, S., and Miles, K. (2011). Tumour heterogeneity in non-small cell lung carcinoma assessed by CT texture analysis: a potential marker of survival. *Eur. Radiol.* **22**(4), 796-802.

(79) Bashir, U., Foot, O., Wise, O., Siddique, M.M., Mclean, E., Bille, A., Goh, V., and Cook, G.J. (2018). Investigating the histopathologic correlates of 18F-FDG PET heterogeneity in non-small-cell lung cancer. *Nucl. Med. Commun.* **39**(12), 1197-1206.

(80) Karacavus, S., Yılmaz, B., Tasdemir, A., Kayaaltı, Ö, Kaya, E., İçer, S., and Ayyıldız, O. (2018). Can Laws Be a Potential PET Image Texture Analysis Approach for Evaluation of Tumor Heterogeneity and Histopathological Characteristics in NSCLC? *J. Digital Imaging* **31**(2), 210-223.

(81) Ma, Y., Feng, W., Wu, Z., Liu, M., Zhang, F., Liang, Z., Cui, C., Huang, J., Li, X., and Guo, X. (2018). Intra-tumoural heterogeneity characterization through texture and colour analysis for differentiation of non-small cell lung carcinoma subtypes. *Phys. Med. Biol.* **63**(16), 165018.

(82) Shukuya, T., and Carbone, D.P. (2016). Predictive Markers for the Efficacy of Anti–PD-1/PD-L1 Antibodies in Lung Cancer. *Journal of Thoracic Oncology* **11**(7), 976-988.

(83) Ilie, M., Long-Mira, E., Bence, C., Butori, C., Lassalle, S., Bouhlel, L., Fazzalari, L., Zahaf, K., Lalvée, S., Washetine, K.*, et al.* (2016). Comparative study of the PD-L1 status between surgically resected specimens and matched biopsies of NSCLC patients reveal major discordances: a potential issue for anti-PD-L1 therapeutic strategies. *Annals of Oncology : Official Journal of the European Society for Medical Oncology* **27**(1), 147-153.

(84) Niemeijer, A.N., Leung, D., Huisman, M.C., Bahce, I., Hoekstra, O.S., Dongen, G. A. M. S, Boellaard, R., Du, S., Hayes, W., Smith, R.*, et al.* (2018). Whole body PD-1 and PD-L1 positron emission tomography in patients with non-small-cell lung cancer. *Nature Communications* **9**

(85) Chen, R., Lin, Y., Shen, W., Hsieh, T., Yen, K., Chen, S., and Kao, C. (2018). Associations of Tumor PD-1 Ligands, Immunohistochemical Studies, and Textural Features in (18)F-FDG PET in Squamous Cell Carcinoma of the Head and Neck. *Scientific Reports* **8**(1), 105.

(86) Yin, Q., Hung, S., Wang, L., Lin, W., Fielding, J.R., Rathmell, W.K., Khandani, A.H., Woods, M.E., Milowsky, M.I., Brooks, S.A.*, et al.* (2017). Associations between Tumor Vascularity, Vascular Endothelial Growth Factor Expression and PET/MRI Radiomic Signatures in Primary Clear-Cell-Renal-Cell-Carcinoma: Proof-of-Concept Study. *Scientific Reports* **7**43356.

(87) Cook, G., and Goh, V. (2019). What can artificial intelligence teach us about the molecular mechanisms underlying disease? *Eur J Nucl Med Mol Imaging* **46**(13), 2715-2721.

(88) Kido, S., Kuriyama, K., Higashiyama, M., Kasugai, T., and Kuroda, C. (2003). Fractal Analysis of Internal and Peripheral Textures of Small Peripheral Bronchogenic Carcinomas in Thin-section Computed Tomography: Comparison of Bronchioloalveolar Cell Carcinomas With Nonbronchioloalveolar Cell Carcinomas. *J. Comput. Assist. Tomogr.* **27**(1), 56-61.

(89) Chen, W., Giger, M.L., Li, H., Bick, U., and Newstead, G.M. (2007). Volumetric texture analysis of breast lesions on contrast-enhanced magnetic resonance images. *Magnetic Resonance in Medicine* **58**(3), 562-571.

(90) Woods, B.J., Clymer, B.D., Kurc, T., Heverhagen, J.T., Stevens, R., Orsdemir, A., Bulan, O., and Knopp, M.V. (2007). Malignant-lesion segmentation using 4D co-occurrence texture analysis applied to dynamic contrast-enhanced magnetic resonance breast image data. *Journal of Magnetic Resonance Imaging* **25**(3), 495-501.

(91) Holli, K., Lääperi, A., Harrison, L., Luukkaala, T., Toivonen, T., Ryymin, P., Dastidar, P., Soimakallio, S., and Eskola, H. (2010). Characterization of Breast Cancer Types by Texture Analysis of Magnetic Resonance Images. *Acad. Radiol.* **17**(2), 135-141.

(92) Eliat, P., Olivié, D., Saïkali, S., Carsin, B., Saint-Jalmes, H., and de Certaines, J.D. (2012). Can Dynamic Contrast-Enhanced Magnetic Resonance Imaging Combined with Texture Analysis Differentiate Malignant Glioneuronal Tumors from Other Glioblastoma? *Neurology Research International* **2012**1-7.

(93) Mayerhoefer, M.E., Schima, W., Trattnig, S., Pinker, K., Berger-Kulemann, V., and Ba-Ssalamah, A. (2010). Texture-based classification of focal liver lesions on MRI at 3.0 Tesla: A feasibility study in cysts and hemangiomas. *Journal of Magnetic Resonance Imaging* **32**(2), 352-359.

(94) Lopes, R., Ayache, A., Makni, N., Puech, P., Villers, A., Mordon, S., and Betrouni, N. (2010). Prostate cancer characterization on MR images using fractal features. *Med. Phys.* **38**(1), 83-95.

(95) Harrison, L.C.V., Luukkaala, T., Pertovaara, H., Saarinen, T.O., Heinonen, T.T., Järvenpää, R., Soimakallio, S., Kellokumpu-Lehtinen, P., Eskola, H.J., and Dastidar, P. (2009). Non-Hodgkin lymphoma response evaluation with MRI texture classification. *Journal of Experimental & Clinical Cancer Research* **28**(1),

(96) Alic, L., van Vliet, M., van Dijke, C.F., Eggermont, A.M.M., Veenland, J.F., and Niessen, W.J. (2011). Heterogeneity in DCE-MRI parametric maps: a biomarker for treatment response? *Phys. Med. Biol.* **56**(6), 1601-1616.

(97) O'Connor, J.P.B., Rose, C.J., Jackson, A., Watson, Y., Cheung, S., Maders, F., Whitcher, B.J., Roberts, C., Buonaccorsi, G.A., Thompson, G.*, et al.* (2011). DCE-MRI biomarkers of tumour heterogeneity predict CRC liver metastasis shrinkage following bevacizumab and FOLFOX-6. *Br. J. Cancer* **105**(1), 139-145.

(98) Ganeshan, B., Abaleke, S., Young, R.C.D., Chatwin, C.R., and Miles, K.A. (2010). Texture analysis of non-small cell lung cancer on unenhanced computed tomography: initial

evidence for a relationship with tumour glucose metabolism and stage. *Cancer Imaging* **10**(1), 137-143.

(99) Segal, E., Sirlin, C.B., Ooi, C., Adler, A.S., Gollub, J., Chen, X., Chan, B.K., Matcuk, G.R., Barry, C.T., Chang, H.Y., and Kuo, M.D. (2007). Decoding global gene expression programs in liver cancer by noninvasive imaging. *Nat. Biotechnol.* **25**(6), 675-680.

(100) Muers, M.F., Stephens, R.J., Fisher, P., Darlison, L., Higgs, C.M.B., Lowry, E., Nicholson, A.G., O'Brien, M., Peake, M., Rudd, R.*, et al.* (2008). Active symptom control with or without chemotherapy in the treatment of patients with malignant pleural mesothelioma (MS01): a multicentre randomised trial. *Lancet (London, England)* **371**(9625), 1685-1694.

(101) Zucali, P.A., Ceresoli, G.L., De Vincenzo, F., Simonelli, M., Lorenzi, E., Gianoncelli, L., and Santoro, A. (2011). Advances in the biology of malignant pleural mesothelioma. *Cancer Treat. Rev.* **37**(7), 543-558.

(102) Robinson, B.W.S., and Lake, R.A. (2005). Advances in malignant mesothelioma. *N. Engl. J. Med.* **353**(15), 1591-1603.

(103) Cao, C.Q., Yan, T.D., Bannon, P.G., and McCaughan, B.C. (2010). A systematic review of extrapleural pneumonectomy for malignant pleural mesothelioma. *Journal of Thoracic Oncology : Official Publication of the International Association for the Study of Lung Cancer* **5**(10), 1692-1703.

(104) Flores, R.M. (2005). The role of PET in the surgical management of malignant pleural mesothelioma. *Lung Cancer* **49 Suppl 1**S27-S32.

(105) Erasmus, J.J., Truong, M.T., Smythe, W.R., Munden, R.F., Marom, E.M., Rice, D.C., Vaporciyan, A.A., Walsh, G.L., Sabloff, B.S., Broemeling, L.D.*, et al.* (2005). Integrated computed tomography-positron emission tomography in patients with potentially resectable malignant pleural mesothelioma: Staging implications. *J. Thorac. Cardiovasc. Surg.* **129**(6), 1364-1370.

(106) Schneider, D.B., Clary-Macy, C., Challa, S., Sasse, K.C., Merrick, S.H., Hawkins, R., Caputo, G., and Jablons, D. (2000). Positron emission tomography with f18-fluorodeoxyglucose in the staging and preoperative evaluation of malignant pleural mesothelioma. *J. Thorac. Cardiovasc. Surg.* **120**(1), 128-133.

(107) Veit-Haibach, P., Schaefer, N.G., Steinert, H.C., Soyka, J.D., Seifert, B., and Stahel, R.A. (2010). Combined FDG-PET/CT in response evaluation of malignant pleural mesothelioma. *Lung Cancer* **67**(3), 311-317.

(108) Francis, R.J., Byrne, M.J., van der Schaaf, A.,A., Boucek, J.A., Nowak, A.K., Phillips, M., Price, R., Patrikeos, A.P., Musk, A.W., and Millward, M.J. (2007). Early prediction of response to chemotherapy and survival in malignant pleural mesothelioma using a novel semiautomated 3-dimensional volume-based analysis of serial 18F-FDG PET scans. *Journal of Nuclear Medicine : Official Publication, Society of Nuclear Medicine* **48**(9), 1449-1458.

(109) Sharif, S., Zahid, I., Routledge, T., and Scarci, M. (2011). Does positron emission tomography offer prognostic information in malignant pleural mesothelioma? *Interactive Cardiovascular and Thoracic Surgery* **12**(5), 806-811.

(110) Klabatsa, A., Chicklore, S., Barrington, S.F., Goh, V., Lang-Lazdunski, L., and Cook, G.J.R. (2014). The association of 18F-FDG PET/CT parameters with survival in malignant pleural mesothelioma. *European Journal of Nuclear Medicine and Molecular Imaging* **41**(2), 276-282.

(111) Cook, G.J.R., Yip, C., Siddique, M., Goh, V., Chicklore, S., Roy, A., Marsden, P., Ahmad, S., and Landau, D. (2013). Are pretreatment 18F-FDG PET tumor textural features in non-small cell lung cancer associated with response and survival after chemoradiotherapy? *Journal of Nuclear Medicine : Official Publication, Society of Nuclear Medicine* **54**(1), 19-26.

(112) Miwa, K., Inubushi, M., Wagatsuma, K., Nagao, M., Murata, T., Koyama, M., Koizumi, M., and Sasaki, M. (2014). FDG uptake heterogeneity evaluated by fractal analysis improves the differential diagnosis of pulmonary nodules. *Eur. J. Radiol.* **83**(4), 715-719.

(113) Kwek, B.H., Aquino, S.L., and Fischman, A.J. (2004). Fluorodeoxyglucose positron emission tomography and CT after talc pleurodesis. *Chest* **125**(6), 2356-2360.

(114) Uto, F., Shiba, E., Onoue, S., Yoshimura, H., Takada, M., Tsuji, Y., Fukugami, S., Asakawa, I., Tamamoto, T., and Hasegawa, M. (2010). Phantom study on radiotherapy planning using PET/CT--delineation of GTV by evaluating SUV. *J. Radiat. Res.* **51**(2), 157-164.

(115) Chicklore, S., Goh, V., Siddique, M., Roy, A., Marsden, P.K., and Cook, G.J.R. (2013). Quantifying tumour heterogeneity in 18F-FDG PET/CT imaging by texture analysis. *European Journal of Nuclear Medicine and Molecular Imaging* **40**(1), 133-140.

(116) Radulescu, E., Ganeshan, B., Minati, L., Beacher, F D C C., Gray, M.A., Chatwin, C., Young, R.C.D., Harrison, N.A., and Critchley, H.D. (2013). Gray matter textural heterogeneity as a potential in-vivo biomarker of fine structural abnormalities in Asperger syndrome. *The Pharmacogenomics Journal* **13**(1), 70-79.

(117) Orlhac, F., Soussan, M., Maisonobe, J., Garcia, C.A., Vanderlinden, B., and Buvat, I. (2014). Tumor Texture Analysis in 18F-FDG PET: Relationships Between Texture Parameters, Histogram Indices, Standardized Uptake Values, Metabolic Volumes, and Total Lesion Glycolysis. *Journal of Nuclear Medicine : Official Publication, Society of Nuclear Medicine* **55**(3), 414-422.

(118) Brooks, F.J., and Grigsby, P.W. (2014). The Effect of Small Tumor Volumes on Studies of Intratumoral Heterogeneity of Tracer Uptake. *Journal of Nuclear Medicine : Official Publication, Society of Nuclear Medicine* **55**(1), 37-42.

(119) Incerti, E., Broggi, S., Fodor, A., Cuzzocrea, M., Samanes Gajate, A.M., Mapelli, P., Fiorino, C., Dell'Oca, I., Pasetti, M., Cattaneo, M.*, et al.* (2018). FDG PET-derived parameters as prognostic tool in progressive malignant pleural mesothelioma treated patients. *European Journal of Nuclear Medicine and Molecular Imaging* **45**(12), 2071-2078.

(120) Kitajima, K., Doi, H., Kuribayashi, K., Hashimoto, M., Tsuchitani, T., Tanooka, M., Fukushima, K., Nakano, T., Hasegawa, S., and Hirota, S. (2017). Prognostic value of pretreatment volume-based quantitative (18)F-FDG PET/CT parameters in patients with malignant pleural mesothelioma. *Eur. J. Radiol.* **86**176-183.

(121) Nowak, A.K., Francis, R.J., Phillips, M.J., Millward, M.J., van der Schaaf, A.,A., Boucek, J., Musk, A.W., McCoy, M.J., Segal, A., Robins, P., and Byrne, M.J. (2010). A novel prognostic model for malignant mesothelioma incorporating quantitative FDG-PET imaging with clinical parameters. *Clinical Cancer Research : An Official Journal of the American Association for Cancer Research* **16**(8), 2409-2417.

(122) Diaz-Cano, S.J. (2012). Tumor Heterogeneity: Mechanisms and Bases for a Reliable Application of Molecular Marker Design. *International Journal of Molecular Sciences* **13**(2), 1951-2011.

(123) Wu, J., Aguilera, T., Shultz, D., Gudur, M., Rubin, D.L., Loo, B.W., Diehn, M., and Li, R. (2016). Early-Stage Non–Small Cell Lung Cancer: Quantitative Imaging Characteristics of 18F Fluorodeoxyglucose PET/CT Allow Prediction of Distant Metastasis. Radiology *281,* 270-278.

(124) Traverso, A., Wee, L., Dekker, A., and Gillies, R. (2018). Repeatability and Reproducibility of Radiomic Features: A Systematic Review. *International Journal of Radiation Oncology, Biology, Physics* **102**(4), 1143-1158.

(125) Guan, Y., Li, W., Jiang, Z., Chen, Y., Liu, S., He, J., Zhou, Z., and Ge, Y. (2016). Whole-Lesion Apparent Diffusion Coefficient-Based Entropy-Related Parameters for Characterizing Cervical Cancers: Initial Findings. *Acad. Radiol.* **23**(12), 1559-1567.

(126) Forgacs, A., Pall Jonsson, H., Dahlbom, M., Daver, F., D DiFranco, M., Opposits, G., K Krizsan, A., Garai, I., Czernin, J., Varga, J.*, et al.* (2016). A Study on the Basic Criteria for Selecting Heterogeneity Parameters of F18-FDG PET Images. *PloS One* **11**(10), e0164113.

(127) Hyun, S.H., Kim, H.S., Choi, S.H., Choi, D.W., Lee, J.K., Lee, K.H., Park, J.O., Lee, K., Kim, B., and Choi, J.Y. (2016). Intratumoral heterogeneity of 18F-FDG uptake predicts survival in patients with pancreatic ductal adenocarcinoma. *European Journal of Nuclear Medicine and Molecular Imaging* **43**(8), 1461-1468.

(128) Azad, G.K., Cousin, F., Siddique, M., Taylor, B., Goh, V., and Cook, G.J.R. (2019). Does Measurement of First-Order and Heterogeneity Parameters Improve Response Assessment of Bone Metastases in Breast Cancer Compared to SUV(max) in [(18)F]fluoride and [(18)F]FDG PET? *Molecular Imaging and Biology* **21**(4), 781-789.

(129) Hatt, M., Majdoub, M., Vallières, M., Tixier, F., Le Rest, C.C., Groheux, D., Hindié, E., Martineau, A., Pradier, O., Hustinx, R.*, et al.* (2015). 18F-FDG PET uptake characterization through texture analysis: investigating the complementary nature of heterogeneity and functional tumor volume in a multi-cancer site patient cohort. *Journal of Nuclear Medicine : Official Publication, Society of Nuclear Medicine* **56**(1), 38-44.

(130) Jemal, A., Bray, F., Center, M.M., Ferlay, J., Ward, E., and Forman, D. (2011). Global cancer statistics. *CA: A Cancer Journal for Clinicians* **61**(2), 69-90.

(131) Dela Cruz, C.,S., Tanoue, L.T., and Matthay, R.A. (2011). Lung cancer: epidemiology, etiology, and prevention. *Clin. Chest Med.* **32**(4), 605-644.

(132) Di Maio, M., Lama, N., Morabito, A., Smit, E.F., Georgoulias, V., Takeda, K., Quoix, E., Hatzidaki, D., Wachters, F.M., Gebbia, V.*, et al.* (2010). Clinical assessment of patients with advanced non-small-cell lung cancer eligible for second-line chemotherapy: a prognostic score from individual data of nine randomised trials. *European Journal of Cancer (Oxford, England : 1990)* **46**(4), 735-743.

(133) Rinaldi, S., and Berardi, R. (2017). Lung cancer prognosis: can histological patterns and morphological features have a role in the management of lung cancer patients? *Annals of Translational Medicine* **5**(17), 353.

(134) Novello, S., Barlesi, F., Califano, R., Cufer, T., Ekman, S., Levra, M.G., Kerr, K., Popat, S., Reck, M., Senan, S.*, et al.* (2016). Metastatic non-small-cell lung cancer: ESMO Clinical Practice Guidelines for diagnosis, treatment and follow-up. *Annals of Oncology : Official Journal of the European Society for Medical Oncology* **27**v1-v27.

(135) Travis, W.D., Brambilla, E., Nicholson, A.G., Yatabe, Y., Austin, J.H.M., Beasley, M.B., Chirieac, L.R., Dacic, S., Duhig, E., Flieder, D.B.*, et al.* (2015). The 2015 World Health Organization Classification of Lung Tumors: Impact of Genetic, Clinical and Radiologic Advances Since the 2004 Classification. *Journal of Thoracic Oncology : Official Publication of the International Association for the Study of Lung Cancer* **10**(9), 1243-1260.

(136) Amin, M.B., Tamboli, P., Merchant, S.H., Ordóñez, N.,G., Ro, J., Ayala, A.G., and Ro, J.Y. (2002). Micropapillary component in lung adenocarcinoma: a distinctive histologic feature with possible prognostic significance. *Am. J. Surg. Pathol.* **26**(3), 358-364.

(137) Borczuk, A.C. (2016). Prognostic considerations of the new World Health Organization classification of lung adenocarcinoma. *European Respiratory Review : An Official Journal of the European Respiratory Society* **25**(142), 364-371.

(138) Park, H.J., Cha, Y., Kim, S.H., Kim, A., Kim, E.Y., and Chang, Y.S. (2017). Keratinization of Lung Squamous Cell Carcinoma Is Associated with Poor Clinical Outcome. *Tuberculosis and Respiratory Diseases* **80**(2), 179-186.

(139) Le Noci, V., Sommariva, M., Tortoreto, M., Zaffaroni, N., Campiglio, M., Tagliabue, E., Balsari, A., and Sfondrini, L. (2016). Reprogramming the lung microenvironment by inhaled immunotherapy fosters immune destruction of tumor. *Oncoimmunology* **5**(11), e1234571.

(140) Fleming, I.N., Manavaki, R., Blower, P.J., West, C., Williams, K.J., Harris, A.L., Domarkas, J., Lord, S., Baldry, C., and Gilbert, F.J. (2015). Imaging tumour hypoxia with positron emission tomography. *Br. J. Cancer* **112**(2), 238-250.

(141) Yeo, C.D., Kang, N., Choi, S.Y., Kim, B.N., Park, C.K., Kim, J.W., Kim, Y.K., and Kim, S.J. (2017). The role of hypoxia on the acquisition of epithelial-mesenchymal transition and cancer stemness: a possible link to epigenetic regulation. *The Korean Journal of Internal Medicine* **32**(4), 589-599.

(142) Urano, N., Fujiwara, Y., Doki, Y., Tsujie, M., Yamamoto, H., Miyata, H., Takiguchi, S., Yasuda, T., Yano, M., and Monden, M. (2006). Overexpression of hypoxia-inducible factor-1 alpha in gastric adenocarcinoma. *Gastric Cancer : Official Journal of the International Gastric Cancer Association and the Japanese Gastric Cancer Association* **9**(1), 44-49.

(143) Singh, D., Arora, R., Kaur, P., Singh, B., Mannan, R., and Arora, S. (2017). Overexpression of hypoxia-inducible factor and metabolic pathways: possible targets of cancer. *Cell & Bioscience* **7**62.

(144) Nielsen, J.S., and McNagny, K.M. (2008). Novel functions of the CD34 family. *J. Cell. Sci.* **121**(Pt 22), 3683-3692.

(145) Seon, B.K., Haba, A., Matsuno, F., Takahashi, N., Tsujie, M., She, X., Harada, N., Uneda, S., Tsujie, T., Toi, H*., et al.* (2011). Endoglin-targeted cancer therapy. *Curr. Drug Deliv.* **8**(1), 135-143.

(146) Ohno, Y., Koyama, H., Yoshikawa, T., Matsumoto, K., Aoyama, N., Onishi, Y., and Sugimura, K. (2012). Diffusion-weighted MRI versus 18F-FDG PET/CT: performance as predictors of tumor treatment response and patient survival in patients with non-small cell lung cancer receiving chemoradiotherapy. *AJR.American Journal of Roentgenology* **198**(1), 75-82.

(147) Rizk, N.P., Tang, L., Adusumilli, P.S., Bains, M.S., Akhurst, T.J., Ilson, D., Goodman, K., and Rusch, V.W. (2009). Predictive value of initial PET-SUVmax in patients with locally advanced esophageal and gastroesophageal junction adenocarcinoma. *Journal of Thoracic Oncology : Official Publication of the International Association for the Study of Lung Cancer* **4**(7), 875-879.

(148) Vesselle, H., Schmidt, R.A., Pugsley, J.M., Li, M., Kohlmyer, S.G., Vallires, E., and Wood, D.E. (2000). Lung cancer proliferation correlates with [F-18]fluorodeoxyglucose uptake by positron emission tomography. *Clinical Cancer Research : An Official Journal of the American Association for Cancer Research* **6**(10), 3837-3844.

(149) Choi, N.C., Fischman, A.J., Niemierko, A., Ryu, J.S., Lynch, T., Wain, J., Wright, C., Fidias, P., and Mathisen, D. (2002). Dose-response relationship between probability of pathologic tumor control and glucose metabolic rate measured with FDG PET after preoperative chemoradiotherapy in locally advanced non-small-cell lung cancer. *Int. J. Radiat. Oncol. Biol. Phys.* **54**(4), 1024-1035.

(150) Ryu, J.S., Choi, N.C., Fischman, A.J., Lynch, T.J., and Mathisen, D.J. (2002). FDG-PET in staging and restaging non-small cell lung cancer after neoadjuvant chemoradiotherapy: correlation with histopathology. *Lung Cancer* **35**(2), 179-187.

(151) Higashi, K., Ueda, Y., Arisaka, Y., Sakuma, T., Nambu, Y., Oguchi, M., Seki, H., Taki, S., Tonami, H., and Yamamoto, I. (2002). 18F-FDG Uptake as a Biologic Prognostic Factor for Recurrence in Patients with Surgically Resected Non-Small Cell Lung Cancer. *The Journal of Nuclear Medicine* **43**(1), 39.

(152) Ahuja, V., Coleman, R.E., Herndon, J., and Patz Jr., E.F. (1998). The prognostic significance of fluorodeoxyglucose positron emission tomography imaging for patients with nonsmall cell lung carcinoma. *Cancer* **83**(5), 918-924.

(153) Vansteenkiste, J.F., Stroobants, S.G., Dupont, P.J., De Leyn, P.R., Verbeken, E.K., Deneffe, G.J., Mortelmans, L.A., and Demedts, M.G. (1999). Prognostic Importance of the Standardized Uptake Value on 18F-Fluoro-2-Deoxy-Glucose–Positron Emission Tomography Scan in Non–Small-Cell Lung Cancer: An Analysis of 125 Cases. *Jco* **17**(10), 3201-3206.

(154) Sugawara, Y., Quint, L.E., Iannettoni, M.D., Orringer, M.B., Russo, J.E., Recker, B.E., Saran, P.A., and Wahl, R.L. (1999). Does the FDG Uptake of Primary Non-Small Cell Lung Cancer Predict Prognosis?. A Work in Progress. *Clin. Positron Imaging* **2**(2), 111-118.

(155) Dhital, K., Saunders, C.A., Seed, P.T., O'Doherty, M.J., and Dussek, J. (2000). (18)F]Fluorodeoxyglucose positron emission tomography and its prognostic value in lung cancer. *Eur. J. Cardiothorac. Surg.* **18**(4), 425-428.

(156) Hanahan, D., and Weinberg, R.A. (2011). Hallmarks of cancer: the next generation. *Cell* **144**(5), 646-674.

(157) Junttila, M.R., and de Sauvage, F.J. (2013). Influence of tumour micro-environment heterogeneity on therapeutic response. *Nature* **501**(7467), 346-354.

(158) Zwanenburg, A., Vallières, M., Abdalah, M.A., Aerts, H. J. W. L., Andrearczyk, V., Apte, A., Ashrafinia, S., Bakas, S., Beukinga, R.J., Boellaard, R.*, et al.* (2020). The Image Biomarker Standardization Initiative: Standardized Quantitative Radiomics for High-Throughput Image-based Phenotyping. *Radiology* 191145.

(159) Hatt, M., Tixier, F., Cheze Le Rest, C., Pradier, O., and Visvikis, D. (2013). Robustness of intratumour ^{18}F-FDG PET uptake heterogeneity quantification for therapy response prediction in oesophageal carcinoma. *Eur. J. Nucl. Med. Mol. Imaging* **40**(11), 1662-1671.

(160) Kinahan, P.E., and Fletcher, J.W. (2010). Positron emission tomography-computed tomography standardized uptake values in clinical practice and assessing response to therapy. *Semin. Ultrasound CT MR* **31**(6), 496-505.

(161) Grove, O., Berglund, A.E., Schabath, M.B., Aerts, H.J., Dekker, A., Wang, H., Velazquez, E.R., Lambin, P., Gu, Y., Balagurunathan, Y.*, et al.* (2015). Quantitative computed tomographic descriptors associate tumor shape complexity and intratumor heterogeneity with prognosis in lung adenocarcinoma. *PLoS One* **10**(3), e0118261.

(162) Weiss, G.J., Ganeshan, B., Miles, K.A., Campbell, D.H., Cheung, P.Y., Frank, S., and Korn, R.L. (2014). Noninvasive image texture analysis differentiates K-ras mutation from pan-wildtype NSCLC and is prognostic. *PLoS One* **9**(7), e100244.

(163) Hayano, K., Kulkarni, N.M., Duda, D.G., Heist, R.S., and Sahani, D.V. (2016). Exploration of Imaging Biomarkers for Predicting Survival of Patients With Advanced Non-Small Cell Lung Cancer Treated With Antiangiogenic Chemotherapy. *AJR Am. J. Roentgenol.* **206**(5), 987-993.

(164) Hatt, M., Dekker, A., Ruysscher, D.D., Oellers, M., Lambin, P., Roux, C., Visvikis, D. (2008). Accurate functional volume definition in PET for radiotherapy treatment planning. *IEEE Nuclear Science Symposium Conference Record.* 5567-71.

(165) Hatt, M., Cheze le Rest, C., Turzo, A., Roux, C., and Visvikis, D. (2009). A fuzzy locally adaptive Bayesian segmentation approach for volume determination in PET. *IEEE Trans. Med. Imaging* **28**(6), 881-893.

(166) Wei, D., Chen, W., Meng, R., Zhao, N., Zhang, X., Liao, D., and Chen, G. (2018). Augmented expression of Ki-67 is correlated with clinicopathological characteristics and prognosis for lung cancer patients: an up-dated systematic review and meta-analysis with 108 studies and 14,732 patients. *Respiratory Research* **19**(1), 150.

(167) Mineo, T.C., Ambrogi, V., Baldi, A., Rabitti, C., Bollero, P., Vincenzi, B., and Tonini, G. (2004). Prognostic impact of VEGF, CD31, CD34, and CD105 expression and tumour vessel invasion after radical surgery for IB-IIA non-small cell lung cancer. *J. Clin. Pathol.* **57**(6), 591-597.

(168) Yohena, T., Yoshino, I., Takenaka, T., Kameyama, T., Ohba, T., Kuniyoshi, Y., and Maehara, Y. (2009). Upregulation of hypoxia-inducible factor-1alpha mRNA and its clinical significance in non-small cell lung cancer. *J. Thorac. Oncol.* **4**(3), 284-290.

(169) Mamede, M., Higashi, T., Kitaichi, M., Ishizu, K., Ishimori, T., Nakamoto, Y., Yanagihara, K., Li, M., Tanaka, F., Wada, H.*, et al.* (2005). 18F]FDG uptake and PCNA, Glut-1, and Hexokinase-II expressions in cancers and inflammatory lesions of the lung. *Neoplasia* **7**(4), 369-379.

(170) Vesselle, H., Salskov, A., Turcotte, E., Wiens, L., Schmidt, R., Jordan, C.D., Vallières, E., and Wood, D.E. (2008). Relationship between non-small cell lung cancer FDG uptake at PET, tumor histology, and Ki-67 proliferation index. *J. Thorac. Oncol.* **3**(9), 971-978.

(171) Ancevski Hunter, K., Socinski, M.A., and Villaruz, L.C. (2018). PD-L1 Testing in Guiding Patient Selection for PD-1/PD-L1 Inhibitor Therapy in Lung Cancer. *Molecular Diagnosis & Therapy* **22**(1), 1-10.

(172) Lynch, T.J., Bell, D.W., Sordella, R., Gurubhagavatula, S., Okimoto, R.A., Brannigan, B.W., Harris, P.L., Haserlat, S.M., Supko, J.G., Haluska, F.G.*, et al.* (2004). Activating mutations in the epidermal growth factor receptor underlying responsiveness of non-small-cell lung cancer to gefitinib. *N. Engl. J. Med.* **350**(21), 2129-2139.

(173) Paez, J.G., Jänne, P.A., Lee, J.C., Tracy, S., Greulich, H., Gabriel, S., Herman, P., Kaye, F.J., Lindeman, N., Boggon, T.J.*, et al.* (2004). EGFR mutations in lung cancer: correlation with clinical response to gefitinib therapy. *Science* **304**(5676), 1497-1500.

(174) Sasaki, H., Shimizu, S., Endo, K., Takada, M., Kawahara, M., Tanaka, H., Matsumura, A., Iuchi, K., Haneda, H., Suzuki, E.*, et al.* (2006). EGFR and erbB2 mutation status in Japanese lung cancer patients. *Int. J. Cancer* **118**(1), 180-184.

(175) Olaussen, K.A., Dunant, A., Fouret, P., Brambilla, E., André, F., Haddad, V., Taranchon, E., Filipits, M., Pirker, R., Popper, H.H.*, et al.* (2006). DNA repair by ERCC1 in non-small-cell lung cancer and cisplatin-based adjuvant chemotherapy. *N. Engl. J. Med.* **355**(10), 983-991.

(176) Sasaki, T., Rodig, S.J., Chirieac, L.R., and JÃ¤nne, P.A. (2010). The biology and treatment of EML4-ALK non-small cell lung cancer. *Eur. J. Cancer* **46**(10), 1773-1780.

(177) Wong, D.W., Leung, E.L., So, K.K., Tam, I.Y., Sihoe, A.D., Cheng, L.C., Ho, K.K., Au, J.S., Chung, L.P., Pik Wong, M., and University of Hong Kong Lung Cancer Study Group. (2009). The EML4-ALK fusion gene is involved in various histologic types of lung cancers from nonsmokers with wild-type EGFR and KRAS. *Cancer* **115**(8), 1723-1733.

(178) Mok, T.S., Wu, Y.L., Thongprasert, S., Yang, C.H., Chu, D.T., Saijo, N., Sunpaweravong, P., Han, B., Margono, B., Ichinose, Y.*, et al.* (2009). Gefitinib or carboplatin-paclitaxel in pulmonary adenocarcinoma. *N. Engl. J. Med.* **361**(10), 947-957.

(179) Maemondo, M., Inoue, A., Kobayashi, K., Sugawara, S., Oizumi, S., Isobe, H., Gemma, A., Harada, M., Yoshizawa, H., Kinoshita, I.*, et al.* (2010). Gefitinib or chemotherapy for non-small-cell lung cancer with mutated EGFR. *N. Engl. J. Med.* **362**(25), 2380-2388.

(180) Castello, A., Grizzi, F., Toschi, L., Rossi, S., Rahal, D., Marchesi, F., Russo, C., Finocchiaro, G., and Lopci, E. (2018). Tumor heterogeneity, hypoxia, and immune markers in surgically resected non-small-cell lung cancer. *Nucl. Med. Commun.* **39**(7), 636-644.

(181) van Baardwijk, A., Bosmans, G., van Suylen, R.J., van Kroonenburgh, M., Hochstenbag, M., Geskes, G., Lambin, P., and De Ruysscher, D. (2008). Correlation of intra-tumour heterogeneity on 18F-FDG PET with pathologic features in non-small cell lung cancer: a feasibility study. *Radiother. Oncol.* **87**(1), 55-58.

(182) Nelson, D.A., Tan, T.T., Rabson, A.B., Anderson, D., Degenhardt, K., and White, E. (2004). Hypoxia and defective apoptosis drive genomic instability and tumorigenesis. *Genes Dev.* **18**(17), 2095-2107.

(183) Semenza, G.L. (2002). HIF-1 and tumor progression: pathophysiology and therapeutics. *Trends Mol. Med.* **8**(4 Suppl), 62.

(184) Ha, S., Choi, H., Cheon, G.J., Kang, K.W., Chung, J., Kim, E.E., and Lee, D.S. (2014). Autoclustering of Non-small Cell Lung Carcinoma Subtypes on (18)F-FDG PET Using Texture Analysis: A Preliminary Result. *Nuclear Medicine and Molecular Imaging* **48**(4), 278-286.

(185) Karetsi, E., Ioannou, M.G., Kerenidi, T., Minas, M., Molyvdas, P.A., Gourgoulianis, K.I., and Paraskeva, E. (2012). Differential expression of hypoxia-inducible factor 1Î± in non-small cell lung cancer and small cell lung cancer. *Clinics (Sao Paulo, Brazil)* **67**(12), 1373-1378.

(186) Haralick, R.M., Shanmugam, K., and Dinstein, I. (1973). Textural Features for Image Classification. *IEEE Transactions on Systems, Man, and Cybernetics* **SMC-3**(6), 610-621.

(187) Galloway, M.M. (1975). Texture analysis using gray level run lengths. *Computer Graphics and Image Processing* **4**(2), 172-179.

(188) Pentland, A.P. (1984). Fractal-Based Description of Natural Scenes. *IEEE Transactions on Pattern Analysis and Machine Intelligence* **PAMI-6**(6), 661-674.

(189) Thibault, G., Fertil, B., Navarro, C., Pereira, S., Cau, P., Lévy, N., Sequeira, J., and Mari, J. (2013). Shape and texture indexes - Application to cell nuclei classification. *Int. J. Pat. Recognit. Artif. Intell.* **27**1357002.

(190) Zwanenburg, A., Leger, S., Vallières, M., and Löck, S. (2016). Image biomarker standardisation initiative.

APPENDIX 1

Textural parameters derived from ^{18}F-FDG PET images using FAST(186-190)

Measures of Central Tendency

Mean

The mean of a data set is the average of all the data values. The sample mean is the point estimator of the population mean μ. Let N be the number of voxels in 3D ROI and $I(i)$ be the grey level at a particular voxel i.

$$\mu = \frac{1}{N}\sum_{i=1}^{N} I(i)$$

Median

The median of a data set is the value in the middle when the data items are arranged in ascending order. Whenever a data set has extreme values, the median is the preferred measure of central location.

Mode

The mode of a data set is the value that occurs with the greatest frequency.

Percentiles

A percentile provides information about how the data are spread over the interval from the smallest value to the largest value. The pth percentile of a data set is a value such that at least p percent of the items take on this value or less and at least (100 - p) percent of the items take on more than this value.

Measures of Variability

Range

The range of a data set is the difference between the largest and smallest data values. It is very sensitive to the smallest and largest data values.

Variance

The variance is a measure of variability that utilises all the data. The variance is the average of the squared differences between each data value and the mean.

$$\sigma^2 = \frac{1}{N-1}\sum_{i=1}^{N}[I(i)-\mu]^2$$

Standard Deviation

The SD of a data set is the positive square root of the variance. It is measured in the same units as the data, making it more easily interpreted than the variance.

$$\sigma = \sqrt{\frac{1}{N-1}\sum_{i=1}^{N}[I(i)-\mu]^2}$$

Skewness

It is an indicator used in distribution analysis as a sign of asymmetry and deviation from a normal distribution. If skewness is negative, the data are spread out more to the left of the mean than to the right. If skewness ‘s ‘ is positive, the data are spread out more to the right. The skewness of the normal distribution (or any perfectly symmetric distribution) is zero.

$$s = \frac{1}{N}\sum_{i=1}^{N}\left[\frac{I(i)-\mu}{\sigma}\right]^3$$

- Skewness > 0: Right skewed distribution - most values are concentrated on left of the mean, with extreme values to the right.
- Skewness < 0: Left skewed distribution - most values are concentrated on the right of the mean, with extreme values to the left.
- Skewness = 0: mean = median, the distribution is symmetrical around the mean.

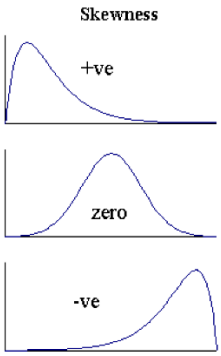

Kurtosis

This indicator is used in distribution analysis as a sign of flattening or "peakedness" of a distribution. Kurtosis ‘k ‘ is a sign of flattening or "peakedness" of a distribution and is a measure of how outlier-prone a distribution is. The kurtosis of the normal distribution is 3. Distributions that are more outlier-prone than the normal distribution have kurtosis greater than 3; distributions that are less outlier-prone have kurtosis less than 3.

$$\mathrm{k} = \frac{1}{N}\sum_{i=1}^{N}\left[\frac{I(i)-\mu}{\sigma}\right]^4$$

- Kurtosis > 3 - Leptokurtic distribution, sharper than a normal distribution, with values concentrated around the mean and thicker tails. This means high probability for extreme values.

- Kurtosis < 3 - Platykurtic distribution, flatter than a normal distribution with a wider peak. The probability for extreme values is less than for a normal distribution, and the values are wider spread around the mean.
- Kurtosis = 3 - Mesokurtic distribution - normal distribution for example.

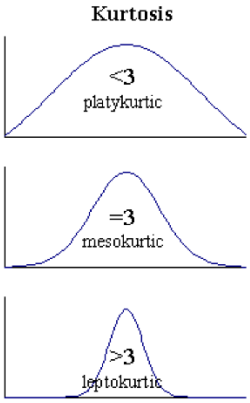

First-Order Measures of Texture

Entropy

Entropy is a statistical measure of randomness that can characterise the heterogeneity of the tumour. It results in high value if tumour have more diverse uptake consisting of many distinct SUVs and uniform frequency of these SUVs. Although tumour with high SUV_{max} tends to have more distinct SUVs than a tumour with low SUV_{max} and it may correlate quite well with entropy, it may not always be the case and a tumour with low SUV_{max} may be more diverse in terms of intensity distribution. A predominantly random distribution has higher entropy. Highly correlated or uniform distribution have low entropy. Therefore, it should not be taken as an independent predictor of heterogeneity.

Let p(i,j) is a vector that contains the histogram counts. Entropy is defined as:

$$\text{entropy} = -\sum_{i=1}^{N_g} p(i)\log_2 p\,(i)$$

Where Ng is total number of different grey levels present in the image. For an image which has been perfectly histogram equalized, the entropy of the image will be maximum. On the other hand, if the image has been thresholded, so that only two states are occupied, the entropy will be low. If all of the pixels have the same value, the entropy of the image is zero.

Energy

Energy takes higher value if histogram is narrowed dominated by single vale. Broader intensity distribution causes the energy to decrease. Energy provides the sum of squared elements in the ROI. It is also known as uniformity or the angular second moment.

$$\text{energy} = \sum_{i=1}^{N_g} [p(i)]^2$$

<u>Neighbourhood Grey Tone Difference Matrices</u>

Coarseness

Large values represent areas where grey-tone differences are small, i.e., coarse texture. In a coarse texture, the primitives or basic patterns making up the texture are large. As a result, such a texture tends to possess a high degree of local uniformity in intensity, even over a fairly large area.

$$f_{cos} = \left[\varepsilon + \sum_{i=1}^{G_h} p_i\, s(i)\right]^{-1}$$

Contrast

This quantity increases with the amount of local variation in intensity. An image is said to have a high level of contrast if areas of different intensity levels are clearly visible. Thus, a high contrast means that the intensity difference between neighbouring regions is large. This is usually the case when the dynamic range of grey scale is large or when it is stretched.

$$f_{con} = \left[\frac{1}{N_g(N_g-1)}\sum_{i=1}^{G_h}\sum_{j=1}^{G_h} p_i\, p_j (i-j)^2\right]\left[\frac{1}{n^2}\sum_{i=1}^{G_h} s(i)\right]$$

Busyness

A busy texture is one in which there are rapid changes of intensity from one pixel to its neighbour; that is the spatial frequency of intensity changes is very high. A higher value of busyness would tend to emphasize the frequency of spatial changes in intensity values.

$$f_{bus} = \sum_{i=1}^{G_h} p_i\, s(i) \Big/ \sum_{i=1}^{G_h}\sum_{j=1}^{G_h} [\, ip_i - jp_j]$$

Complexity

A texture is considered complex if the information content is high. This occurs when there are many patches or primitives present in the texture, and more so when the primitives have different average intensities. High values of complexity would indicate a high degree of information content.

$$f_{com} = \sum_{i=1}^{G_h}\sum_{j=1}^{G_h} \left\{|i-j|/\left(n^2(p_i+p_j)\right)\right\}\{\, p_i\, s(i) + p_j s(j)\}$$